STUDY OF NANOWIRES FOR MICROWAVE AND MILLIMETER WAVE FREQUENCY APPLICATIONS

A DISSERTATION

SUBMITTED TO THE FACULTY OF

THE UNIVERSITY OF MINNESOTA

BY

Yali Zhang

IN PARTIAL FULFILLMENT OF THE REQUIREMENTS

FOR THE DEGREE OF

DOCTOR OF PHILOSOPHY

Rhonda Franklin, Advisor

December 2021

Acknowledgements

During my PhD study in the past five years at the University of Minnesota, there are many great people that have supported and enlightened me. Among them, I would like to thank Prof. Rhonda Franklin first. She is a very patient and insightful advisor who provides invaluable suggestion and guidance to help me develop important skills to solve my research problems. She also teaches me how to communicate, present, and write in an academic environment, which I believe will benefit me in my future career. Thanks to her excellent mentoring, I learned to become a better student, a better researcher, and a better collaborator.

I would like to thank Prof. Bethanie Stadler for her mentoring and help. Working with her and her research group is an enjoyable and fruitful experience for me. I also greatly appreciate the guidance from Prof. Rashaunda Henderson. She and her group from University of Texas-Dallas supported my research on high frequency responses. I want to thank for the technical support from Prof. Yahya Tousi. And I would like to thank Prof. Michael Garwood, for his time to provide comments and suggestions on this dissertation.

The equipment used for 67 GHz measurement is from Prof. Tousi's lab. The 110 GHz measurement results are provided by Prof. Henderon's lab. I want to thank National Science Foundation, Semiconductor Research Corporation, and ARFTG Roger Pollard fellowship for the funding support. Part of research in this thesis is performed in the Minnesota Nano Center.

I appreciate the help and support from my MPACT group member, Chanjoon Lee, Wen Zhou, Aditya Dave, and Lucia Garcia. I would like to also offer my thank for the contribution from the members of Prof. Stadler's group, Zohreh Nemati, Joseph Um, and Allison Harpel and Nikita Mahjabeen from Prof. Henderson's group.

Lastly, I would like to thank the support and love from my parents, Jiande Zhang and Songqi Yang.

Dedication

This thesis is dedicated to:

My beloved parents, Songqi Yang and Jiande Zhang

Abstract

This dissertation discusses the application of nanowire (NW) technology applied in millimeter wave and sub-millimeter wave frequency bands. Both magnetic nanowires (MNWs) and copper (Cu) NWs are studied. MNW is proposed for use as bio-labels in nanomedicine application and as magnetic substrate in non-reciprocal design for communication application. To do that, the ferromagnetic resonance (FMR) technique is adopted for MNWs characterization. Cu NW is investigated for use as vertical interconnect in integrated circuit (IC) for wireless communication applications. A coplanar waveguide (CPW) with NW Cu vias design was proposed and studied.

The theory and simulation model of MNWs and Cu NWs are first discussed to provide preliminary understanding of the FMR of MNWs and concepts of Cu NW-based vias (chapter 2). Then the MNWs are fully characterized in the DC field domain. The FMR characterization system and methods are developed. The factors that influence the FMR characterization are studied. A tri-labeling system is built based on nickel (Ni), cobalt (Co) and iron (Fe) MNWs. The MNWs in a bio-mimicking and biological media are characterized (chapter 3). Next, to use MNWs in non-reciprocal devices, three key parameters are defined, FMR frequencies, permeability, and linewidth. A complete characterization method is developed to acquire these three parameters accurately (chapter 4). Lastly, the Cu NWs vias in a CPW structure are designed, fabricated, and measured in three frequency bands 0.04-40 GHz, 0.01- 67 GHz and 0.01-110 GHz. The NW via loss is

extracted and compared to other advanced via technologies. A comparison of NW and conventional via is also presented. (chapter 5).

The outcome of different study investigated in this work show the promising potential of NWs as a favorable material for future biomedical and communication applications.

Table of Contents

List of Abbreviation

3D	three dimensional
AAO	anodized aluminum oxide
Al	aluminum
Bcc	body-centered cubic
Co	cobalt
CPW	coplanar waveguide
Cu	copper
Fcc	face-centered cubic
Fe	iron
FMR	ferromagnetic resonance
iAAO	integrated anodized aluminum oxide
IC	integrated circuit
IOT	internet of things
IP	in plane
LRRM	Line-reflect-reflect-match
MNW	magnetic nanowire
MRI	magnetic resonance imaging

Ni	nickel
NW	nanowire
OP	out of plane
PAM	phase analysis method
PEG	polyethylene glycol
SEM	scanning electron microscopy
Si	silicon
SIW	substrate integrated waveguide
SNR	signal to noise ratio
VL	via length
VNA	vector network analyzer
VW	via width

List of Tables

List of Figures

Chapter 1 Introduction

1.1 Background and motivation

Future millimeter wave and sub-millimeter wave communication systems are essential for internet of things (IOT) devices, autonomous vehicles, and low-power Cube-satellites. The requirements for further miniaturization and performance enhancement, however, are still very challenging to meet. Nanostructure-based low loss three dimensional integrated circuits (3DIC) can be a game changer in these areas due to their small size, low loss and high integration. In addition, there is a need in the field of emerging nanomedicine to provide precise detection of pathological changes and targeted therapy, which can be addressed by using the AC properties of magnetic nanostructures to create bio-labels. Both areas demand effective design and measurement technique for nanoscale components in micrometer-scale devices. This work focuses on developing accurate and sensitive methods to characterize nanowires (NWs) for cell labeling in nanomedicine and component circuitry in 5G communication.

1.2 Use of NWs for biolabeling application

Bio-labels are usually defined as micro- or nano-scale components that can be integrated into a biological environment [1]. For example, typical biosensor technology for cancer tracking uses optical or electrochemical methods based on particles such as fluorescence molecules [2]-[3] or quantum dots [4]-[5]. This technology shows success for detecting cancer cells with high sensitivity using a small amount of analyte such as serum or blood. However, these particles have poor mobility within the fluid environment, and they are limited to single biomarker detection.

To address these limitations, magnetic nanoparticles, and magnetic nanowires (MNWs), which can be easily moved by external magnet, are considered promising for next generation bio-labels. They have been extensively studied for biological applications ranging from drug delivery [6], hyperthermia treatment [7] and contrast agent for magnetic resonance imaging (MRI) [8]. Recently, they have also been reported to show potential to be used for multiple bio-labels detection [9].

Compared to nanoparticles, which typically have a wide size distribution due to fabrication limitations [10], MNWs, grown in substrates with nanometer diameter pores, have several new advantages that make them better biological application candidates especially bio-labels. First, the well-defined pores in the substrate template make the size of MNWs more controllable. Second, MNWs possess large surface area for coating and bio-functionalization due to their suppressed tendency of aggregation. An Au coating on cobalt (Co) and nickel (Ni) NWs has shown the benefit of mitigating the oxidization of these metallic nano labels [11], whereas a polyethylene glycol (PEG) coating on NWs reduces the metal toxicity [12]. Third, the high aspect ratio, easily achievable by MNW, is defined as the length to diameter ratio and offers good ferromagnetic resonance (FMR) properties that could be very useful for tracking NWs.

FMR measurement is an important technique that has been prevalently used for characterizing the dynamic response of magnetic material. FMR is defined as the natural precession of magnetization in magnetic material when the material is exposed to a specific combination of DC and AC magnetic fields.

The high aspect ratio MNWs in low DC field possess FMR absorption at microwave frequencies that can be easily tuned. These features make MNWs great candidates for nano-labels to tag cells.

In this work, MNWs will be studied for use as bio-labels using the FMR measurement technique to achieve detection and identification. A scanning electron microscope (SEM) image of MNWs inside cells is shown in Fig 1.1.

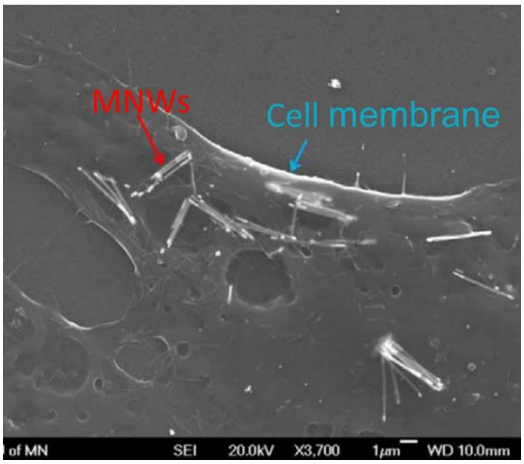

Fig 1.1. MNWs internalized in a cell [13]

1.3 Use of NWs for communication application

For communication operating in the microwave and submillimeter wave frequency range, nanostructures with magnetic and non-magnetic properties are prime candidates for circuit and sensor technology to provide low loss and high circuit performance.

1.3.1 Communication device application

Conventional non-reciprocal device designs use magnetic substrate to provide signal transmission and isolation in the same signal path. Typical magnetic substrate is magnetic thin films, which have been widely studied for communication device design. Ferrites with

garnet or spinel structure needs an external permanent magnet to provide external magnetic field which greatly increases the device sizes [14]-[15]. One solution is to use M-type ferrite, which possess high crystalline anisotropy, to create self-biased non-reciprocal device [16]-[17]. It eliminates a need for an external magnet. Unfortunately, the insertion loss doesn't show good results, which might be due to rough surface and defects created in the fabrication process.

Alternatively, MNW is explored to be used as magnetic substrate that can achieve non-reciprocity and has extremely smooth surface due to the substrate's properties. Its long thin shape provides a large remnant state, which allows high magnetization to exist when external DC field is zero. Therefore, MNW substrates can eliminate the need for undesirable external magnets and reduce the device size. Using MNW substrate, the operating frequency can be easily tuned in the synthesis process. Also, MNWs grown in an anodized aluminum oxide (AAO) template provide high stability, compared to thin film, due to less exposure to the air. Examples of microwave devices fabricated with MNWs in AAO template for use in wireless communications are circulator [18] and phase shifter [19]. Recently, a circulator design fabricated on 100 μm thick MNWs in AAO showed promising results with -2.7 dB insertion loss, around -15 dB return loss and 12.4 dB non-reciprocity at 5.9 GHz [20].

To use MNWs as magnetic substrate, the characterization process is needed. In this dissertation, the key design parameters for MNW substrate, such as FMR frequencies and permeability, will be extracted and discussed.

1.3.2 Interconnect for 3DIC application

Three dimensional integrated circuits (3DIC) play an important role in future communication technology and chip technology. They require low surface area, low cost, and high signal-speed. To reduce the circuit size and cost, one solution is to create circuits based on small, cheap, and good quality via technology.

A via is defined as a vertical interconnect transition between circuits on different layers of chips. As silicon (Si) technology expands to higher frequency, the vias fabricated on high resistivity Si wafer [21]-[22] becomes popular for its low parasitic inductance and low dielectric loss. The vias in these works are thicker than 100 μm. For thinner substrate, such as 50 μm thick commercial AAO, copper (Cu) NWs are used as vertical vias. They show low loss in millimeter and submillimeter frequency bands. Cu NW vias fabricated in commercial AAO template have shown loss of 0.035 dB at 40 GHz [23] and 0.23 dB at 110 GHz [24]. They are also used in passive circuit components such as substrate integrated waveguide [25] and inductors. A 2 turns inductor fabricated on the commercial AAO with Cu NW as interconnection has the Q of 16 at 4 GHz and the inductance of 0.5 nH [26]. These results demonstrate that the benefits of using AAO as a substrate.

In this work, a novel integrated Cu NWs via technology, which is fabricated in the integrated AAO (iAAO) on Si wafer, is proposed. Due to nanometer-size, Cu NWs provide a high penetration to electromagnetic fields at high frequency which provide reduced conductor loss. When used in bundles, they can guarantee the uniformity and low parasitic inductance. The proposed structure gains the benefit of low loss Cu NWs and achieves a high integration by using iAAO on Si wafer.

1.4 Thesis overview

Chapter 2 will discuss the theory and simulation model developed for magnetic and non-magnetic nanowires (NWs) study. For MNWs, the Kittel equation is used to predict the FMR frequencies. Two software, Object Oriented Micromagnetic Framework (OOMMF) [27] and NMAG Computational Micro magnetism (NMAG) [28], are used to obtain susceptibility, FMR frequencies, and linewidth for single and arrays of MNW. For circuit-level simulation, the Cu NW will be used as vias in a coplanar waveguide (CPW) line. The basic design and simulation method in a full wave electromagnetic modeling tool, HFSS, is discussed.

In chapter 3, the FMR of MNWs grown in AAO template is discussed. They are characterized in DC field domain. The theory from chapter 2 will provide theoretical predications of FMR frequencies and will be compared to the experimental results. The factors that influence FMR characterization are studied, and the results will be used later when the FMR signal needs to be evaluated in an application. Three types of MNW materials, Ni, Fe and Co, are considered for use in building a tri-labeling system. Finally, the FMR response of MNWs in polycarbonate, which provide bio-mimicking environment, and in biological samples is evaluated.

In chapter 4, the FMR of MNWs are characterized in frequency domain to be used as magnetic substrate for microwave devices. Three key parameters are important to determine: FMR frequency, permeability, and linewidth. The extraction method from measurement data will be developed and discussed.

Chapter 5 investigates the use of Cu NWs as vertical integrated vias. The NW vias are fabricated and measured in three frequency bands, up to 40 GHz, up to 67 GHz and up to 110 GHz. The via loss is extracted and compared to other advanced technology in literature. A comparison of NW and conventional vias is also presented.

Lastly, chapter 6 will provide a summary of this dissertation and propose ideas for future work.

Chapter 2 Theory for magnetic and Cu NWs

2.1 Introduction

Magnetic nanowires (MNWs) show great potential to be used as labels in biological applications due to their small size, which allows them to be taken into or attached to a cell, and their magnetic properties, which allow them to be detected and identified. Also, their high shape anisotropy along the wire axis provides FMR frequencies in microwave frequency band with zero external DC field, which provides advantages for use in non-reciprocal device. Non-magnetic nanowires (NWs) on the other hand can be used in device to reduce the loss. As a result, theoretical study of single and array MNWs [9], [29] and NWs in general [23]-[24] has stimulated active research, recently.

For biolabeling applications and non-reciprocal device design, the ferromagnetic resonance (FMR) of MNWs need to be studied. The Kittel equation predicts the FMR frequencies of single and arrays of MNWs, where for arrays, values of porosity, magnetization, and external magnetic field are needed. However, lacking in the Kittel equation are the effects on diameter and length. The linewidth, which influences the detection resolution, is also missing. Therefore, micromagnetic simulation tools like OOMMF and NMAG are used to study these properties and the dynamic response of single and arrays of MNWs, based on wire physical parameters.

For communication applications, non-magnetic NWs such as copper (Cu) NWs can be used as a vertical interconnect. The large size differences between NWs in nanometers and transmission line geometry in microns, make it difficult to use a 3D electromagnetic simulation tools accurately and require long computation time. In [24], a lumped element

model of Cu NW interconnect was presented to model the NW vias while maintaining acceptable computation time. However, experimental data is needed to extract the value of each of lumped element. Herein, a micron-sized Cu pillar model that account for porosity will be shown to approximate RF performance of Cu NW arrays that can be used as interconnect with acceptable computation time.

In this chapter, the theory and simulation study of NWs will be discussed. First, MNWs study will be described in chapter 2.2. Next, a model will be presented in chapter 2.3 for Cu NWs that forms vertical vias.

2.2 Theory and simulation of MNWs

2.2.1 Theory of MNW study using Kittel equation

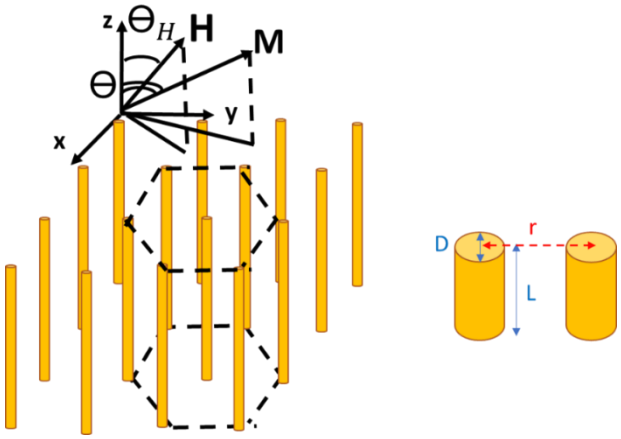

Fig 2.1. Coordinate system for an array of MNWs. MNWs in the array are arranged in hexagonal. θ is the angle between magnetization, M, and z axis. θ_H is the angle between external DC field, H, and z axis. The MNW diameter, length and interwire distance can be represented by D, L and r, respectively.

The Kittle equation [30], equation 2.1, describes the dependence of FMR frequency on effective anisotropy field inside the material and applied external field

$$\omega_{FMR} = \gamma * \sqrt{\left[Hcos(\theta - \theta_H) + H_{eff}cos^2\theta\right][Hcos(\theta - \theta_H) + H_{eff}cos2\theta]} \qquad (2.1)$$

where ω_{FMR} represents FMR frequencies, H is external DC magnetic field, H_{eff} is effective field inside MNWs, θ_H is the angle of external magnetic field, θ is the angle of magnetization (M) and γ is gyromagnetic ratio for specific material. For Co, Ni and Fe, γ has value of 3.003 MHz/Oe, 2.912 MHz/Oe and 3.318 MHz/Oe, respectively. The angles θ and θ_H are shown in Fig 2.1.

Three internal fields of magnetic material are included in H_{eff}: (1) dipolar interaction field (H_{dip}), (2) crystalline anisotropy field (H_u) and (3) demagnetization anisotropy field (H_{dem}). H_{dip} reflects how each single MNW in the array interacts with each other. H_u indicates how the crystalline structure of MNWs influence the FMR response. Lastly, H_{dem} indicates the FMR dependence on the shape of single and array of MNWs, which can be changed by porosity and aspect ratio between MNW diameter and length.

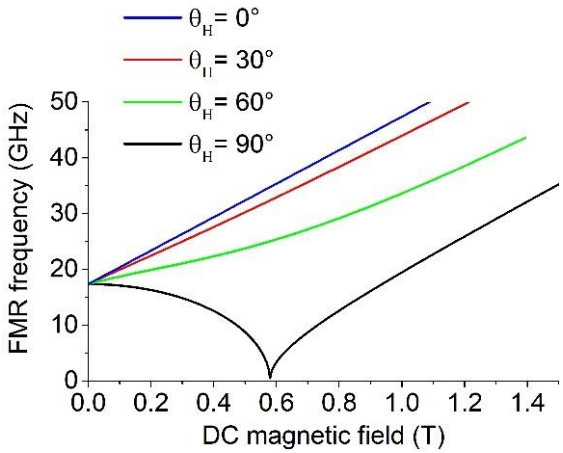

Fig 2.2. FMR responses for θ_H = 0 °, 30 °, 60 ° and 90 ° calculated using Kittel equation.

To predict the experimental FMR response of MNWs with different orientations, an example of Co MNWs with length of 15.5 μm, porosity of 12% and diameter of 40nm

is used for the Kittel equation calculation. In Fig 2.2, the FMR responses of Co MNWs at four different θ_H is predicted.

Due to MNWs' long thin shape, the high shape anisotropy field is along with wire axis and therefore the magnetization aligns with the wire axis at the initial state. This property creates two special cases for FMR response study in MNWs, θ_H = 0 ° and 90 °; one has external DC field align with internal magnetization (θ_H = 0 °) whereas the other one has DC field in perpendicular to the internal magnetization (θ_H = 90 °).

When θ_H equals 0 °, the FMR frequencies increase linearly as external DC magnetic field increases. When θ_H equals 90 °, as the external DC field increases, the magnetization was changed from along wire axis direction to perpendicular to the axis direction. Therefore, the FMR frequencies decreases first and then increases. The experimental study of MNWs in chapter 3 and chapter 4 are primarily performed in these two orientations.

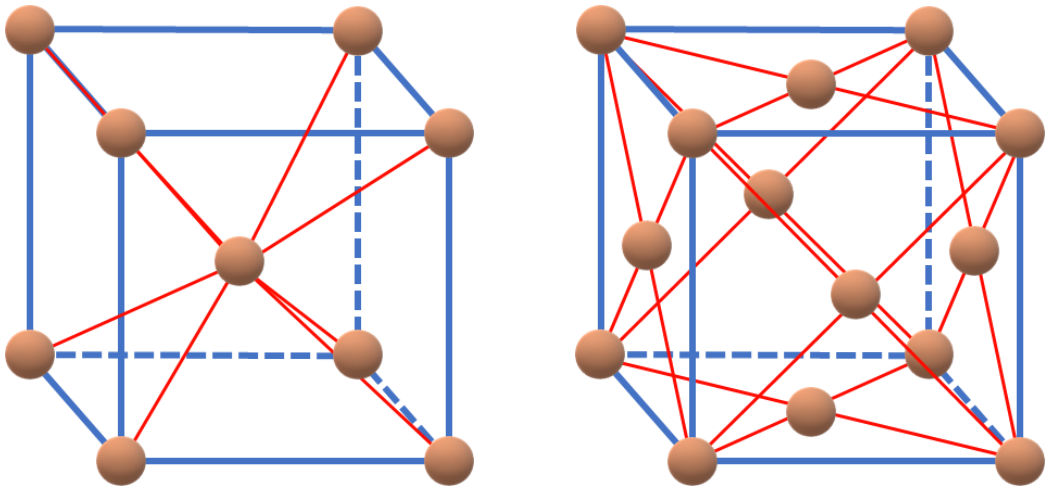

(a) (b)

Fig 2.3. Crystalline structure for magnetic material. (a) Body centered cubic structure for Fe. (b) Face centered cubic structure for Ni.

In this work, three focused material are Co, Ni and Fe. Fe and Ni MNWs possess body-center cubic (bcc) (Fig 2.3a) and face-centered cubic (fcc) crystalline structure (Fig 2.3b), respectively. All Co MNWs are fabricated in a precursor solution with pH = 2, which creates heavily faulted fcc crystalline structure [31]. Due to the fcc and bcc crystalline structure properties, all materials used in this work possess weak crystalline anisotropy field, which can be ignored in the Kittel equation calculation. In [31], a simplified equation 2.2 was shown to represent the case at θ_H= 0° with H_u =0, which will be used a lot in this thesis.

$$\omega_{FMR} = \gamma * (H + 2\pi M_s - 6\pi M_s P) \tag{2.2}$$

In equation 2.2, M_s is saturation magnetization, P is porosity and H is external DC field. For Co, Ni and Fe, M_s values are 1440 emu/cc, 485 emu/cc and 1707 emu/cc, respectively. P is porosity. At θ_H= 0°, the FMR frequencies calculated using equation 2.1 and equation 2.2 have the similar results. The value of $-6\pi M_s P$ in equation 2.2 is the term that describes the dipolar interaction field (H_{dip}).

Based on the Kittel equation, the FMR frequencies at different orientations can be predicted. To obtain more parameters for FMR response study such as the susceptibility and linewidth of single and arrays of MNWs, OOMMF and NMAG models will be discussed next.

2.2.2 Simulation of single MNWs using OOMMF

A typical MNW requires aspect ratio between length and diameter greater than 10, which allows shape anisotropy along with the wire axis. OOMMF is able to model a single MNW with high aspect ratio and therefore is used to model its FMR response.

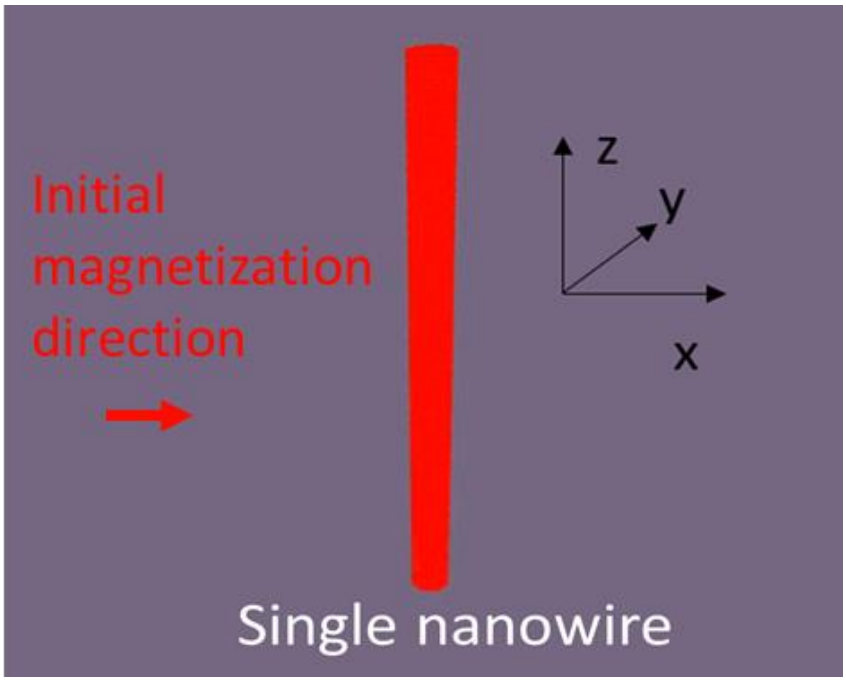

Fig 2.4. Simulated single Co MNW using OOMMF.

In Fig 2.4, a single Co MNW model with a typical NW diameter of 40nm and length of 800 nm in OOMMF is shown. The aspect ratio between length and diameter is chosen to be 20. The moment of MNW, shown in red, is set in x direction and as the initial magnetization (M) state. To simulate FMR response, the steady state needs to be identified. In Fig 2.5, when the simulation begins, the normalized magnetization in x and y direction starts from maximal value 1 and decreases to zero with damping effect, whereas in the z direction, the normalized magnetization increases from 0 to 1. The time point when the magnetization in x and y direction (Mx and My) reaches zero was called steady state. In this state, the magnetization aligns to the wire axis due to the shape anisotropy field.

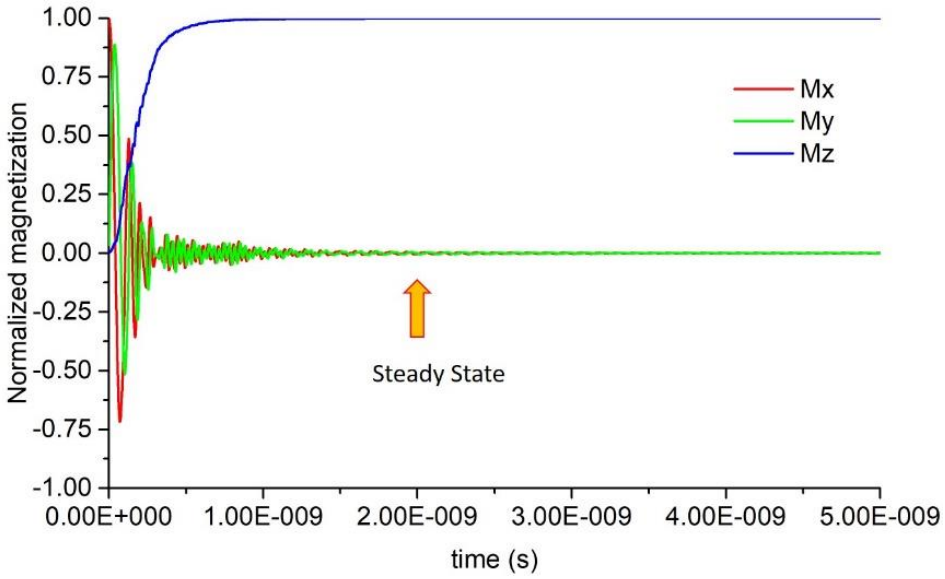

Fig 2.5. Magnetization response in x, y and z direction. Mx, My and Mz are magnetization in x, y and z direction, respectively.

Next, add a pulsed AC field in the y direction and calculate the susceptibility: $\chi = \frac{M(\omega)}{H(\omega)} = \chi'(\omega) - j\chi''(\omega)$. In this susceptibility equation, $M(\omega)$ and $H(\omega)$ are magnetization and AC magnetic field in frequency domain, respectively. $\chi'(\omega)$ and $\chi''(\omega)$ are real and imaginary part of susceptibility in frequency domain, respectively. By plotting $\chi'(\omega)$ and $\chi''(\omega)$ with respect to the frequency in x or y direction, the FMR frequencies can be obtained by the peak or the dip of $\chi''(\omega)$. See Appendix A for detail FMR simulation procedure.

In Fig 2.6, the susceptibility (χ' and χ'') is shown for Co MNWs with 0.2 T external DC field in x direction. Two FMR frequencies can be obtained from χ'': 8.77 GHz and 30 GHz. The FMR frequency at the lower band, 8.77 GHz, is defined as end mode and corresponds to the domain wall resonance at the end of single MNW. The frequency at the higher band, 30 GHz, however, is defined as the bulk mode and corresponds to the magnetization resonance in the bulk of the MNW region. The bulk mode is the primary

FMR frequency and is stronger compared to the end mode. The linewidth of the bulk mode indicates the loss of material and is 1.08GHz, which is obtained from the full width maximum of χ''.

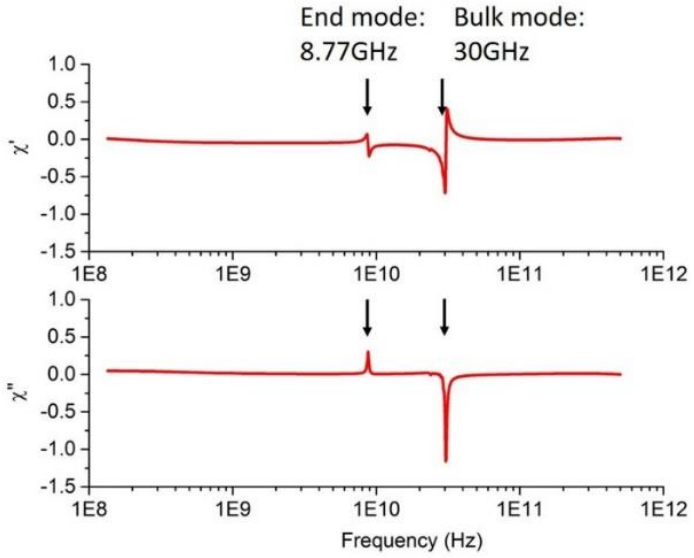

Fig 2.6. Real and imaginary part of susceptibility for single Co MNW in x direction with external DC field of 0.2T.

While OOMMF can simulate single wire behavior accurately, it cannot consider multiple wires due to a lack of periodic boundary conditions. In chapter 2.2.3, the FMR performance of MNW arrays will be simulated using NMAG.

2.2.3 Simulation of MNW arrays using NMAG

Herein, NMAG was used to simulate the FMR response of array of MNWs due to its periodic boundary function, which can be used to simulate the dipole interaction between individual MNWs inside the array accurately.

In Fig 2.7, a top view of a 100 by 100 Co MNW array simulated in NMAG is shown with length of 800 nm and diameter of 40 nm. A 0.2T DC field is added along with wire

axis or normal to the page. The simulation procedure using NMAG is similar to that of using OOMMF. See Appendix A for detail simulation procedure.

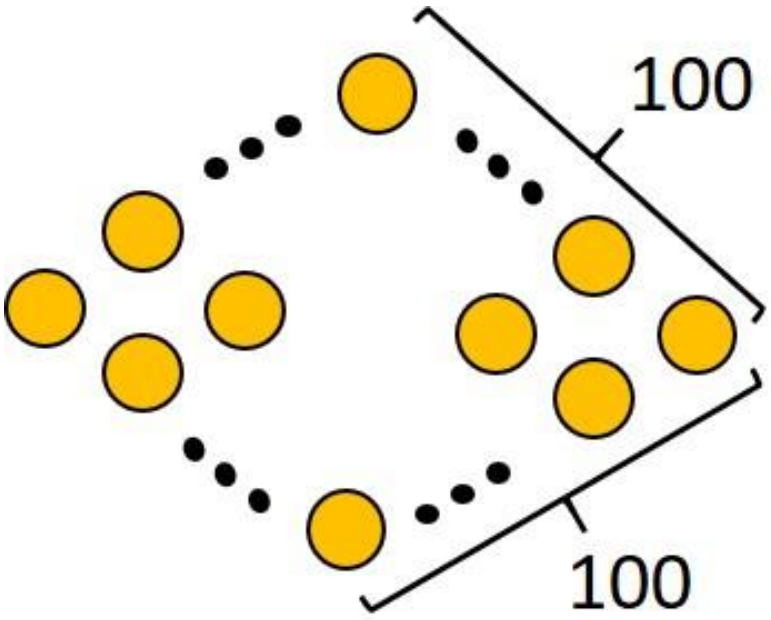

Fig 2.7. Top view of MNW array modeled in NMAG.

The susceptibility plots for χ' and χ'' are shown in Fig 2.8. The end mode and bulk mode for Co MNW array are 5 GHz and 21.7 GHz, respectively. However, both FMR frequencies for end and bulk mode are lower than that of the single MNW results simulated by OOMMF. This relationship can be explained using equation 2.2, where the FMR frequency of the MNW array decreases due to the dipolar interaction field. The linewidth of bulk mode from Co MNW array is 1.3GHz.

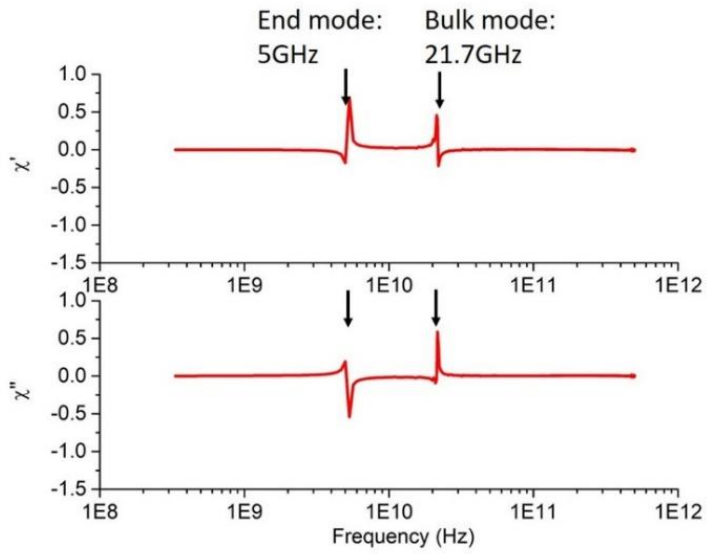

Fig 2.8. Real and imaginary part of susceptibility for array of Co MNWs in x direction with external DC field of 0.2T.

2.3 RF models for Cu NW application in HFSS

In this work, Cu NWs are used to form integrated vertical vias.

NWs that grown in a porous integrated template such as integrated anodized aluminium (iAAO) usually possess nanometer-sized wire diameter and 1-to-2-micron sized thickness. Bundles of NWs can provide vertical connection between top and bottom transmission lines and form the vias.

Herein, a coplanar waveguide (CPW) structure shown in Fig 2.9 is used to be the standard transmission line type. From Fig 2.9, a CPW line has one signal line (S) in the middle and two ground (G) in the same plane of S. The signal line width (W), slot width (g) and ground plane width (Wg) are designed to be 93.9 μm, 53.05 μm and 400 μm, respectively. The impedance is designed to be 50 Ω. The total CPW width which equals W+2*g+2*Wg is designed to be 1000 μm to guarantee that the single mode operates up to 60 GHz.

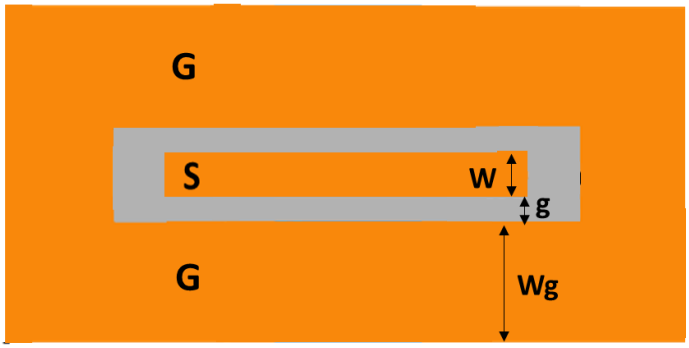

Fig 2.9. Top view of a standard CPW line. S and G represent signal line and ground plane region, respectively. W, g and Wg are signal line width, slot width and ground plane width, respectively.

The via design based on CPW structure is shown in Fig 2.10. NW vias described by via width (VW) and via length (VL) are located on S and G plane. Two G-S-G NW vias are included in a two-port transmission line as interconnect between top and bottom CPWs. The signal transmission path, shown in Fig 2.9b, is going through top CPW, first NW vias, bottom CPW, second NW via and back to the Top CPW.

CPW line with NW via design needs to be modeled in Ansys HFSS (High Frequency Structural Simulator) [32]. However, due to the large size difference between NW vias and CPW circuit, high computation time is required to model the proposed structure accurately. Therefore, a micron-sized Cu pillars model are used to approximate NW via performance.

In Fig 2.11, top view of CPW with NW via modeled in HFSS is shown. Assuming the NW grown in iAAO has the porosity of 9%, which means the total Cu area over iAAO region is 9%. The area of Cu pillar area over iAAO in HFSS should also be 9% to approximate the RF performance based on metal volume. To save computation time, 5.5 µm by 5.5 µm Cu pillar are used in the via region. The interwire distance is 17.5 µm to

keep the division between Cu pillar area and via area to be 9%. The total circuit length is 1220 μm. VL is 90 μm. VWs on the S and G plane are the same as W and Wg, respectively.

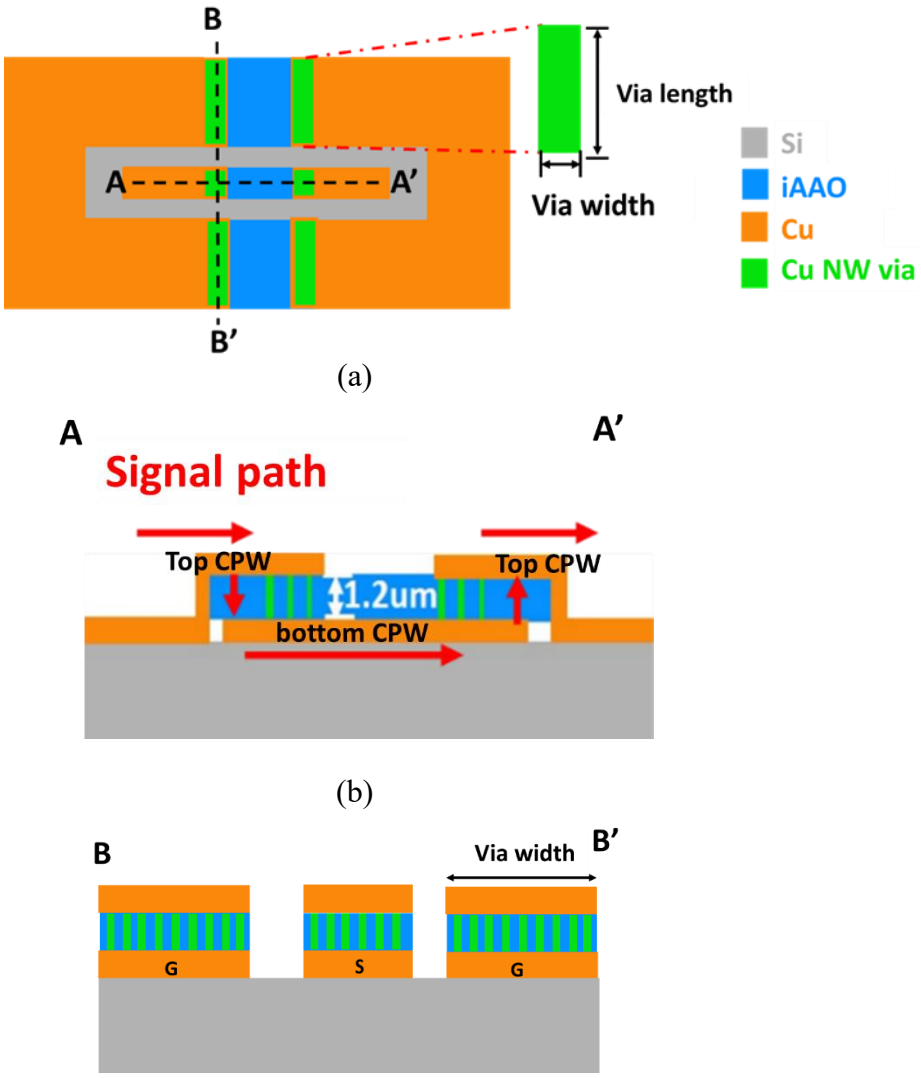

Fig 2.10. Top view and cross section of via design in CPW circuit. (a) Top view of CPW with NW via. (b) Cross section of CPW with NW via at AA' direction. (c) Cross section of CPW with NW via at BB' direction.

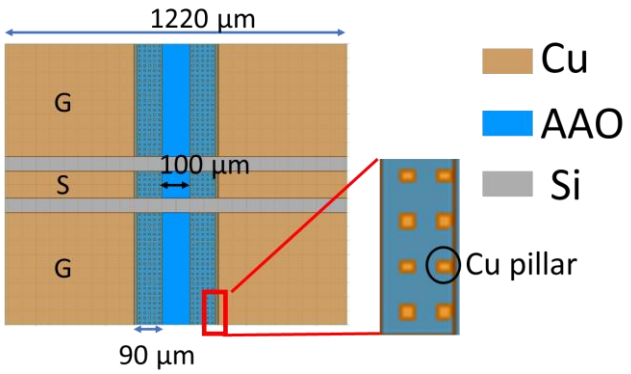

Fig 2.11. Top view of CPW with NW via modeled in HFSS. The via region are simulating using micron-sized Cu pillars.

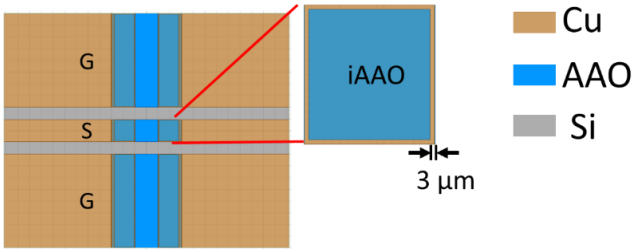

(a)

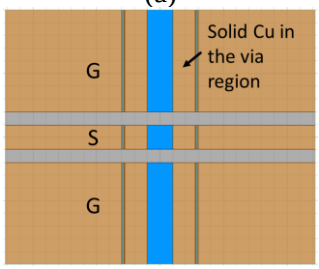

(b)

Fig 2.12. Two reference vias for NW via study. (a) Top view of conventional vias in CPW; (b) Top view of solid Cu via in CPW.

Based on same via and CPW dimensions, another two types of vias are designed as reference for NW vias, shown in Fig 2.12. One is the conventional via (Fig 2.12a) that is formed by the connection at the edge of vias between top and bottom CPW. The edge width is designed to be 3 mμ to make area of Cu connection to be 9 % of iAAO area. The other one is the solid Cu via (Fig 2.12b) that is formed by solid metal bulk in the via region.

The simulation results of NW vias and two reference vias are shown in Fig 2.13. The CPW with NW vias shows decent signal transmission and low reflection coefficient with the S21 value of

-0.35 dB and S11 value of -46 dB at 40 GHz, respectively. The performance of CPW with NW and conventional vias are close. Below 30 GHz, the solid Cu via shows the best S21 performance due to the highest volume of metal in the via region and largest area for current to flow through. Above 30 GHz, due to skin depth effect, the S21 of Cu solid via decreases and aligns with the NW and conventional via.

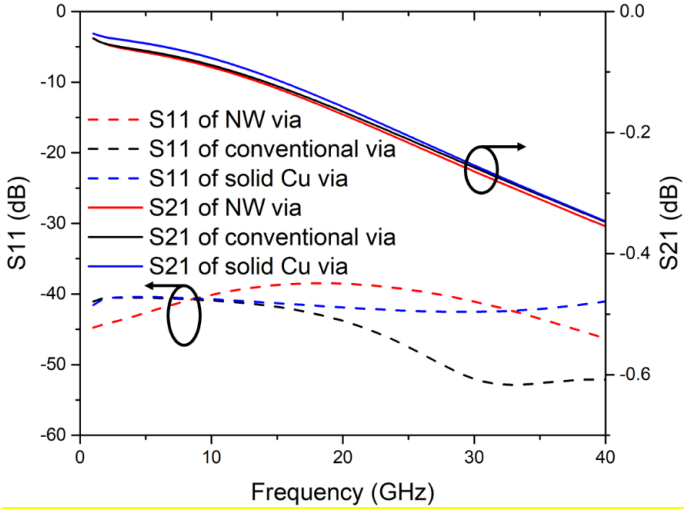

Fig 2.13. Comparison of NW, conventional and solid Cu vias.

2.4 Summary

In this chapter, the simulation and modeling of MNWs and Cu NWs are shown. The FMR theory and simulation of MNWs are studied. Kittel equation is used to predict the FMR frequencies of MNWs but cannot show the linewidth and susceptibility. By using two micromagnetic software tools, OOMMF and NMAG, the end mode and bulk mode of single and array of MNWs are presented. Compared to a single MNW, array of MNWs

shows lower FMR frequencies for both bulk mode and end mode due to dipolar interaction field. The linewidth of single and array of NWs can be predicted which indicates system detection resolution. A complete theory and model study for FMR of MNWs was presented. This will be used to guide the experimental MNWs characterization in Chapter 3 and 4.

The Cu NWs are designed as vertical vias. By using a micron-sized model with 5.5 μm by 5.5 μm Cu pillar and 17.5 μm interwire distance, Cu NWs vias in a CPW line can be simulated in HFSS. Then, the NW via is compared to a conventional via and a solid Cu via. NW and conventional via shows close performance across the band. For solid Cu via, it shows best performance below 30 GHz due to the highest metal volume. When above 30 GHz, the performance of solid Cu via is degraded and aligned with the results of NW and conventional vias due to skin depth effect. Based on the simulation CPW with Cu NW via model, the proposed structure is going to be designed, fabricated and measured in chapter 5.

Chapter 3 MNW characterization for biolabeling applications

3.1 Introduction

Magnetic nanowires (MNWs) are studied for use as bio labels for different type of cells, molecules, and sub-cellular structure. The antibody corresponding to one type of cells can be tagged to one type of MNW. By using ferromagnetic resonance (FMR) techniques, the different types of MNWs can be detected and identified. Therefore, different types of cells can be detected and identified. For example, nickel (Ni) nanowires (NWs) and iron (Fe) NWs can correspond to a cancer and healthy cell, respectively. By detecting Ni NWs FMR frequencies, cancer cells can be identified.

To apply MNWs for biolabeling system, the FMR frequencies and variable that influences them needs to be studied. Thus, circuits that can provide AC fields are needed. Waveguide cavity [33], microstrip [34] and coplanar waveguide (CPW) [35] are typical microwave circuit transmission line technology that can provide an AC magnetic field with MNWs. CPW is a broader band design. It offers large measurement frequency range and ease of use with measurement samples compared to waveguide cavity, which is bandwidth limited. CPW also provides a stronger AC magnetic field on top of the circuit board, which is desirable for sample characterization, compared with microstrip, whose fields are primarily in the substrate.

The most common used FMR measurement approaches include lock-in detection method [36], pulse perturbation method [37], and VNA-FMR method [38]. Herein, the VNA-FMR method is used and adopted for use with both short-circuited and through-line

CPW measurement circuits. The FMR characterization of MNWs, tri-labeling system and MNWs inside biological samples are studied.

3.2 MNW sample fabrication process and dimension description

In chapter 3, two types of templates are used, anodized aluminum oxide (AAO) and polycarbonate

For both templates, a 17 nm Ti and 300 nm Cu layer are deposited on the one side of template as electrode for chemical electrodeposition process [9], shown in Fig 3.1.

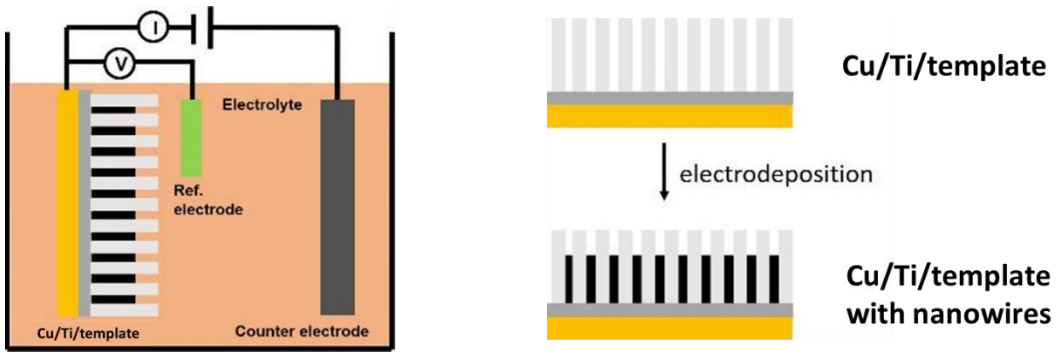

Fig 3.1. Fabrication process for MNW samples.

Three types of material are used. They are Cobalt (Co), Ni and Fe. For all Co MNWs, the precursor electrolyte has pH of 2, which means heavily faulted fcc crystalline structure is created. One example of fabricated Co MNWs grown in AAO with NW diameter of 40 nm and porosity of 12 % is shown in Fig 3.2.

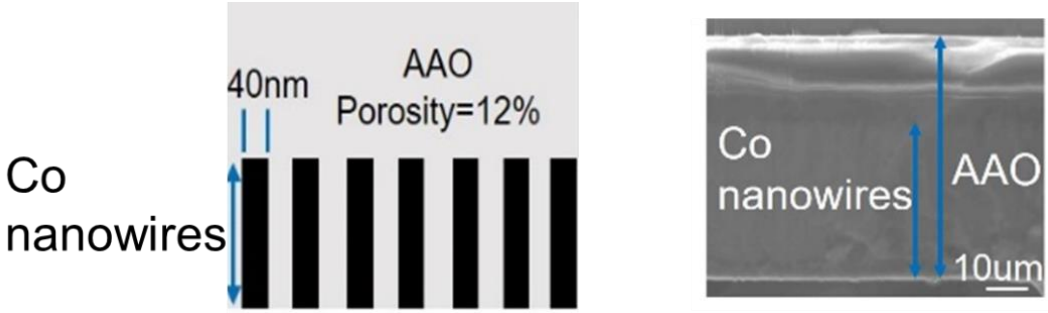

Fig 3.2. Cross-section of Co NWs in AAO (left) and scanning electron microscopy (SEM) image of Co NW in AAO (right).

TABLE 3.1
DIMENSIONS OF MNW SAMPLE

Template	Material type	Sample order	NW length (μm)	NW diameter (nm)	Porosity	Diced or not	Chip length (mm)	Chip width (mm)
AAO	Co	Co72-small	15.5	40	12%	yes	1.958	0.331
		Co72	15.5	40	12%	no	N/A	N/A
		Co80	28.2	40	12%	yes	3.689	0.423
		Co114-small	0.534	40	9%	yes	0.220	1.875
		Co114-medium	0.534	40	9%	yes	0.481	1.875
		Co114-large	0.534	40	9%	yes	3	1.875
	Ni	Ni62	18	80	15%	no	N/A	N/A
	Fe	Fe49	10.5	40	12	no	N/A	N/A
Poly-carbonate	Ni	N/A	3	100	2.4%	no	N/A	N/A

The dimension information of MNW samples used in Chapter 3 is shown in Table 3.1. All diced sample are first attached to a Si wafer with photoresist as adhesion and then diced into rectangular shape using wafer dicing saw.

3.3 FMR characterization system and measurement set-up

The FMR characterization system is shown in Fig 3.3 [39]. The NW samples are placed above a CPW circuit, which provides an AC magnetic field to the test sample. The circuit is then put between two electromagnet poles, which provides a DC magnetic field. An Anritsu 37369D vector network analyzer (VNA) is used to provide the AC signal and detect the FMR response using reflection coefficient (S11) or transmission coefficient (S21). In addition, the measurements in this chapter are performed in the DC field domain, where the AC field is fixed with discrete frequency in the range of 0.04-40GHz and the DC field is swept from +1.5T to -1.5T with the rate of 0.025T/s in all measurements.

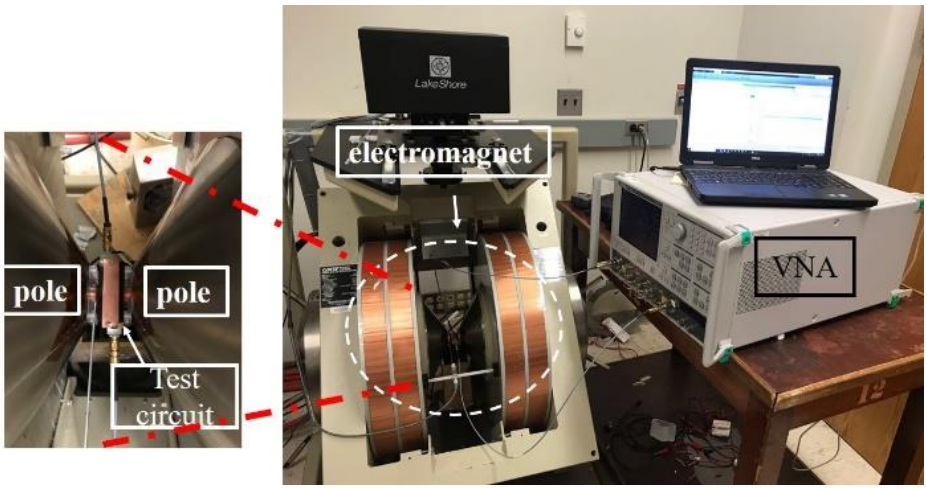

Fig 3.3. Test circuit between two poles (left) and FMR characterization system set-up with electromagnet and VNA (right).

One-port and two-port CPW circuits, shown in Fig 3.4a and Fig 3.4b, respectively, are used and designed on Rogers10 mil Duroid 5880LZ (ε_r = 2) [40] with signal line width of 16.5 mil and slot width of 5 mil. The trace length is 7.8 mm for the one-port circuit and 6.8 cm for the two-port circuit.

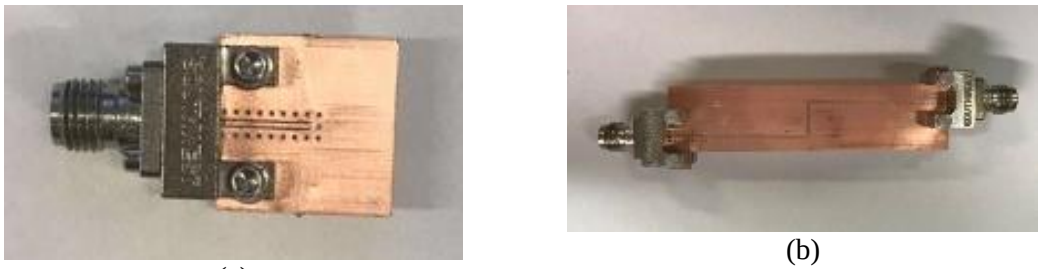

(a) (b)

Fig 3.4. (a) One-port short-circuited CPW board, (b) two-port through-line CPW board.

In this work, MNW samples are measured in two orientations based on the DC field direction, out-of-the-plane (OP) and in-the-plane (IP). The DC field direction is along the wire axis for OP orientation and perpendicular to the wire axis for IP orientation.

To reduce the interference from the testing system, nonmagnetic cables (Cinch Connectivity Solutions [41]) were used. The flexible nonmagnetic cables, however, were

sensitive to bending compared to the semi-rigid measurement cables during calibration. Thus, both one-port and two-port measurements were referenced at the VNA ports.

Typical FMR detection measurements are obtained for DC magnetic field direction in the out-of-plane (OP) direction and in-plane (IP) direction. The DC field and AC field distribution are shown in Fig 3.5. In OP orientation, both one-port and two-port circuits have DC fields perpendicular to the AC fields. In IP orientation, DC field is always perpendicular to the AC fields for two-port circuit, whereas DC field is perpendicular to AC field in the slot only for one-port circuit.

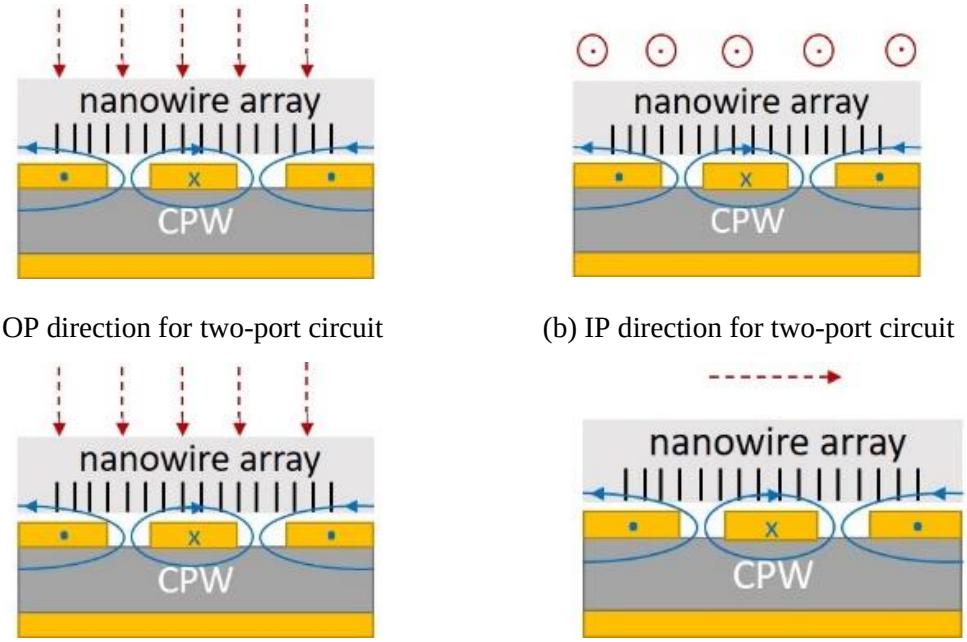

(a) OP direction for two-port circuit

(b) IP direction for two-port circuit

(c) OP direction for one-port circuit

(d) IP direction for one-port circuit

Fig 3.5. A schematic of the cross sections of CPW boards to show field distribution in OP and IP direction. The red dashed line and red circle represent the DC field direction, the blue solid line represents the AC field direction, and the black line is NW axis. All cross sections are from the middle of the one-port and two-port circuits.

3.4 FMR characterization method

Two FMR characterization methods are going to be introduced, compared, and discussed in this section. They are magnitude method and phase analysis method (PAM).

3.4.1 Magnitude method

Magnitude method is defined as describing the FMR response by using the magnitude of S11 or S21 data. Using magnitude method, FMR frequencies can be acquired by the minimum value of magnitude of S parameters. Next, the FMR response acquired using magnitude method and its comparison with theory will be shown.

3.4.1.1 FMR measurement and theory comparison

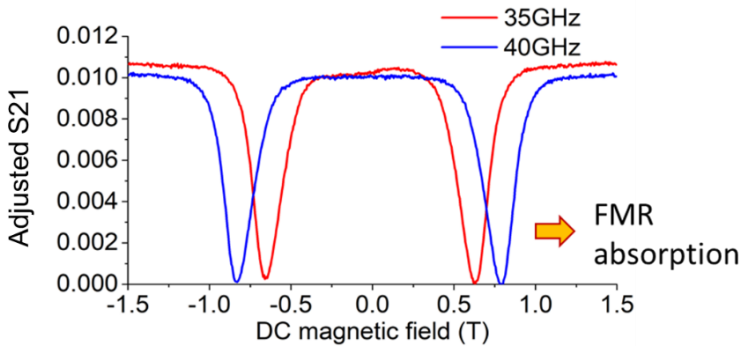

Fig 3.6. FMR response of Co72 in OP orientation.

Herein, Co72 NWs that grown in anodized aluminum oxide (AAO) template with porosity of 12%, length of 15.5 μm and 40 nm is used. The FMR response of Co72 on two-port CPW circuits is shown in Fig 3.6. The frequencies of FMR absorption can be obtained by the minimum of adjusted S21. The adjusted S parameter is defined in equation 3.1.

$$\text{Adjusted S21} = |S21| - \min(|S21|) \tag{3.1}$$

where |S21| is the magnitude of S21 and min(|S21|) is minimum value of |S21|. The FMR frequencies of Co72 at 35 GHz and 40 GHz are obtained for positive DC field of 0.63 T and 0.785 T, respectively.

To confirm the accuracy of experimental FMR frequencies obtained from magnitude method, the comparison of measurement, Kittel equation and NMAG modeling of FMR frequencies in OP orientation for Co72 is shown in Fig 3.7. In the measurement, the DC fields are acquired with FMR frequencies at 20 GHz, 25 GHz, 30 GHz, 35 GHz and 40 GHz. The theoretical FMR frequencies is calculated using Kittel equation 2.2 with external DC field in the range of 0-0.9T. A FMR frequency obtained from NMAG simulation using χ'' curve at 0.2 T DC field is included and shown as blue star. There is a good agreement between all data.

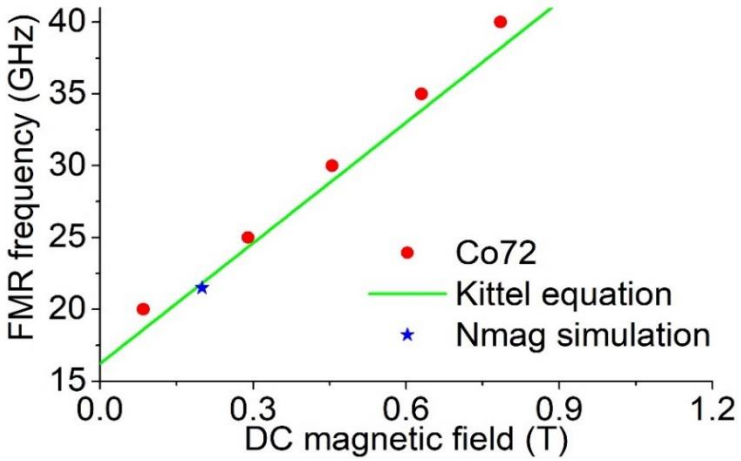

Fig 3.7. Comparison of FMR measurement, Kittel equation and NMAG modeling of Co72 in OP orientation.

Four 3D printed fixture were designed, fabricated, and used to measure the FMR frequency for θ_H at 90 ° (IP), 60 °, 30 ° and 0 ° (OP), where θ_H is the angle of external DC field with respect to the wire axis. The measurement results, shown in Fig 3.8, show similar trends to Kittel equation results in Fig 2.2. At 0° (OP), the FMR frequency increases

linearly with DC field strength, whereas at 90° (IP), FMR frequency shows minimum value around 0.65 T. A gradual transition between OP and IP can be observed at 30° and 60°. Since magnetization prefers to align with the wire axis due to the strong shape anisotropy presented in the NW array, lower DC fields are needed to observe FMR in OP direction. As the angles of the DC field perpendicular to the wire axis increase, magnetization takes higher DC field to rotate and achieve saturation.

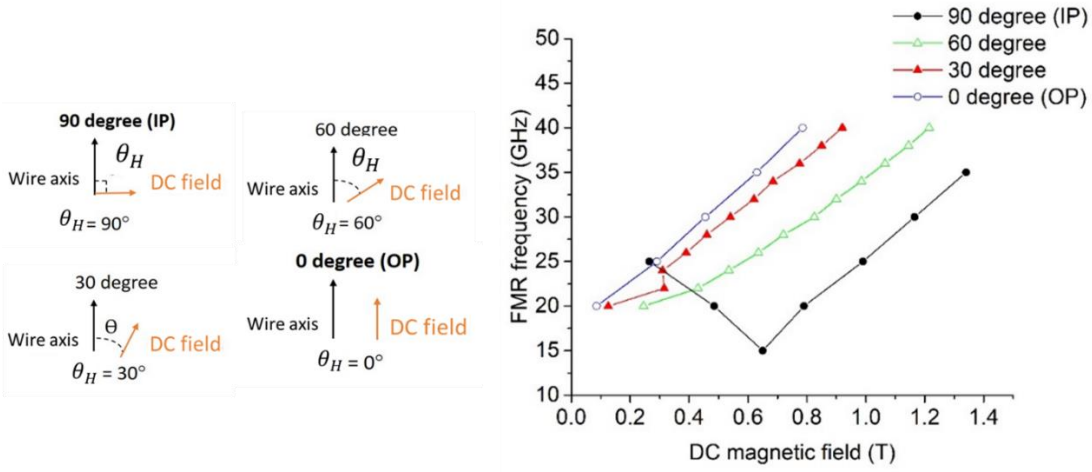

Fig 3.8. The FMR frequency versus DC field pattern at 0° (OP), 30°, 60° and 90° (IP).

Some biomedical applications, like bio-labels, requires small volume of material. Therefore, methods that detect low FMR signal are needed.

3.4.1.2 Signal enhancement study

To enhance the ability to detect small volume material and low FMR signal, Cu back layer effect and position effect are studied.

3.4.1.2.1 Cu back layer effect

Since a 17 nm Ti and 300 nm Cu layer are deposited as electrode on the one side of MNWs, the effect of the Cu back layer is studied using the electrode [42].

A MNW sample called Co72-small, is diced into a rectangular with length of 1.958 mm and width of 0.331 mm. The diced Co72-small was placed across the CPW test circuit, which includes the slot and the signal line, with and without Cu back layer. In Fig 3.9, the FMR measurements are observed for Co72-small with and without Cu back layer. The sample with Cu layer creates almost seven times stronger FMR signal compared to the sample without Cu back layer. In Fig 3.10, HFSS simulation results are used to explain this effect.

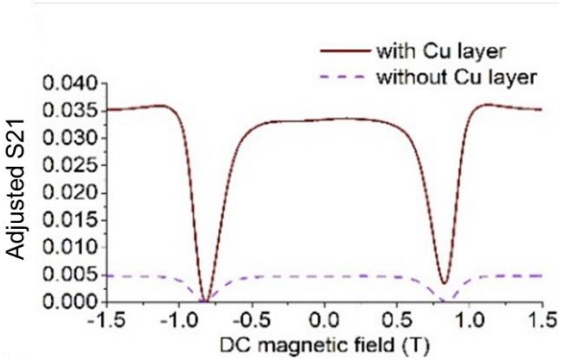

Fig 3.9. The comparison between the Co72-small sample chip with and without Cu back layer at 40GHz in OP orientation.

(a) (b)

Fig 3.10. The HFSS simulation for sample without and with Cu back layer. Red and green arrows represent the AC field strength of 316A/m and 190A/m, respectively. (a) Cross section of sample on CPW. (b) Cross section of sample on CPW with Cu back layer

Without Cu layer, the AC fields are concentrated inside the CPW slots, whereas with Cu layer, the AC fields are concentrated above the signal line due to the transfer of electric field attraction from the CPW grounds to sample Cu layer. The Cu layer acts like a floating ground and is closer to the signal line above the sample. Thus, by including a Cu back layer to the MNW sample, the FMR response is further enhanced.

3.4.1.2.2 Position effect

CPW line has different AC fields distribution around slot and signal line. Therefore, the position effect is studied here by putting sample on the slot and signal line [39].

Co MNW sample, Co80, grown in 50 μm AAO with 12% porosity, 40 nm diameter and NW length 28.2 μm, is used. The Co80 NW sample is diced into a narrow rectangular shape with length of 3.698 mm and width of 0.423 mm. A CPW line is used as test circuit with a signal line width of 391 μm and slot width of 150 μm (Fig 3.11). The DC fields are applied along the signal line. The AC fields are perpendicular to the signal line direction on the signal line region and normal to the page in the slot region.

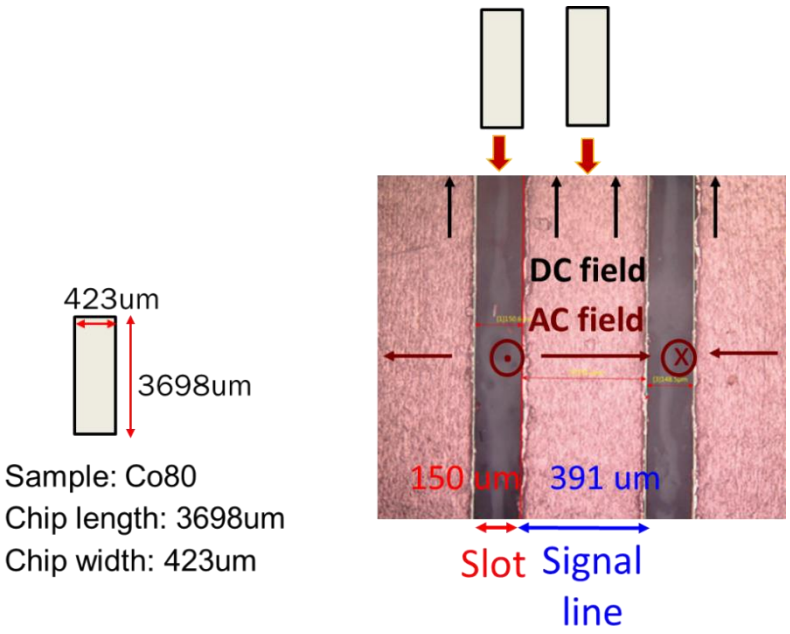

Fig 3.11. Diced Co 80 sample (left) and top view of CPW line with Co80 (right).

The Co80 sample was put on the slot or on the signal line of two-port CPW circuit, shown in Fig. 3.11, to measure FMR response. The measurements are performed in IP orientation. In Fig 3.12, the FMR frequencies versus DC field in IP direction is plotted. In IP orientation, magnetization initially align with wire axis and perpendicular to the DC fields. As DC field increases, magnetization rotate and gradually align with DC field direction. The region that magnetization is rotating and not fully saturate in DC field direction is called low DC field region, whereas the region that magnetization is align with DC field direction is called high DC field region. The low DC field and high DC field regions are separated by a transition point at 15 GHz, where the magnetization is at exact saturation point.

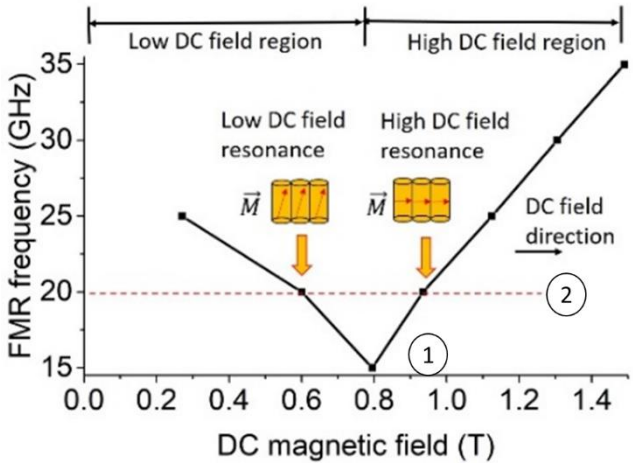

Fig 3.12. FMR frequency versus DC field in IP direction.

First, FMR measurement on the slot and on the signal line on two-port CPW in IP orientation is performed at 15GHz, shown in Fig. 3.13. Since the magnetization is at exact saturation point at 15 GHz, magnetization direction is perpendicular to the AC fields both in the slot and on the signal line. The FMR absorption for the sample placed on the slot is stronger than placed on the signal line. This is due to the stronger AC field around the CPW slot (Fig 3.10a). Thus, to enhance FMR response, the sample chip should be placed on the slot.

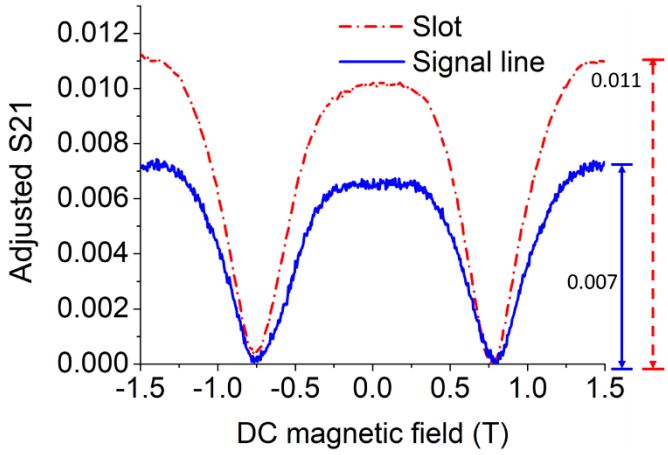

Fig 3.13. The comparison between the Co80 sample on the slot and on the signal line at 15GHz in IP orientation.

Secondly, The Co80 sample is measured in IP direction at 20 GHz, where the red dashed line intersects with a black line at two FMR frequencies (Fig 3.12). The optimal angle between AC field and magnetization for detecting the FMR frequency can be obtained.

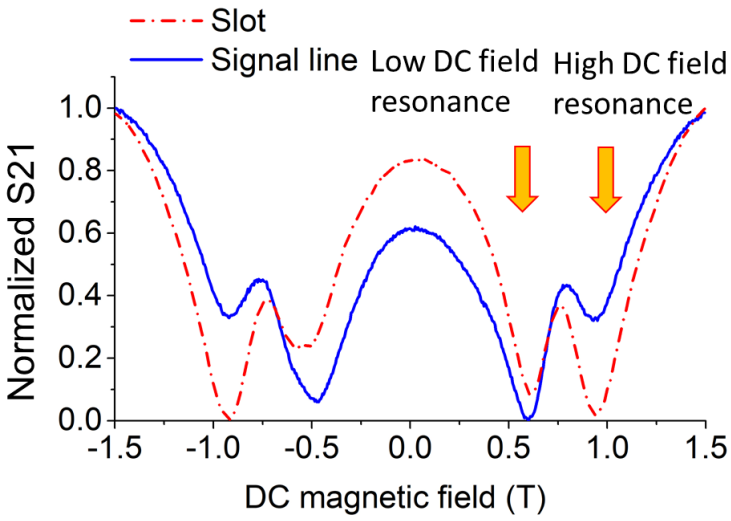

Fig. 3.14. The comparison between the sample on the slot and signal line at 20GHz in IP direction.

In Fig 3.14, there are two FMR absorptions in IP orientation regardless of sample placement on the slot or signal line. One absorption occurs in the low DC field region where the NW magnetization is dominated by shape anisotropy effect and the other occurs in the high field region where the magnetization is aligned with DC field in IP orientation. To better compare the signal strength relationship between two FMR absorptions from two positions, the FMR response is expressed using normalized S21 in Fig 3.14, which can be defined in equation 3.2.

$$\text{Normalized S21} = \frac{S21 - \min(S21)}{\max(S21) - \min(S21)} \qquad (3.2)$$

The max(S21) and min(S21) are maximum and minimum of S21.

When the sample is on the signal line, the AC field is orthogonal to the magnetization in both low and high DC field regions. When the sample is on the slot, however, the AC field is orthogonal to magnetization in the high DC field region but close to parallel in the low field region. Unfortunately, the non-orthogonality between AC field and magnetization in the low field region leads to the weaker absorption which flips the strength relationship between the low field resonance and high field resonance. Thus, for efficient absorption of FMR, AC field should be perpendicular to the magnetization.

In summary, from position effect study, two approaches can be used to enhance FMR absorptions. The first one is putting the MNW sample on the slot rather than on the signal line; the second one is to make AC field be perpendicular to the magnetization of measured MNWs.

3.4.1.3 Small signal analysis study

For biolabeling application, small volume of material is expected for in situ experiments. Therefore, the smallest detectable signal level and MNW volume need to be determined and investigated for our set-up. Since one-port short circuited CPW and two-port thru line CPW are used for FMR measurement, the one that provides the more sensitive detection needs to be determined among two. And the small signal analysis will be investigated based on the circuit that provide most sensitive detection. So, the comparison of one-port short circuited CPW and two-port thru line CPW is needed.

3.4.1.3.1 One-port short-circuited versus two-port thru line methods

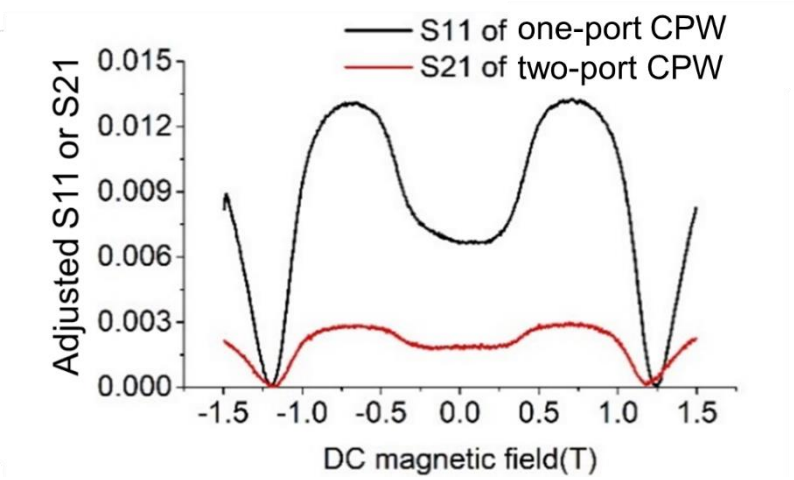

Fig 3.14. The FMR measurement of the Co72 on two-port CPW and short-circuit CPW at 26GHz in IP orientation.

Fig 3.14 shows the FMR response of diced Co72-small in the DC field domain. The adjusted S21 and S11, ratio between input and output voltage of two-port and one-port CPW, are used to express the FMR response. Adjust S21 can be calculated using equation 3.1, whereas adjusted S11 can be calculated using equation 3.3.

$$\text{Adjusted S11} = |S11| - \min(|S11|) \tag{3.3}$$

|S11| is magnitude of S11 and min(|S11|) is the minimum of |S11|.

From two-port and short-circuited CPW, the FMR response are similar and FMR frequencies align well with each other. This means both methods can be used to characterize FMR response with constant FMR results. The FMR absorption measured from short-circuited CPW, however, is much stronger than the one from the two-port CPW. This occurs because the short-circuited CPW has a shorter signal traces and uses one cable to obtain the data. These provide shorter signal path with less insertion loss. Also, it allows AC signal to pass the MNW sample twice to measure the FMR response. Therefore, the

short-circuited CPW will be used to study the volume effect of MNWs and to determine the smallest detectable signal level and material volume.

3.4.1.3.2 Volume effect

Volume effect is studied based on a small volume MNW sample. The sample with low porosity and short NW length is preferred to reduce the material volume [43].

Herein, Co114 is grown in 50 µm thick AAO with porosity of 9%, with NW diameter of 40nm, and NW length of 0.534µm. The NW length is designed to be as short as possible to reduce the volume of material but 10 times larger than the diameter to guarantee that high shape anisotropy is still along the wire axis. Three chips are diced from Co114: large, medium and small with a chip width of 1.875 mm and chip lengths of a) 3 mm, b) 0.481 mm and c) 0.220 mm, respectively. The large, medium and small chip volumes are $3x10^{-3}$ mm^3, $4.8x10^{-4}$ mm^3 and $2.2x10^{-4}$ mm^3, respectively.

The short-circuited test line with medium chip is shown in Fig 3.15. The sample is put across both signal line and slots of CPW lines. FMR absorptions were measured in the OP direction.

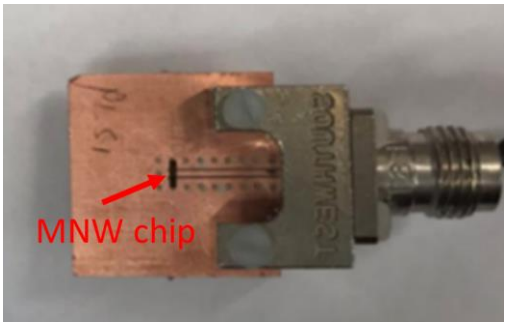

Fig. 3.15. Short-circuited CPW test circuit with Co114 (1875 µm x 481 µm).

To determine the accuracy of FMR frequencies from three MNW volume test chips, a comparison is needed between the experimental results and theoretical predication. In Fig 3.16, the FMR response for different volumes chips is compared with the Kittel equation for Co from equation 2.2.

The goal is to identify how experimental FMR data deviates from the Kittel equation by comparing a mean difference between the measured and the predicted frequencies. Eight FMR data points are collected for each chip. At each DC field, the difference between the predicted and measured FMR is computed. Next, these differences are summed and divided by the total number of data points to produce an average frequency difference value between measured and predicted results, defined as mean difference of FMR frequencies. The ideal mean difference value should approach zero. The large chip FMR response mean difference is 0.865GHz and agrees well with the Kittel equation. The medium and small chips FMRs diverge more from the Kittel equation and have mean differences of 1.855GHz and 2.205GHz, respectively. Both are more than twice the value of the large chip mean difference. Fig 3.17 will be used to explain the results.

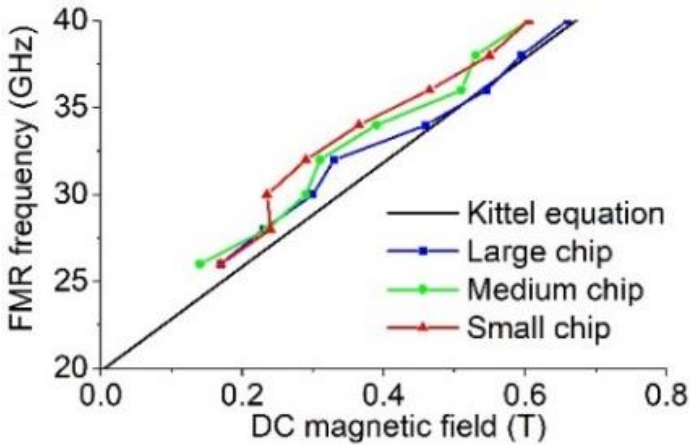

Fig 3.16. The comparison of experimental FMR response and Kittel equation (P = 9%) in the OP orientation.

In Fig 3.17a, as the volume of material decreases, the adjusted S11 magnitude, corresponding to FMR response, reduces and indicate the lower absorption. Fig 3.17b shows the data after smoothing. In Fig 3.17b, the FMR frequency points, based on the minimum value of the curve, vary for different volume chips. This is due to constant VNA noise power. Hence, as chip volume is reduced, the signal to noise (SNR) ratio decreases which introduces higher error when extracting the FMR frequency value. Therefore, the medium and small chip diverge more from the Kittel equation than the large chip.

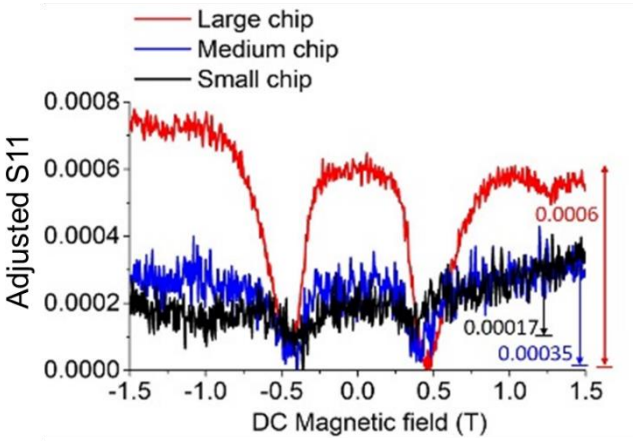

(a)

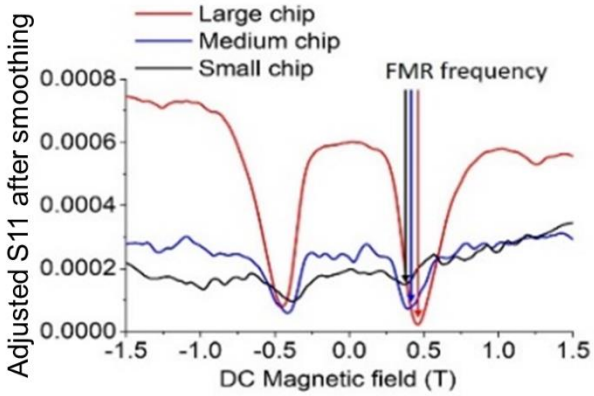

(b)

Fig 3.17. The FMR response for three volumes of Co114 at 34GHz in the OP orientation. (a) The plot of adjusted S11. (b) The adjusted S11 with smoothing span value of 0.07.

Since the lowest VNA detectable signal strength (S11 or S21) is 0.0002, the small chip's signal strength, around 0.00017, is below the detection limit. Thus, the FMR error is expected to be high and is confirmed with the mean difference calculations, as discussed previously. To detect FMR response accurately for this VNA system, the Co volume and magnetization should be greater than that of small chip, $2.2x10^{-4}$ mm^3 and 317μemu, respectively. In other words, when designing the biolabeling system based on current one-port VNA-FMR method, Co NW should be larger than the $2.2x10^{-4}$ mm^3. For Ni and Fe NWs, the magnetization should be designed to be greater than 317 μemu.

3.4.2 Phase analysis method (PAM)

Using the VNA-FMR method, both magnitude and phase data can be collected from the MNWs. So far, FMR frequencies and signal strength have been obtained by the magnitude of the S-parameters. When FMR linewidths overlap, however, accurate parameter extraction is difficult to achieve. Thus, a phase analysis method (PAM) [44] is proposed using the phase of the S parameters and will be discussed.

PAM method obtains the FMR frequencies from the phase of S21 or S11, which can be defined as S21_phase or S11_phase. The first step is to take the phase derivative using equation 3.4.

$$\text{Phase derivative} = \frac{\partial S_{21\_phase}}{\partial DC\_field} \quad \text{or} \quad \frac{\partial S_{11\_phase}}{\partial DC\_field} \tag{3.4}$$

Then, FMR frequencies can be obtained from the extrema of the phase derivative. To fully understand PAM method, this method will be compared with magnitude method and be used to study the position and volume effect.

3.4.2.1 PAM and magnitude method comparison

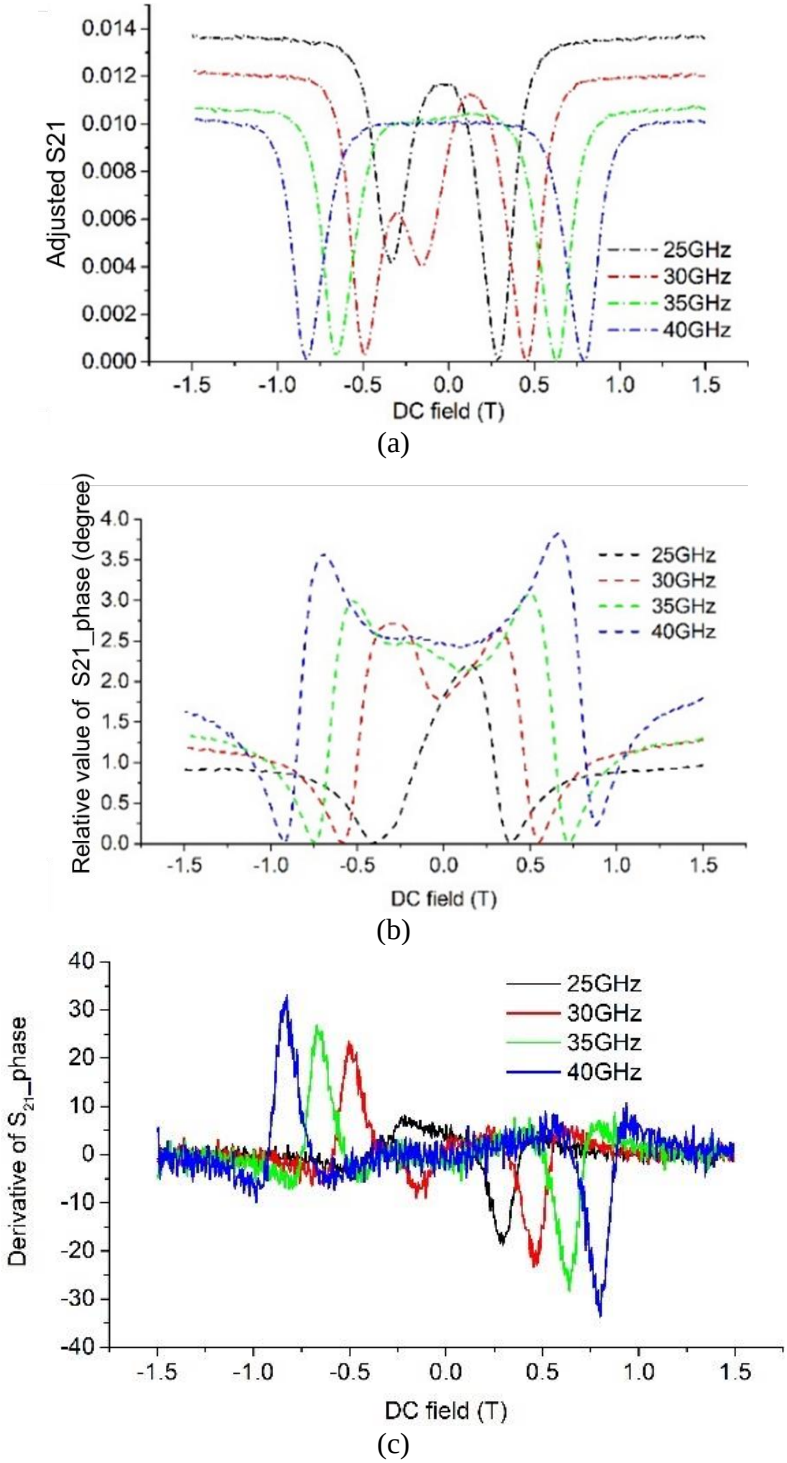

Fig 3.18. Family curves for Co72 in OP: (a) Relative value of $|S_{21}|$; (b) Relative value of S_{21}_phase in degrees; (c) Derivative of S_{21}_phase.

In Fig 3.18, the PAM and magnitude methods are compared. Co72 is measured on two-port measurement circuit in OP direction at 25 GHz, 30 GHz, 35 GHz and 40 GHz. The family curves for magnitude, phase and phase derivative of S21 in DC field domain indicate the relationship of FMR response versus DC field. A family curve of each parameter is shown in Fig 3.18. As DC field increases, the FMR frequencies also increase. For ease of comparison, the phase data is relative value which can be defined as the subtraction between the original value and minima.

From the minima of adjusted S21 and extrema values of the phase derivatives, FMR frequencies can be obtained with the same values. The DC fields corresponding to FMR frequencies are 0.29 T (25 GHz), 0.455 T (30 GHz), 0.63 T (35 GHz) and 0.785 T (40 GHz). Furthermore, the sign of the phase derivative indicates the moment directions for OP orientation corresponding to negative and positive DC field.

Fig 3.19 shows the magnitude and phase derivative data for Co72 in IP at 25GHz. Resonances located at low DC field are difficult to determine from the S21 magnitude and magnitude method because their linewidths are overlapped. By observing the phase derivative of the S21 data in Fig 3.18b, resonances are shown clearly. Thus, compared to the magnitude method, PAM is advantageous in showing the moment direction and distinguishing resonances when linewidth overlaps.

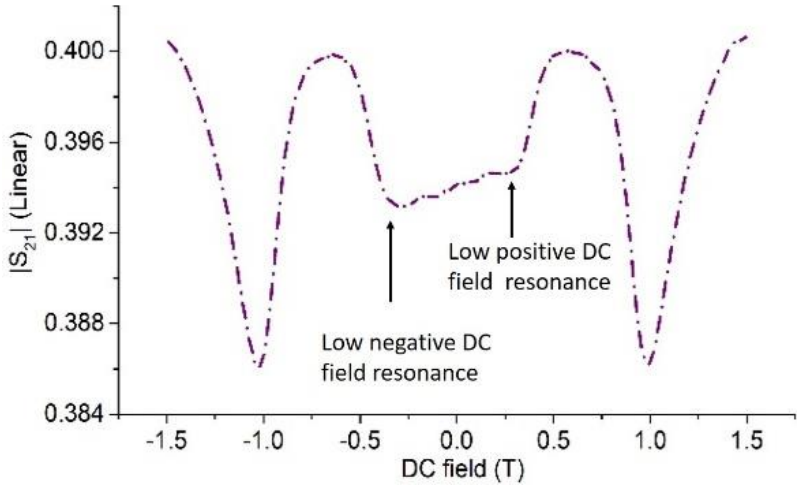

(a)

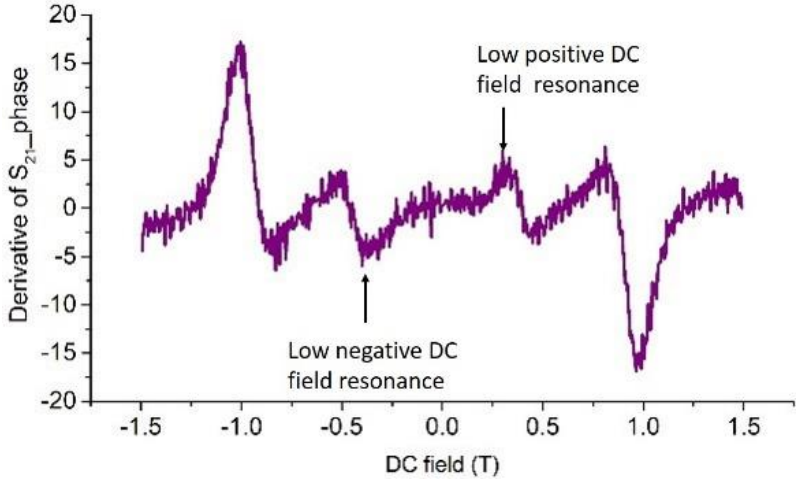

(b)

Fig 3.19. FMR for Co72 in IP at 25GHz: (a) $|S_{21}|$; (b) derivative of S_{21}_phase.

3.4.2.2 Position effect study

Phase is sensitive to sample placement. A diced Co80 chip with length of 3.698 mm and width of 0.423 mm is measured with different placements in OP at 40GHz; one is across the signal line and the other is above one slot. The phase and phase derivative of these two placement cases are shown in Fig 3.20. The S21 phase strength differs due to the placement orientations. For Co80 across the signal line, the phase variation is 0.74° compared to the slot placement, where the phase variation is 3.49°. Regardless of placement, however, consistent FMR frequencies are obtained at DC field of 0.905T as shown in Fig 3.20b.

Therefore, PAM method can be applied for MNW to obtain consistent FMR frequencies regardless of the different sample placement.

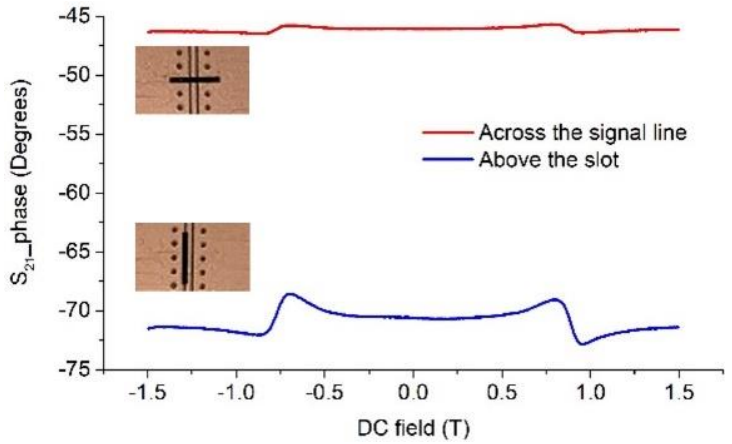

(a)

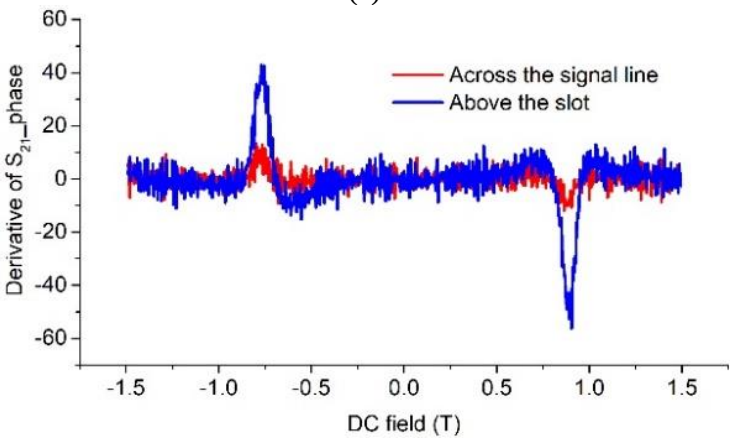

(b)

Fig 3.20. FMR results for Co80 in OP at 40GHz for sample across the signal line and above the slot: (a)S_{21}_phase in degrees; (b) derivative of S_{21}_phase.

3.4.2.3 Volume effect study

Due to the requirements for small size and volume of material detection for biomedical application, volume effect study of PAM method is needed to understand and to improve signal sensitivity. In this study, the one-port test circuit is used since it possesses higher signal sensitivity and signal strength compared to the two-port circuit.

The PAM approach is applied to two Co114 chips (Co114-large and Co114-medium) with similar chip widths of 1.875 mm. The respective chip lengths 3 mm and 0.481 mm are used to study the volume effect. The volume of large and medium Co114 chips are $3x10^{-3}$ mm^3, $4.8x10^{-4}$ mm^3, respectively. Fig. 3.21a shows the relative phases of S11 for large and medium chip in OP at 30 GHz. They have similar shape but different values due to length variation. Fig 3.21b shows the phase derivatives after smoothing the S11 phase data, which is necessary to reduce the high background noise in the raw data. From phase derivative results, approximate 0.06 T difference is observed between large and medium at FMR frequency. This difference might be due to the error introduced by the smoothing function.

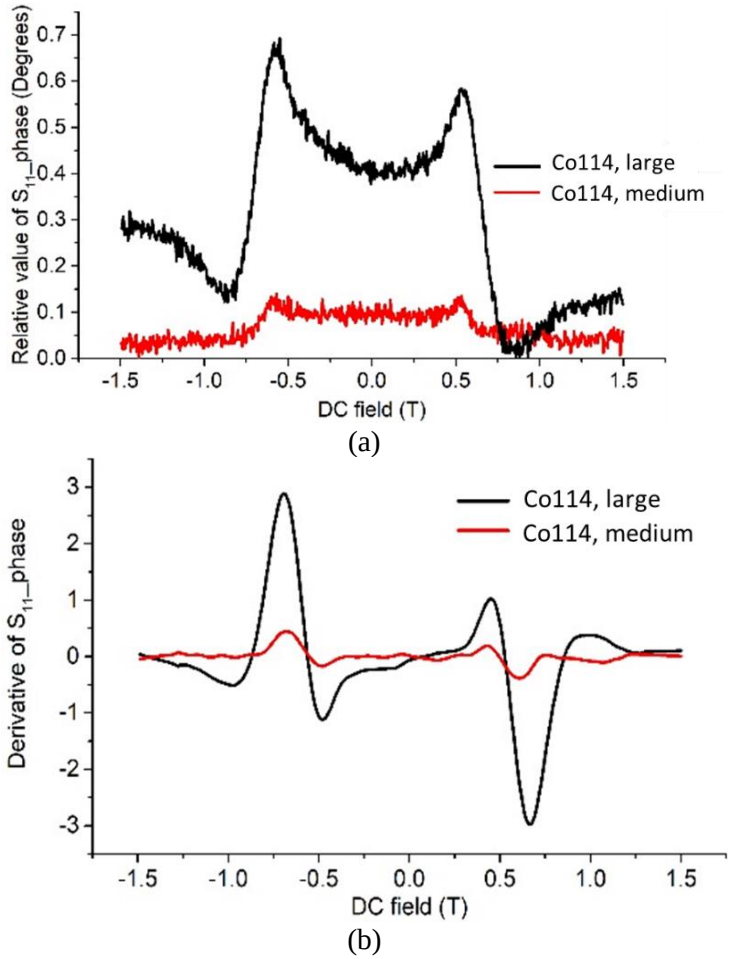

Fig 3.21. FMR results for Co114-A and Co114-B in OP at 40GHz: (a) Relative value of S_{11}_phase; (b) derivative of S_{11}_phase.

3.5 Tri-labeling system detection and identification

In the biolabeling applications, the ability to detect and identify multiple MNWs simultaneously is needed. In this section, the design of tri-labeling system will first be presented. Then the magnitude and PAM methods will be used to analyze a tri-labeling system.

3.5.1 Design of tri-labeling system model

By the endocytosis process, different types of MNWs, such as Fe, Ni and Co, can be taken into the cells, shown in Fig 3.22. The FMR frequencies of these MNWs therefore can be used to identify three different types of cells. To confirm this concept, these MNWs need to be detected and identified outside the cell first. Therefore, a tri-labeling system concept is proposed.

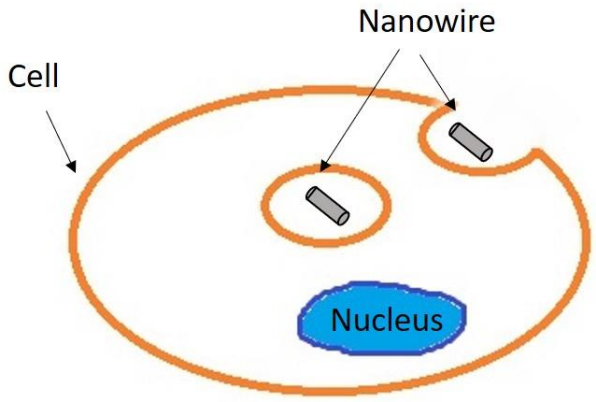

Fig 3.22. NWs inside cell through endocytosis process.

All MNWs are grown in 50 μm thick AAO. The proposed measurement configuration is shown in Fig 3.23. Three MNW samples are stacked on the CPW line. The stack order is based on ensuring the weakest to the strongest saturation magnetization order is achieved. The order from bottom to top is Ni, Co and Fe with corresponding saturation

magnetization of 485 emu/cc, 1440 emu/cc and 1707 emu/cc, respectively. This order allows all three samples to be detected and identified simultaneously.

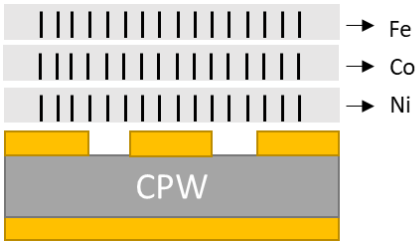

Fig 3.23 Tri-labeling system measurement configuration.

3.5.2 FMR tri-labeling model identification using magnitude method

Ni62, Co72 and Fe49 with NW length of 18 um, 15.5 um and 10.5 um, respectively, are used for tri-labeling model. Based on two-port measurement circuit, three MNW samples are measured in OP direction at 40 GHz individually and stacked as shown in Fig 3.23 simultaneously. The FMR frequencies are obtained using magnitude method in DC field domain, shown in Fig 3.24.

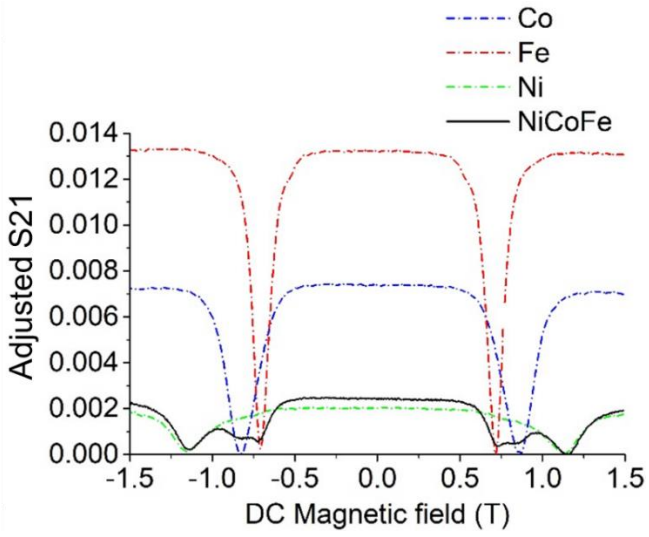

Fig 3.24. Tri-labeling system measurement using magnitude method.

From Fig 3.24, it can be shown that, FMR of Ni, Co and Fe can be detected individually and identified when measured together. The DC field for Ni, Co and Fe are 1.155 T, 0.785 T and 0.725 T. Compared to Ni, FMR frequencies of Co and Fe NW samples occur at lower DC field values due to higher saturation magnetization. Based on magnitude method, Ni, Co and Fe MNWs shows great potential for tri-labelling system.

3.5.3 Moment direction indication for tri-labeling model using PAM

Furthermore, PAM is studied for tri-labelling system using Ni, Co, and Fe MNWs. The same samples and measurement configuration is used for PAM based on two-port circuit. In Fig 3.25, the FMR for three samples measured in OP direction at 40 GHz is shown.

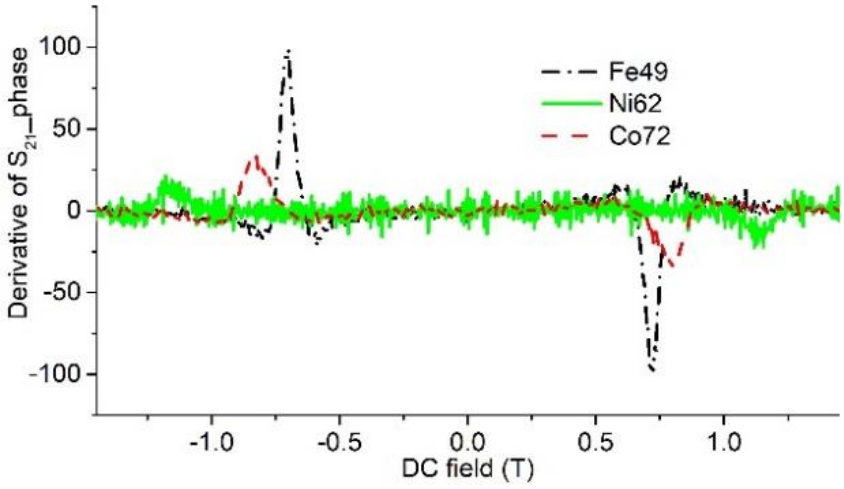

Fig 3.25. Tri-labeling system measurement using PAM.

The DC fields corresponding to FMR frequencies of Ni, Co and Fe MNWs obtained from PAM are similar to the magnitude method, 1.155 T, 0.785 T and 0.725 T. The data of Ni sample is nosier compared to Co and Fe due to lower magnetization of Ni. Compared to magnitude method, the PAM also shows different moment direction for positive and negative DC field regions.

3.6 MNWs assessment in bio-mimicking environments and bio-sample.

Measuring MNWs in a bio-environment will encounter three primary challenges, compared to measuring them in AAO template. First, MNWs will be randomly distributed, which means their porosity can be various in different region of sample. Second, MNWs will be randomly oriented. Third, small volume of magnetic material will be used which therefore generates small FMR signal strength.

In this section, the ability of detecting and identifying MNWs in a bio-mimicking environment and bio-sample will be evaluated.

The detection of FMR can be achieved by acquiring the difference between CPW circuit with and without MNW sample. In Fig 3.26, the difference between adjusted S21 data of Co NW and empty circuit is computed. A curve, shown in blue, with a nonzero difference value indicates NW presence on the circuit board. The value of difference indicates the magnitude of FMR absorption.

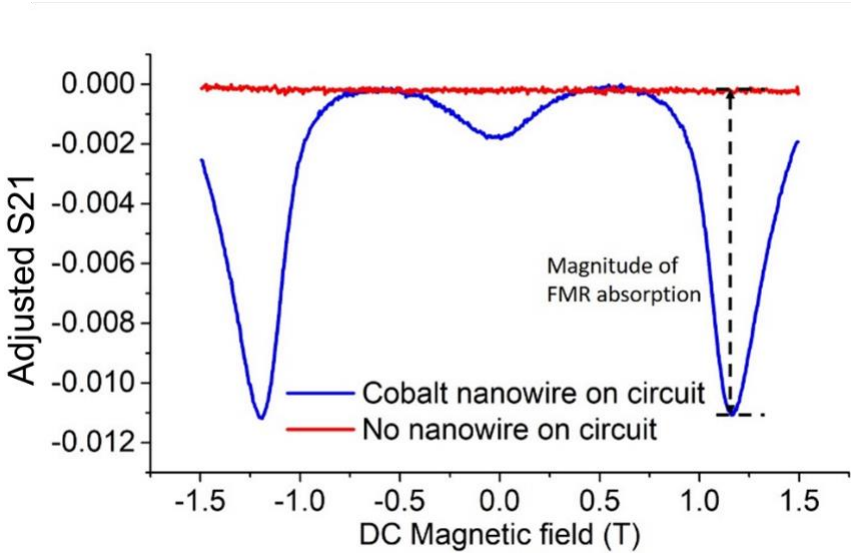

Fig 3.26. Comparison of Co NWs on circuit and no NW on circuit in IP direction at 30 GHz.

3.6.1 MNWs with random distribution and low FMR signal in polycarbonate substrate

The NWs inside cells are expected to be randomly distributed and oriented. However, the AAO templates used so far possess ordered pores in a rhombus shape. To study the NW in a bio-mimicking environment, with same orientation but random distribution, polycarbonate is used in this section. Different from AAO, the pores in polycarbonate are created by track-etch method where pores are created by high energy ion bombardment, which produces random distribution.

Herein, a Ni MNW sample fabricated on polycarbonate with diameter of 100 nm, wire length of 3 μm and porosity of 2.4% is used. The short NW length, low porosity and low saturation magnetization of Ni provide small FMR signal level.

The data are measured based on one-port circuit in IP orientation at 30 GHz and is shown in Fig. 3.27. The FMR absorption indicate the ability to detect the randomly distributed Ni NWs by FMR technique.

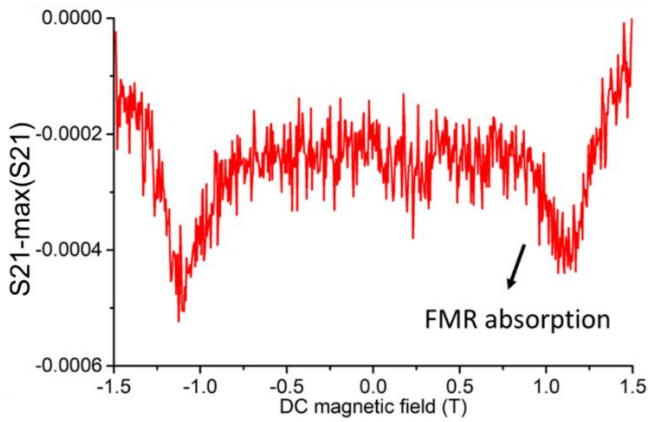

Fig 3.27. Ni NW grown in polycarbonate measured in IP orientation at 30GHz.

The FMR frequencies are compared to the Kittel equation predication for OP and IP orientation shown in Fig 3.28. The alignment between Kittel equation and measurement indicates the identification for Ni MNWs in polycarbonate.

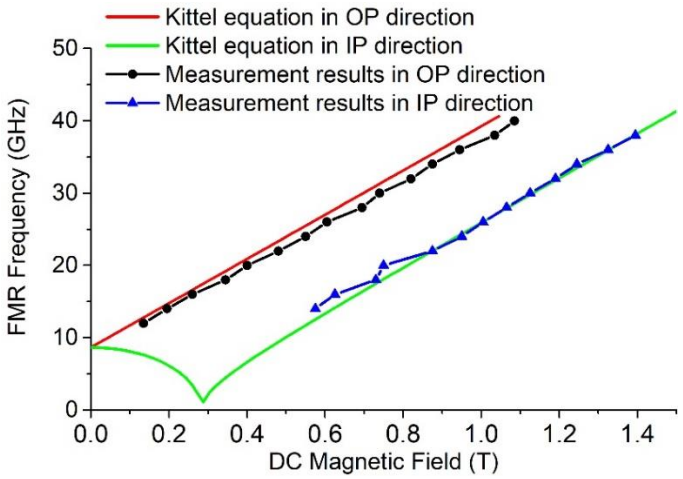

Fig 3.28. Comparison of measurement and Kittel equation for Ni NW grown in polycarbonate.

3.6.2 MNWs with random orientation and distribution in fixed cells

A bio-sample made with osteosarcoma cell and Fe-Au NWs is studied in this section. The cells are fixed with Epon 812 resin. The measurement used one-port measurement circuit to gain the benefit of highest sensitivity. The measured results in IP direction at 36 GHz is shown in Fig. 3.29. The comparison of measurement and Kittel equation predication for ordered FeAu NWs is shown in Fig. 3.30. From Fig. 3.29, the FeAu NWs inside bio-samples are detectable. The FMR response of bio-sample in IP and OP directions, shown in Fig. 3.30, are aligned together, which indicates the randomly-orientation of FeAu NWs inside cells. They are not aligned to the Kittel equation, which indicates that FeAu NWs can be detected but cannot be identified. To identify the MNWs

inside cells, the NWs need to be oriented to the same direction, which requires an external DC field and the bio-sample with MNWs in the liquid environment.

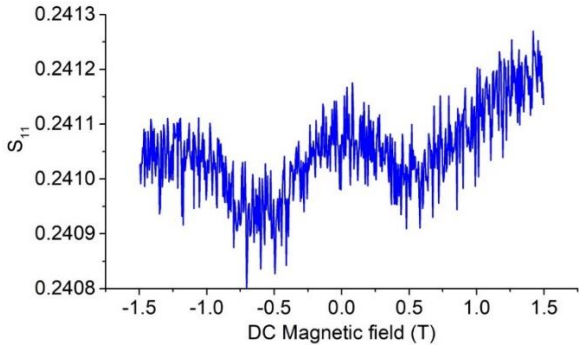

Fig 3.29. The FMR measurement of bio-sample in IP direction at 36GHz.

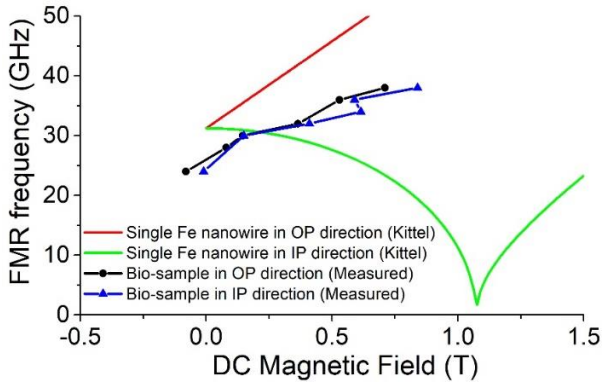

Fig 3.30. Comparison of measurement and Kittel equation for bio-sample.

3.7 Summary

In Chapter 3, the characterization of FMR response for MNWs is studied for biolabeling applications. The VNA-FMR method is implemented with CPW test circuits, which provide both magnitude and phase of S parameter to obtain the FMR response. Two methods are proposed, magnitude method and PAM method.

Based on magnitude method, FMR frequencies of Co MNWs are studied and compared to the Kittel equation and simulation results. The experimental data and simulation show good agreement. The variables that influence FMR response are studied,

such as Cu back effect and position effect. From the study, including a Cu back layer on the sample, placing the sample on the slot and making the external AC field perpendicular to the magnetization each enhance the FMR signal.

To quantify the system ability to detect small signal. Small signal analysis is performed by determining the most sensitive system among one-port and two-port approach and smallest detectable material volume. From the experimental, one-port short-circuited CPW shows higher signal strength compared to two-port thru line CPW due to less signal transmission path and therefore less loss. The smallest detectable Co volume and magnetization are 2.2×10^{-4} mm^3 and 317 μemu, respectively, using the one-port circuit.

For PAM method, the derivative value of S parameter phase is taken, which provide the information of FMR frequencies. Compared to the magnitude method, PAM shows advantages in determining the FMR for overlapping linewidths and direction of magnetic moments. This feature will make FMR signals easier to distinguish when PAM is applied to biosensing applications.

In addition, position effect of PAM method is studied. The results show that FMR frequency is not sensitive to the placement differences. Also, two small size and small volume samples with same width but different lengths are characterized accurately using one-port CPW circuit. The DC field values at the FMR frequency for Co114-large differ from Co114-medium by 0.06 T, which might be due to the error introduced by the smoothing function.

The tri-labeling system is proposed for use with magnitude and PAM methods. Ni, Co and Fe MNWs are measured individually and simultaneously. The FMR frequencies for

three different material can be detected and distinguished, which shows great potential for tri-label biosensor applications.

Finally, the MNWs are characterized in a bio-mimicking environment and biological sample. For bio-mimicking environment, the MNWs are grown in polycarbonate, which are randomly distributed but aligned in the same directions. The detection and identification can be achieved in this case. For MNW in biological sample, NWs are randomly distributed and oriented in osteosarcoma cell. The detection can be achieved but identification cannot be realized. The next step will be putting MNWs and cells in a liquid format and using external DC field to align NWs in the same orientation.

Chapter 4 MNW characterization for communication applications

4.1 Introduction

Magnetic nanowires (MNWs) are attracting broad interest for microwave device design in transmitting and receiving modules for wireless communication technology [45-47]. Their long thin shape provides high shape anisotropy along the wire axis, which creates large remnant state. This feature allows MNWs to possess gigahertz frequency range ferromagnetic resonance (FMR) absorption at zero DC field and to eliminate a need for an external magnet when applied in nonreciprocal microwave devices. Therefore, MNW-based microwave devices are desirable for future wireless communication. Also, MNWs grown in an anodized aluminum oxide (AAO) template provide high stability, compared to thin film, due to less exposure to the air. Examples of recent designs based on MNWs include circulators [48], band-stop filters [49], and isolators [50].

To use MNWs as a magnetic substrate for non-reciprocal device design, characterization is needed to obtain the material parameters. Three key design parameters play dominant role in the device design process. They are FMR, permeability tensor and linewidth.

In this chapter, the discussion about key design parameters will be presented first. Then an experimental method to characterize MNWs will be shown.

4.2 Key parameters for use of MNWs in AAO template for non-reciprocal device design

A non-reciprocal device, such as circulator, provides transmission in the one direction and isolation on the opposite direction, shown in Fig 4.1. For example, if signal needs to transmit from port 1 to port 3, then the ideal transmitted voltage ratio from port 1 to port 3 (S31) should approach to 1 and that from port 3 to port 1 (S13) should approach to 0.

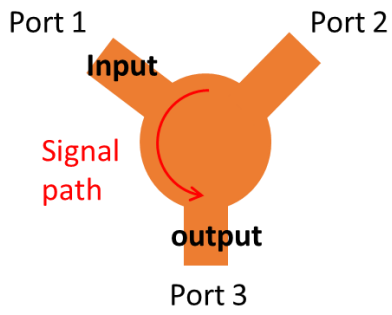

Fig 4.1. A schematic of a circulator.

A conventional circulator usually requires a magnetic material to provide high non-reciprocity, which is a parameter defined as the power difference of transmitted signal between forward and backward direction.

To use MNWs grown in AAO template as a magnetic substrate for non-reciprocal device design, several parameters are important to understand. They are FMR frequencies, permeability tensor and linewidth.

4.2.1 FMR frequency

FMR frequencies stems from the magnetic material, in which countless spinning electrons resonant at an AC frequency with specific DC field. In Fig 4.2, a spinning electron within magnetic material is shown. The DC fields are perpendicular to the AC fields. The frequency that electron resonant at is called FMR frequency.

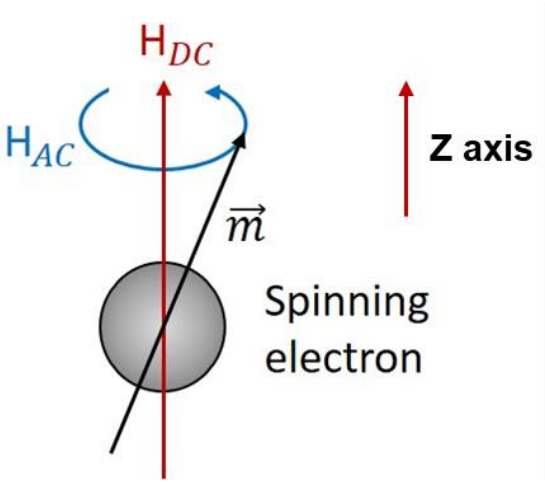

Fig 4.2. Spinning electron inside magnetic material. H_{DC} is internal DC field and H_{AC} is internal AC field.

FMR frequency is an important parameter for non-reciprocal device design. The high non-reciprocity occurs around FMR. Therefore, a well-performed non-reciprocal device needs to be designed close to an FMR. However, at FMR resonance point, the material loss is extremely high and theoretically close to an infinite value, which is undesirable. So, the FMR of MNW substrate needs to be characterized accurately before head. Based on the FMR frequency, the operation frequency would be designed to be close to FMR frequency but not at exact resonance point.

4.2.2 Permeability

Permeability is the second important parameters, which is related to FMR frequency. The relative permeability for a magnetic material is greater than 1 around FMR frequency.

A typical permeability around FMR is shown in Fig 4.3. The real part of permeability, μ', will first increase to a positive maximal and decrease to a negative maximal. The non-reciprocity is proportional to the μ'. The larger the μ' is, the larger the non-reciprocal effect will be. The imaginary part of permeability, μ'', is related to the transmission loss. A μ'' has a peak at FMR resonance. The larger the $\mu''$is, the higher signal loss would be for forward signal transmission direction.

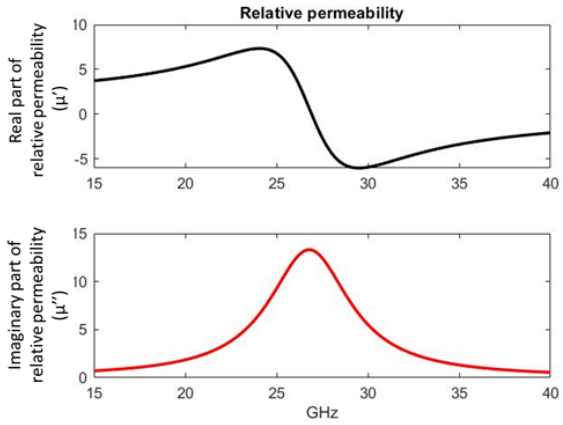

Fig 4.3. Relative permeability at FMR frequency band.

This also explains why a non-reciprocal device designer would have operating frequency close to the FMR but not at the exact resonance point.

4.2.3 FMR Linewidth

The last key parameter is FMR linewidth, which is defined as the full width maximal of permeability. The FMR linewidth indicates the material loss. As a magnetic

substrate, MNWs should possess the lowest signal transmission loss in forward direction as possible. Therefore, the linewidth of fabricated MNW substrate should also be as low as possible.

From [51], the linewidth in frequency domain, $\Delta\omega_0$, can be expressed in the equation 4.1

$$\Delta\omega_0 = 2\alpha\omega = \Delta H\mu_0\gamma \qquad (4.1)$$

where α is damping constant, ω is the operate frequency, and ΔH is the linewidth in DC field domain. From equation 4.1, linewidth increases as frequency increases. Furthermore, other variables show influence on FMR linewidth like NW length [9] and need to be further confirmed by more experimental study.

To design microwave devices in a full wave modeling tool, these three parameters of MNW are needed and are not readily available in commercial software like Ansys HFSS (High Frequency Structural Simulator). Therefore, an experimental method to characterize the FMR properties of MNWs and extract their relative permeability and linewidth in the frequency domain is needed and required to accurately model circuits using this type of material. The FMR and permeability extraction measurement will be shown next.

4.3 FMR and Permeability extraction

Herein, using VNA-FMR method [38], the FMR response and permeability can be obtained based on one-port coplanar waveguide (CPW) line. The FMR data are obtained in the frequency domain for the ease of designing the device using electromagnetic software.

An Anritsu 37369D VNA is used and provides an AC field that is swept in the range of 0.04 GHz to 40 GHz. It detects FMR response by reflection coefficient (S11). The CPW circuit with MNW sample is put between two poles from electromagnet that provides a constant DC magnetic field in the range of 0 to 0.55 T. The measurement system set-up is the same as that was shown in Fig 3.3.

Compared to the FMR measurement method in DC field domain, described and discussed in Chapter 3, FMR characterization in frequency domain is more challenging due to RF background noise. To overcome this issue, different volume sizes of MNW sample (small and large), are used to extract permeability. Also, to enhance the FMR signal strength, the Cu back effect is used.

4.3.1 Extraction using small volume sample

A diced cobalt MNW sample, Co72-small, with length of 1.958 mm and width of 0.331 mm is used in this section. No Cu back layer is included. The sample is put on the CPW and S11 data, which indicates the FMR response, is obtained. In Fig. 4.4, S11 data of an AAO sample and a Co72-small sample on a short-circuited CPW for DC fields at 0.4T and 0.5T are shown, respectively. The additional reduction in S11 with the Co72-small sample compared to the empty AAO suggest that FMR is present. However, it is not adequate to determine the specific FMR frequency due to the presence of additional board resonances. Thus, the known “four steps” method [52-54] is needed and applied here in order to determine the FMR frequency and extract the permeability of the Co72-small sample.

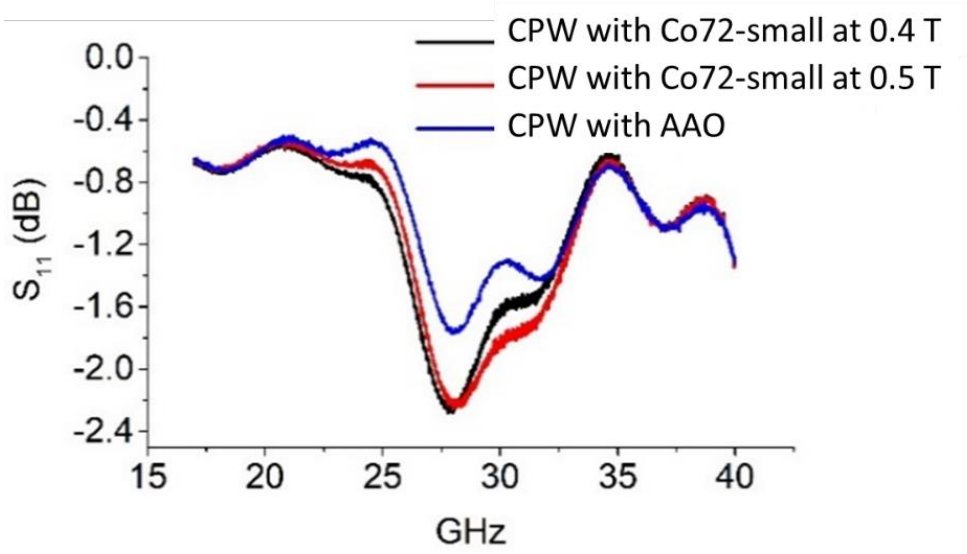

Fig 4.4. The S_{11} measurement of the CPW board with Co72-small sample at 0.4T, 0.5T and CPW board with same size AAO in OP direction.

Using the "four steps" method [53], first, a calibration is performed to remove cable and connector effects. The one-port VNA calibration shifts the reference plane to the input of the test circuit connector. Then, the S_{11} value of two short-circuited CPW test boards (i.e., lengths of 7.8mm and 5.8mm) is measured to remove the connector effects. The side view cross section of NW sample on a one-port CPW is shown in Fig 4.5. The reflection coefficient (Γ) of the circuit is expressed as equation 4.2

$$\Gamma = \Gamma_0 e^{-2(\gamma_{empty} l_{empty} + \gamma_{sample} l_{sample})} \qquad (4.2)$$

where Γ_0 is the reflection constant at the end of the transmission line with the value of -1, $\gamma_{empty}$is propagation constant in the empty CPW, l_{empty} is the line length of empty CPW, γ_{sample} is propagation constant for the CPW with MNW sample and l_{sample} is the length of MNW sample. Since the propagation constant can be expressed as $\gamma = \frac{i\omega\sqrt{\mu_{eff}\epsilon_{eff}}}{c_0}$, the effective permeability μ_{eff} can be extracted from γ based on Γ. The extraction process will be discussed in the next few steps.

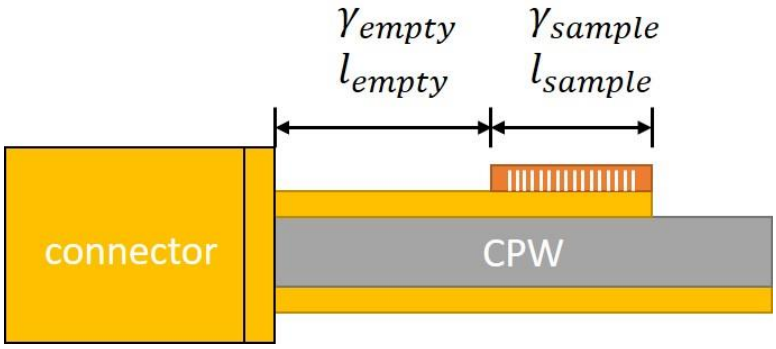

Fig 4.5. Cross section of NW sample above one-port CPW circuit. γ_{empty} is propagation constant in the empty CPW, l_{empty} is the line length of empty CPW, γ_{sample} is propagation constant for the CPW with MNW sample and l_{sample} is the length of MNW sample.

In second step, the S11 of empty test board, S_{11}^{empty}, is measured to obtain the effective permittivity of short-circuited CPW test board, defined as ϵ_{eff}^{empty}, using equation 4.3.

$$\epsilon_{eff}^{empty} = \left(\frac{ic_0 \ln\left(-S_{11}^{empty}\right)}{2\omega(l_{sample}+l_{empty})}\right)^2 \qquad (4.3)$$

Third, the CPW test board was measured with AAO template to obtain effective permittivity of board with AAO, ϵ_{eff}^{AAO}, using equation 4.4. In equation 4.4, S_{11}^{AAO} is the S11 data of CPW test board with AAO.

$$\epsilon_{eff}^{AAO} = \left(\frac{ic_0 \ln\left(-S_{11}^{AAO}\right)}{2\omega l_{sample}} - \frac{\sqrt{\epsilon_{eff}^{empty}}\, l_{empty}}{l_{sample}}\right)^2 \qquad (4.4)$$

And finally, the S11 data of test board with NW array sample, S_{11}^{sample}, is measured to obtain the effective permeability of the test board with NW sample. The last measurement is used to extract the effective permeability of the NWs based on the effective permittivity value from the previous steps. The equation 4.5 is used to extract the effective permeability, μ_{eff}.

$$\mu_{eff} = \left(\frac{ic_0 \ln\left(-S_{11}^{sample}\right)}{2\omega l_{sample}\sqrt{\epsilon_{eff}^{AAO}}} - \frac{\sqrt{\epsilon_{eff}^{empty}}\, l_{empty}}{\sqrt{\epsilon_{eff}^{AAO}}\, l_{sample}}\right)^2 \quad (4.5)$$

Then equation 4.6,

$$\mu'_{initial} = \frac{Ms}{Ha} + 1 \quad (4.6)$$

is used for calibrating the initial real part of relative permeability in low frequency range using M_s of 1440 emu/cc and H_a, extracted from hysteresis loop with the value of 4446 Oe (Fig 4.6). Finally, relative permeability, μ, is obtained with the value of calibrated μ_{eff}.

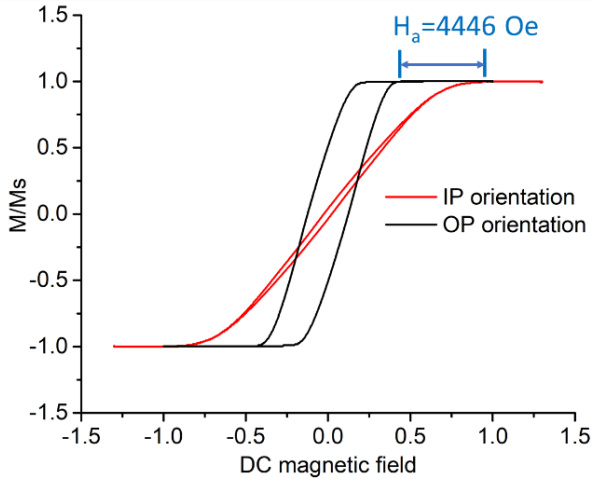

Fig 4.6. Hysteresis loop of Co72 in IP and OP orientation. Anisotropy field, H_a, is defined by the difference of DC saturation field in IP and OP orientation.

In the third and fourth steps, the AAO and MNWs sample were put above the left slot of the CPW board in OP direction of DC field to reach the maximum AC field region as seen in Fig 4.7. The study in chapter 3.4.1.2.2 shows that FMR absorption comes from the orthogonality of AC field and magnetization. The sample width ,0.331 mm, is slightly wider than the gap and it is believed that the sample edges above the signal line absorb the

AC field energy due to the orthogonal relationship between magnetization and AC field on the signal line.

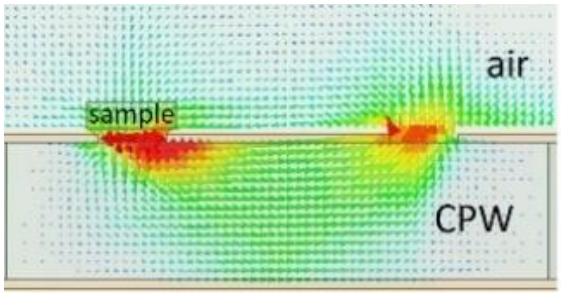

Fig 4.7. HFSS simulation for AC magnetic field distribution of CPW board at cross section. Red and green arrows represent the AC magnetic field strength of 270A/m and 109A/m, respectively.

The relative permeability, $\mu = \mu' - j\mu''$, of Co72-small at 0.4T in OP orientation is shown in Fig 4.8. The FMR frequency for Co72-small is 27GHz based on the peak of μ'', which is not obvious from S11 Fig 4.4. Fig 4.8 shows that the real part of relative permeability is 7 and the imaginary part is 4.5 at FMR frequency. From the full width at half maximum of μ'', the linewidth of Co72-small is 5.18 GHz.

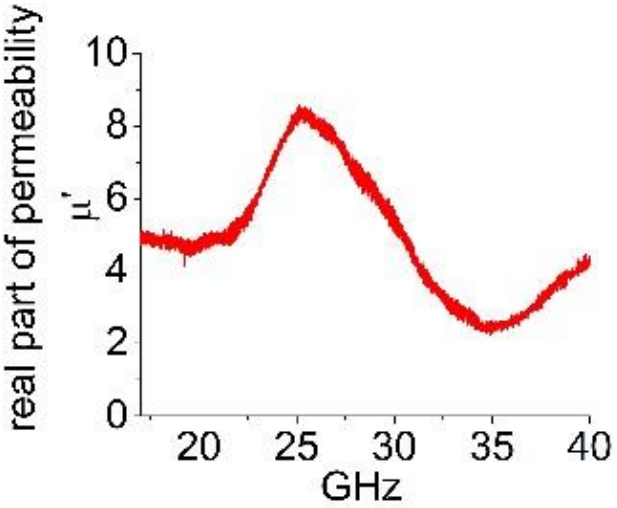

(a)

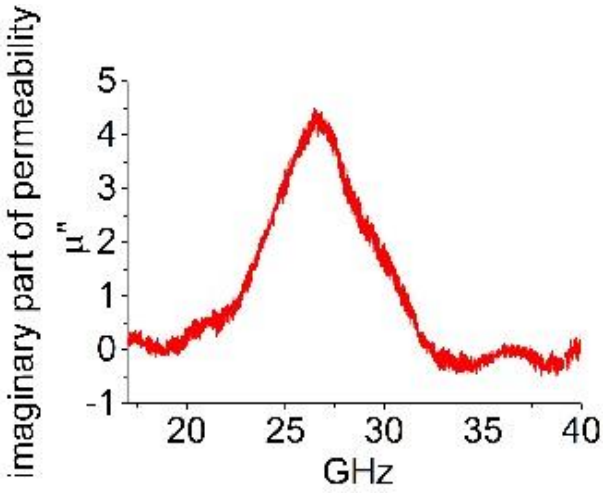

(b)

Fig 4.8. (a) The real part of permeability μ' for nanowire array at 0.4T in OP direction, (b) The imaginary part $\mu''$of permeability for NW array at 0.4T in OP direction. The FMR frequency for Co72-small at 0.4 T is 27GHz.

At the other DC fields like 0.5 T, the permeability data for Co72-small cannot be obtained due to high RF background noise environment. So, a large volume sample will be used in the next section.

4.3.2 Extraction using large volume sample

Extracting the FMR frequencies and permeability based on small volume sample, discussed in chapter 4.2.1, is difficult due to small FMR signal level and large RF background noise. To resolve the issue, several large volume samples, which can cover the cross section of CPW line, are used [55].

4.3.2.1 MNW sample without Cu back layer

A diced Co72-large sample with length of 3 mm and width of 2 mm is used. No Cu back layer is included. The S11 response of empty AAO and Co72-large without Cu layer on CPW circuit in OP orientation is shown in Fig 4.9. The AAO template without NWs is used to provide reference. Co72-large MNWs grown inside AAO are measured at different

DC fields. Board resonances and FMR responses are identified. A board resonance for AAO above CPW is observed around 27.2 GHz. The FMR resonances of Co72-large can be observed at 0.45 T and 0.52 T when they are located away from the board resonances. Below 0.4 T, FMR resonances overlap with board resonances and are hard to determine. Compared to the FMR response of Co72-small shown in Fig 4.4, the FMR frequencies of Co72-large can be observed at frequency bands that are away from board resonances.

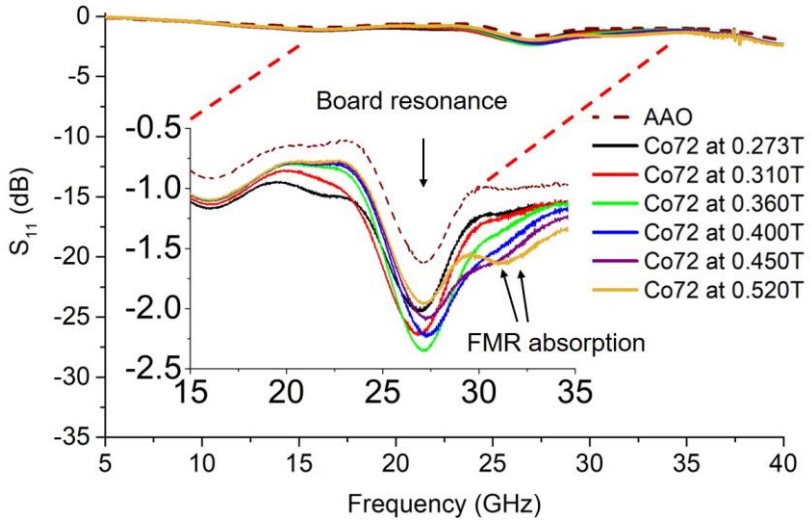

Fig 4.9. Reflection response (S11) versus frequency for MNW sample and empty AAO placed on top of the CPW circuit. The Co72-large without Cu and AAO samples are evaluated at different DC field values to identify board resonances and FMR absorption peaks. A detailed view of FMR response from 15 to 35 GHz is embedded.

Based on these S11 data, permeability of Co72-large is extracted using "four step methods". Considering CPW structure, permeability includes two components contributed by AC fields above signal line and slots. Herein, measurements are taken in OP orientation. Therefore, only AC fields above the signal line contribute to the extracted permeability since the AC signal and magnetization above slot are primarily parallel.

The extracted permeability of Co72-large without Cu layer is shown in Fig 4.10. The μ' for DC fields below 0.36T, shown in Fig 4.10a, is influenced by the board resonance and distorted from 25-29.5 GHz. The μ'' show less influence from the board resonance. The average linewidth is obtained by calculating the average of full width at half maximum of all μ'' curves. The calculated linewidth of Co72-large without the Cu layer is 5.6 GHz.

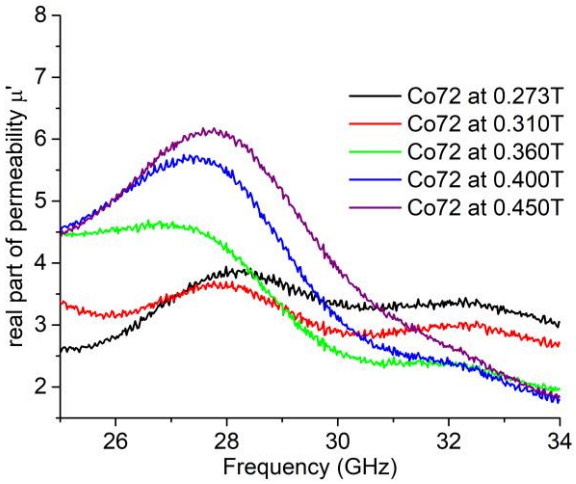

(a)

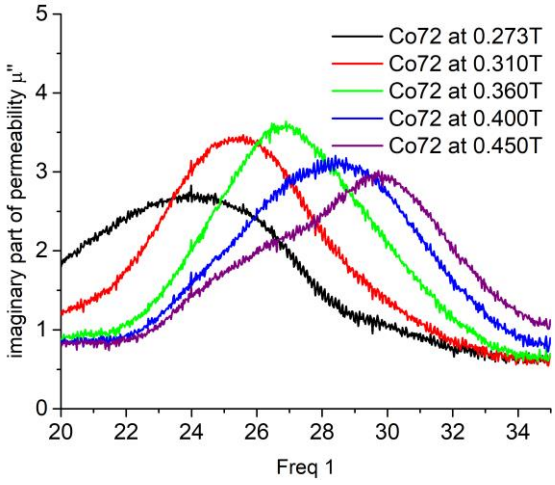

(b)

Fig 4.10. Permeability of Co72 without Cu layer. (a) The real part of permeability μ', (b) The imaginary part of permeability μ''.

Compared to the small volume sample, the large volume sample provide clear FMR frequencies in the bands that are away from the board resonances. The permeability can be extracted, which is, however, has the distortion from 25-29.5 GHz due to the board resonance. To resolve the issue that FMR frequency and extracted permeability can be influenced by board resonance, Cu back layer is used and will be presented next.

4.3.2.2 MNW sample with Cu back layer

To enhance the FMR signal, a Cu layer has been deposited on one side of the Co72-large sample. The presence of Cu layer attracts the magnetic fields from the slots of CPW to the region above the signal line as discussed earlier to enhance the FMR absorption (Fig 3.10).

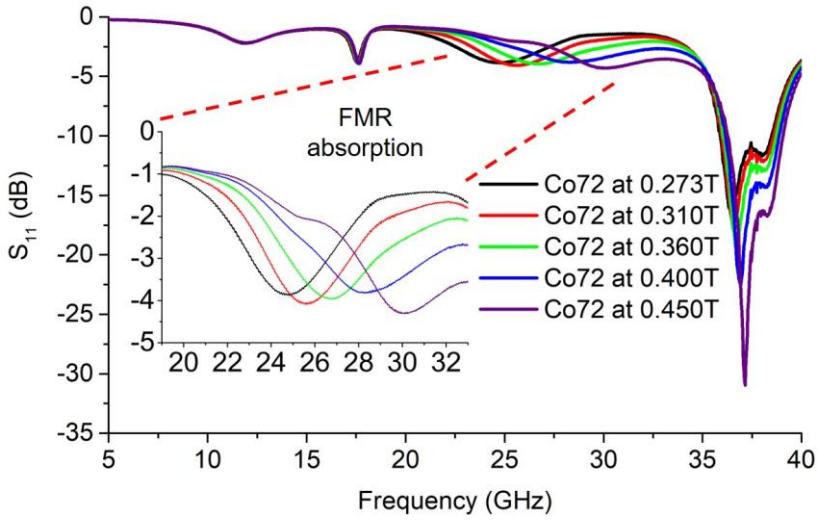

Fig 4.11. S11 response of Co72-large with Cu back layer at different DC fields. A detailed view of FMR response from 19 to 33 GHz is embedded.

In Fig 4.11, the FMR absorptions of Co72-large with Cu layer can be clearly observed at all five different DC fields. The FMR signal strengths are around -4 dB and is stronger compared to Co72-large without Cu layer, which are around -1.6 dB. When the

Cu back layer is included, however, three parasitic resonances are introduced at 12 GHz, 17.5GHz and near 37GHz. These resonances are related to the capacitance introduced between Cu layer and CPW circuit and inductance of MNWs.

Therefore, while the Cu layer offers signal enhancement benefits that result in higher FMR absorption and ease of detection, it can also introduce unwanted parasitic resonances in the frequency domain. However, in this work, these parasitic resonant frequencies do not interfere with the FMR frequencies of interest. The factors that control the frequency and signal strength of parasitic resonances are being investigated.

To confirm the accuracy of FMR frequency extraction in frequency domain, FMR frequencies of Co72-large with Cu layer is compared to the Kittel equation 2.2 and shown in Fig. 4.12. The FMR frequencies of Co72-large align well with the Kittel equation.

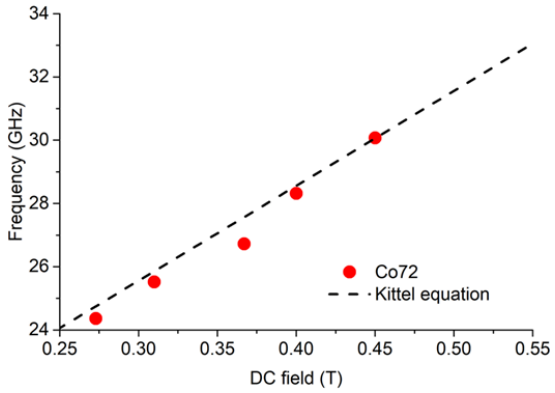

Fig 4.12. FMR Comparison between FMR frequencies of Co72-large extracted in frequency domain and the Kittel equation.

Based on Co72-large with Cu layer and using "four step methods", the permeability at different DC field is shown in Fig. 4.13. The real part of permeability (μ') in Fig 4.13a has less distortion from the board resonance, which is more accurate, compared to Co72-large without Cu layer (Fig 4.10a). This is due to stronger FMR absorption resulting from

the Cu back layer. The average linewidth of Co72-large with Cu layer is 4.96 GHz and is 11% smaller than the sample without the Cu layer. This shows the potential of Cu back layer to decrease the linewidth of the material which relates to the damping loss. The peak values of μ'' indicate the FMR frequencies which agree with the FMR frequencies in Fig 4.11.

To confirm that the Cu back layer enhancement method can be applied to the other material, Fe47 with NW length of 10.5 µm, NW diameter of 40 nm and porosity of 12% is investigated. The Fe47 MNW sample is diced with length of 3 mm and width of 2 mm. The anisotropy field of Fe47 is acquired by the hysteresis loop measurement with the value of 8270 Oe.

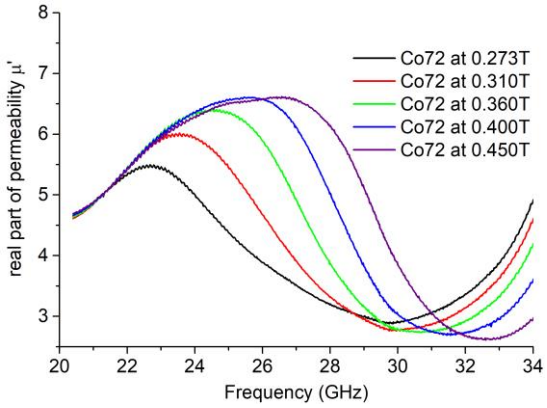

(a)

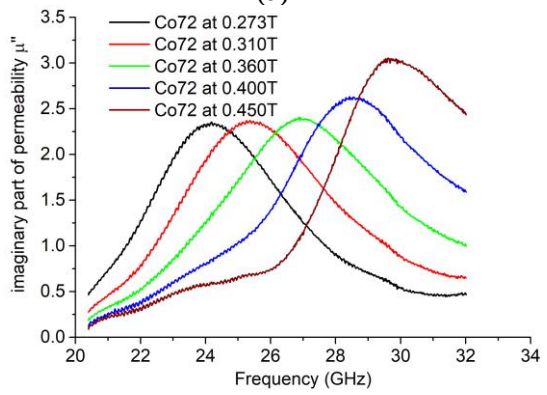

(b)

Fig 4.13. Permeability of Co72-large with Cu layer. (a) The real part of permeability μ', (b) The imaginary part of permeability μ''.

The extracted relative permeability of Fe47 with the Cu back layer is shown in Fig 4.14 Compared to Co MNWs, Fe MNWs possess higher FMR frequencies at low DC field due to higher saturation magnetization. For example, the FMR is 31.86 GHz for Fe47 at 0.42 T (Fig 4.14b) and is 30.07 GHz for Co72-large at 0.45 T (Fig 4.13b). This feature can be beneficial for microwave device design when external DC field is limited but higher operating frequency is required.

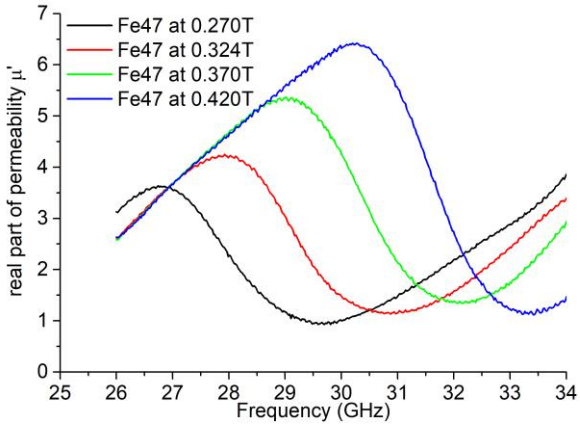

(a)

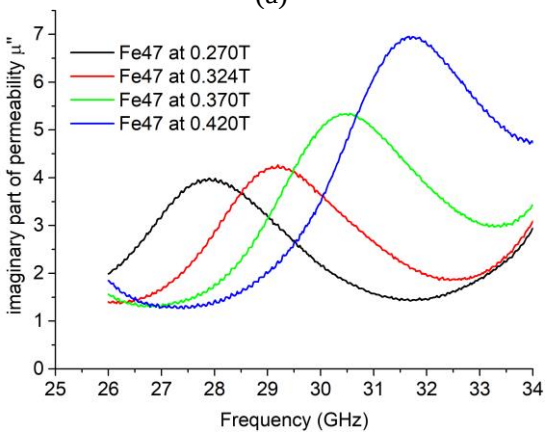

(b)

Fig 4.14. Permeability of Fe47 with Cu layer. (a) The real part of permeability μ', (b) The imaginary part of permeability μ''.

In general, using a large volume sample with Cu back layer, the FMR frequencies, relative permeability, and linewidth for different types of MNWs can be acquired successfully.

4.4 Summary

In this Chapter, a complete characterization method for FMR response and permeability extraction of MNWs are presented for communication device design.

Three key parameters for non-reciprocal device design have been discussed. They are FMR frequencies, permeability tensor and FMR linewidth. They are required to design a device using an electromagnetic software. FMR frequency provide information of the ideal operating frequency bands. The permeability indicates the non-reciprocity, and the FMR linewidth provide the information about material loss.

Compared to chapter 3, FMR study in chapter 4 is implemented in frequency domain, which is more challenge due to the RF background noise. Therefore, MNW samples with different volume of material are studied and Cu back layer effect is applied.

Based on Co72-small without Cu back layer, the FMR frequencies, permeability and linewidth can be obtained by “four step methods” at 0.4 T in frequency domain. The real part of relative permeability is 7 and the imaginary part is 4.5 at FMR frequency of 27 GHz. The linewidth is obtained with the value of 5.18 GHz. At other DC fields, the RF background noise cause the difficulty on the permeability extraction.

Then, by using Co72-large without Cu back layer, FMR frequency can be obtained in the frequency bands that are away from board resonances. However, the extracted

permeability possess distortion from 25 GHz to 29.5 GHz influenced by the board resonances.

To further resolve the issue, a Cu back layer is added to enhance the FMR absorption. Compared to the Co72-large without Cu back layer, the FMR absorption of sample with Cu layer possess twice higher signal magnitude, which provide ease of FMR detection and permeability extraction. The obtained FMR frequencies of Co72-large with Cu back layer aligns well with Kittel equation. Based on enhanced S11 data, the permeability of Co72-large with Cu layer is extracted and shows no distortion. The linewidth can be obtained from μ'' with the value of 4.96 GHz. To further confirm that the permeability extraction methods can be applied to other material, the Fe47 MNWs with Cu back layer are studied and the permeability is extracted successfully. Therefore, by using FMR characterization technique in this chapter, the three key parameters can be obtained from a MNW substrate.

In summary, to design a non-reciprocal device using MNW substrate, FMR frequencies, permeability and linewidth need to be obtained in the frequency domain first. A MNW sample with large volume material and Cu back layer needs to be used to obtain these parameters. A small value of linewidth is preferred, which indicate low material loss. Then, based on FMR frequencies, the device needs to be designed close to the FMR resonance to gain the benefit of high non-reciprocity, but not at exact resonance point to avoid high loss from material absorption. And lastly, the extracted permeability can be imported into a commercial software to accurately model the device design.

Chapter 5 Cu NWs on Si as vertical via for millimeter wave packaging and integration

5.1 Introduction

In IC circuits and systems, vias play a significant role in high-speed signal transmission. They provide high-density interconnections between active devices as well as are used in grounding, signal routing, and transitions from microstrip to coplanar waveguide (CPW). Vias have less metal interconnection paths and therefore lower parasitic resistance and inductance [56], compared to conventional interconnect technology such as wire bonds.

However, as the communication frequency band expands progressively into millimeter (30 -300 GHz) and even submillimeter wave frequencies (300 GHz - 300 THz), conductive loss due to higher skin depth effect and parasitic inductance in these vias becomes prohibitive. To resolve these issues, different substrate materials are used to reduce the high frequency loss, such as high resistivity silicon (Si) wafers [21]-[22], glass [57] and commercial anodized alumina oxide (AAO) [23]-[24]. Unfortunately, due to substrate thickness limitations, the thickness of vias used in these technologies falls within the range of 50-250 μm. This range does not satisfy the need of small package size for a 3D IC/Si integration process [58] in CMOS applications, such as the CMOS imager sensor [59]. The required via thickness is in the range of 1-30 μm. Thus, a technique for fabricating and characterizing ultra-thin vias that are required by 3D CMOS applications is lacking.

To address this via thickness issue, a novel integrated via structure in integrated AAO (iAAO) with copper (Cu) nanowires (NWs) on high resistivity Si wafer is

investigated. CPW lines on high resistivity Si are used to evaluate the via loss and to separate Si substrate loss from the via assessment. The test result shows that this integrated via structure provides a low power loss due to the benefit of both substrate material and NW properties. NWs are easily penetrated by high frequency fields due to their nano-meter size and therefore show less skin depth effect. By using bundles of NWs, total power loss can be decreased [23]. Also, by using iAAO, ultra-low via thickness can be provided and improved integration can be achieved.

In this chapter, integrated Cu NW vias are studied as vertical interconnects between CPW lines for millimeter wave band. The skin depth effect is discussed first. Then, the design and simulation results are going to be shown. Next, the transmission characteristics of these NW vias are measured up to 40 GHz, 67 GHz, and 110 GHz. The via dimensions and position effects are studied. Lastly, the performance of NW and conventional via are compared.

5.2 Skin depth effect

To apply Cu NWs as vertical vias in millimeter wave, the skin depth effect which contributes to the conductive loss needs to be understand. Fig 5.1 shows a cross section of a good conductor with skin depth effect. As frequency expands to the microwave bands, the current flows through the outer region of the conductor, between the dashed and solid circle (Fig 5.1), instead of the whole cross section area. This creates higher loss. The skin depth, defined as δ_s, is therefore used to describe how deep an electromagnetic wave can penetrate a conductor and is expressed in equation 5.1 [51].

$$\delta_s = \frac{1}{\sqrt{\pi f \mu \sigma}} \qquad (5.1)$$

In equation 5.1, f is the frequency value, μ is permeability with the value of 4π x 10^{-7} H/m and σ is conductivity with a value of 5.8 x 10^{7} for Cu. For example, the skin depths of Cu at 40 GHz, 67 GHz and 110 GHz are 330 nm, 255 nm and 199 nm, respectively. Considering the Cu NWs used in this work has the diameter of 20 nm, which is far less than the skin depth in the frequency bands of interest, they are expected to provide benefits of high RF field penetration and low conductor loss.

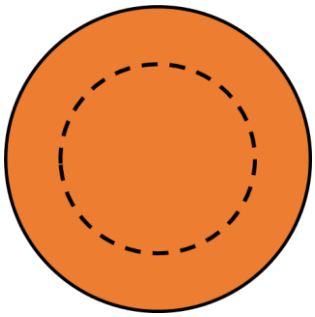

Fig 5.1. Cross section of a conductor with skin depth effect.

5.3 Cu NW via as vertical interconnect on Si

To use NWs as vertical interconnect, both their AC and DC properties are important and need to be studied.

In this work, the DC resistivity measurement is implemented based on integrated Cu NWs with 1.7 μm wire length, 20 nm pore diameter and 9 % porosity. The measured DC resistance and calculated resistivity are 261 Ω and 4.82 μΩ-cm, respectively. This result aligns well with published research on the DC resistivity of Cu NW [60]-[61].

For AC properties study, NW via design based on a transmission line is used and will be discussed in the section.

5.3.1 Design and simulation of CPW line with NW vias

5.3.1.1 Design of CPW line with NW vias

The NW vias are built on CPW structures. For AC operation, two CPW designs are developed, CPW design A (CPW-A) and CPW design B (CPW-B). For CPW-A, the width of signal line, slot, and ground are 93.9 µm, 53.05 µm and 400 µm, respectively. The CPW-A total width is 1000 µm which guarantees single mode operation up to 60 GHz. For CPW-B, the width of signal line, slot, and ground are 40 µm, 20 µm and 140 µm, respectively. The CPW-B total width is 360 µm which corresponds to the single mode operation up to 167 GHz. The total width of CPW-A is 2.78 times wider than CPW-B.

For both CPW configuration, two types of NW via are designed. Type 1 has a via width (VW) that is similar to the signal line and ground width; whereas Type 2 via has a fixed width and is centered on the signal line plane (S) and ground plane (G). The top views of both are shown in Fig 5.2, where VW and via length (VL) are defined.

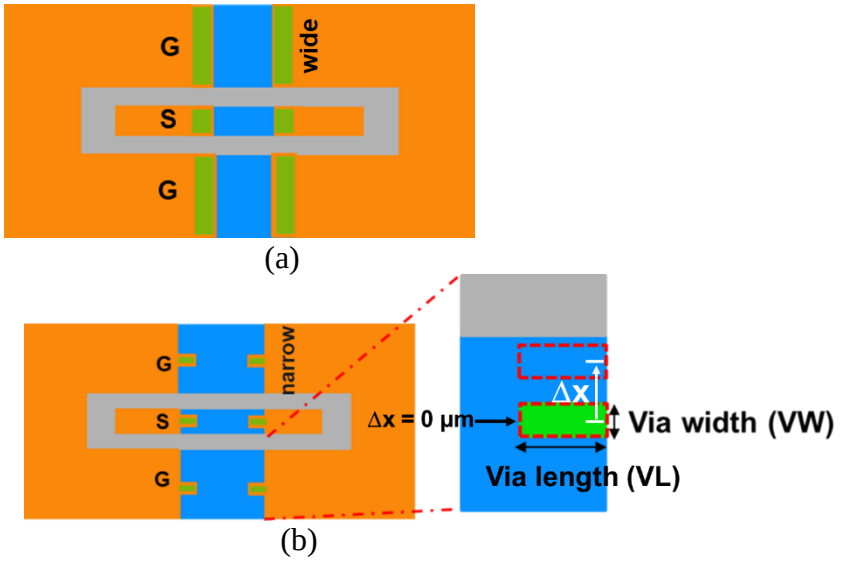

Fig 5.2. Top view of Type 1 and Type 2 NW via. (a) Type 1 NW via. (b)Type 2 NW via.

For CPW-A with Type 1 NW via design, VW on the S and G plane are 80 µm and 390 µm, respectively. For CPW-B Type 1 NW via design, VW on the S and G plane are 30 µm and 130 µm, respectively. For both cases, VL is 90 µm.

TABLE 5.1
SUMMARY OF TYPE 2 VIA DIMENSIONS

CPW design	VL (µm)	VW (µm)
A	30	S = G = 70
	90	S = G = 30
	90	S = G = 70
	150	S = G = 30
B	90	S = G = 20
	150	S = G = 20

Type 2 via with different VWs and VLs are designed and studied to determine the via dimension effect. The dimensions considered for Type 2 vias are shown in Table 5.1. The VL ranges from 30 to 150 µm and the VW is 20, 30 or 70 µm.

A study is also performed to determine the optimal via location on the G plane by comparing Δx, the offset values relative to the G plane midpoint. The via location with Δx = 0 µm is at the midpoint of the G plane, shown in Fig. 5.2b.

Layouts of one-unit and five-unit CPW with NW via design are shown in Fig 5.3. In Fig 5.3a, a one-unit cell circuit is comprised of three sections: a Via-AAO-CPW section and two CPW feed lines (L2). The Via-AAO-CPW section is comprised of two rectangular NW vias, two via to CPW transitions (T1) and a CPW line below AAO section (L1). To enhance the signal level of vias, a five-unit CPW circuit (Fig 5.3b) is designed to include 5 Via-AAO-CPW sections for a total of 10 NW vias.

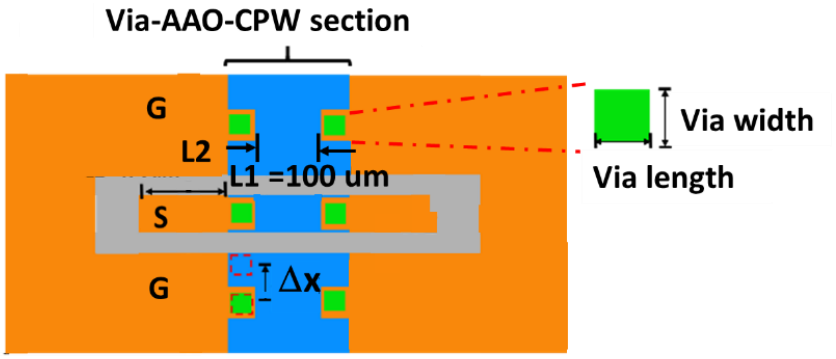

(a)

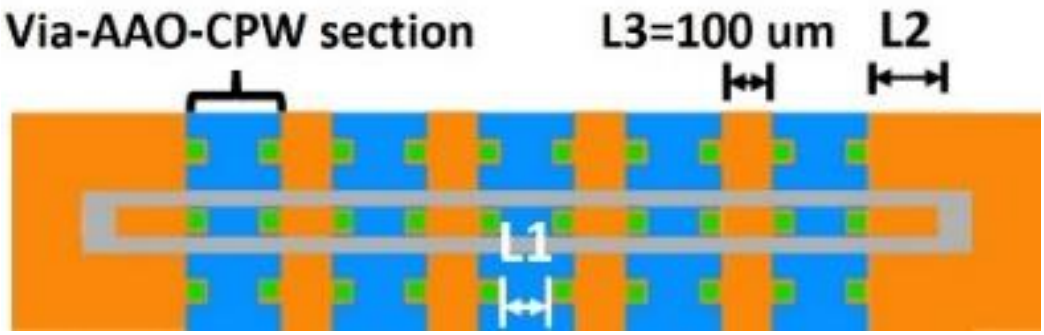

(b)

Fig 5.3. Top view of CPW with NW via design: (a) One-unit CPW with NW via; (b) Five-unit CPW with NW via.

The total length of the one-unit and five-unit circuits are defined in equation 5.2 and equation 5.3, respectively. The L1 and L3 terms describe the length of CPW line below AAO and CPW line between the Via-AAO-CPW sections (Fig 5.3), and both of them are 100 µm. The T1 and T2 terms describe the length of the via to CPW transition region and the alignment gap, which are 10 µm and 5 µm respectively. L2 denotes the feedline length. For CPW-A and CPW-B, the L2 values are 460 µm and 180 µm, respectively. As an example, if a one-unit CPW-A design with Type 1 via has a VL of 90 µm, the total length of the circuit will be 1220 µm.

$$L_{\text{one-unit, CPW with NW via}} = L1+2*L2+2*VL+2*T1 \quad (5.2)$$

$$L_{\text{five-unit, CPW with NW via}} = 5*L1+2*L2+4*L3+10*T1+8*T2+10*VL \quad (5.3)$$

In general, a length equation of a N-unit CPW with NW via (N>1) can be expressed using equation 5.4.

$$L_{\text{N-unit, CPW with NW via}} = N*L1+2*L2+(N-1)*L3+2*N*T1+2*(N-1)*T2+2*N*VL \quad (5.4)$$

5.3.1.2 Simulation results of CPW line with NW vias

In this study, NW vias of different configurations are simulated using HFSS. Since the simulation results of one-unit CPW with different via dimensions doesn't show significant difference, only five-unit CPW models are shown.

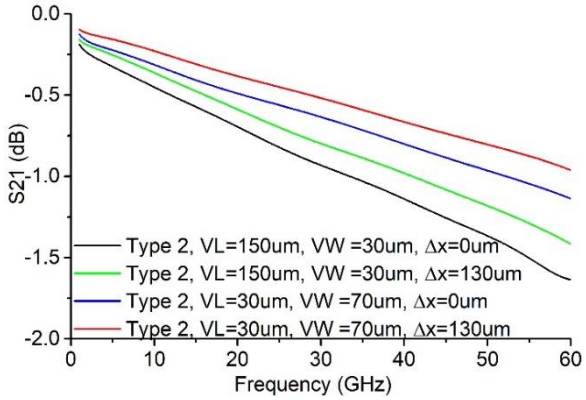

(a)

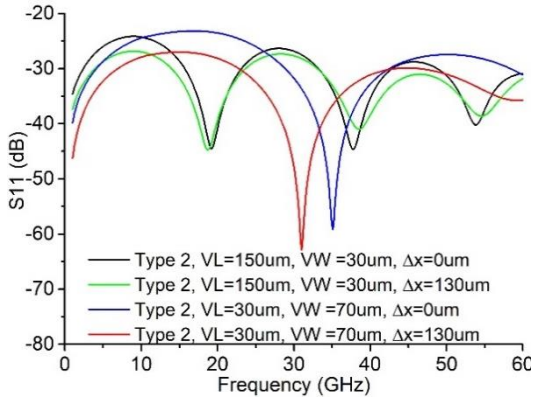

(b)

Fig 5.4. Simulation results of five-unit CPW-A with Type 2 NW vias: (a) S21 data in dB; (b) S11 data in dB.

The simulation results of five-unit CPW-A with Type 2 NW vias are shown in Fig 5.4. The via dimensions that have the best (VL = 30 μm, VW =70 μm, Δx =130 μm) and

worst (VL = 150 µm, VW=30 µm, Δx=0 µm) performance have a transmission loss (S21) difference of 0.475 dB at 40 GHz. The via position is studied by comparing the same vias dimensions but at different Δx location, such as blue and red curves shown in Fig 5.4. The blue curve corresponds to Δx = 0 µm and red curve corresponds to Δx = 130 µm. When the via in G plane is shifted from the midpoint (Δx =0 µm) to the inner edge of slot (Δx = 130 µm), the S21 and S11 of red curve shows higher

and lower values, respectively, compare to the blue curve. This indicates that the via design expressed in red with Δx = 130 µm has lower mismatch, more signal power transmission and therefore improved overall performance.

Next, the simulation data of five-unit CPW-B with Type 1 and Type 2 NW vias are plotted in Fig 5.5. Type 1 via shows highest S21 and therefore lowest insertion loss due to its wide VW dimensions on S and G plane, which provides the largest area for current to flow. For Type 2 vias with the same VW, as VL increases, the transmission path increases and therefore higher insertion loss is observed. Similar to the simulation results of CPW-A, via position with higher Δx in CPW-B provides better performance.

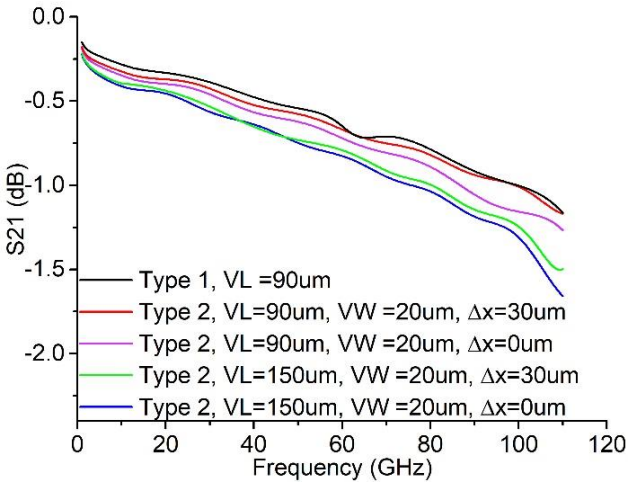

(a)

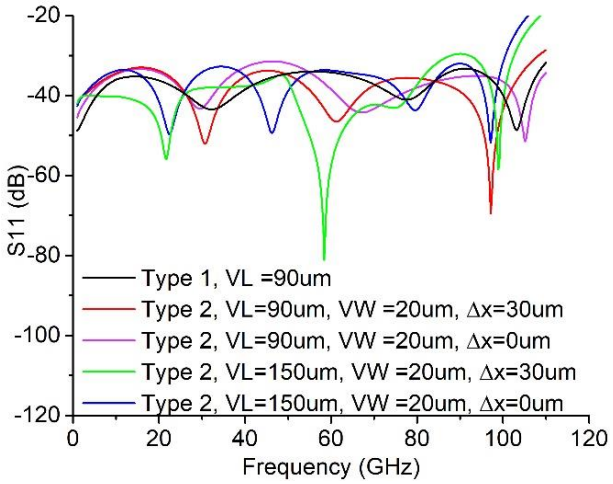

(b)

Fig 5.5. Simulation results of five-unit CPW-B with NW vias: (a) S21 data in dB; (b) S11 data in dB.

The simulation results indicate that via dimension with wider VW, shorter VL and larger Δx should be designed for low loss via, and the experiments will be performed to validate it. To do so, a fabrication processes is needed to create these NW structures and will be presented in the next section.

5.3.2 Fabrication processes of CPW line with NW and conventional vias

Two processes, Process I and Process II, are developed for Cu NW vias fabrication. These processes create integrated NW vias in integrated AAO (iAAO) on Si. In Process I, NW in iAAO is fabricated before patterning. In Process II, however, NWs are only allowed to grow in patterned iAAO via regions. A conventional via fabrication process is also developed based on iAAO on Si and are used as the reference.

5.3.2.1 Fabrication processes of Process I: NW in iAAO as a uniform layer

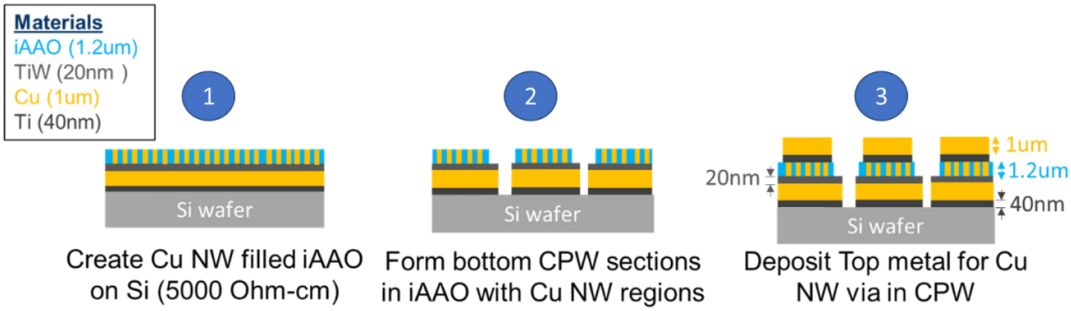

(a) (b) (c)

Fig 5.6. Fabrication process for Process I.

The fabrication processes for Process I NW via is shown in Fig 5.6. The fabrication starts with a 500 µm thick high resistivity Si wafer with a deposited Cu layer. The Si wafer in use has a resistivity value of greater than 5000 Ohm-cm. Then, an evaporated aluminum (Al) layer is deposited on the Cu layer and anodized into 1.2 µm thick iAAO. The iAAO is next pore widened to an average of 20 nm pore diameter and 9% porosity. Next, Cu NWs are grown in the iAAO template using an electrodeposition process [62]. In step two, shown in Fig 5.6b, the back etching process is used to create bottom CPW lines. And the last step, shown in Fig 5.6c, deposits a top Cu layer to make connection between top and bottom CPW and form the NW via.

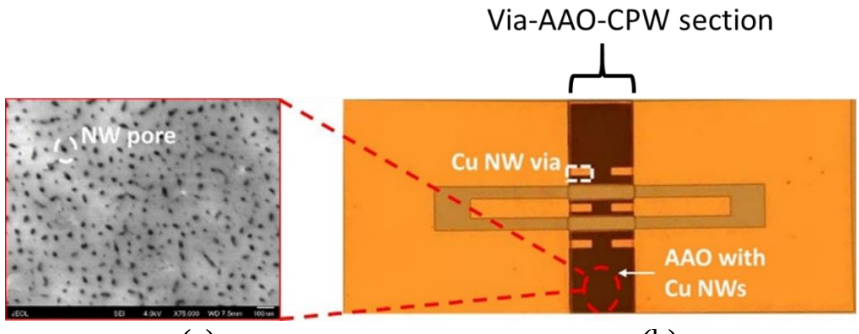

(a) (b)

Fig 5.7. (a) Scanning electron microscope (SEM) image of NW pore on iAAO surface. (b) Fabricated one-unit cell CPW with Type 2 NW via based on Process I.

Fig 5.7 shows an example of a one-unit circuit with Type 2 via using Process I fabrication method. All AAO regions have NW filling are shown as dark brown in Fig 5.7b. Only the via region connects the top feedline section, shown in gold, and bottom CPW lines under iAAO with NWs.

5.3.2.2 Fabrication processes of Process II: Cu NW in iAAO via region only

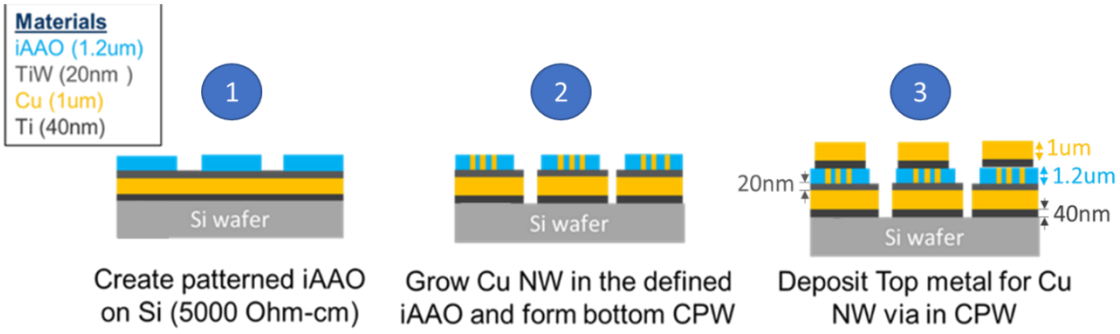

Fig 5.8. Fabrication process for Process II.

In Fig 5.8, the Process II fabrication starts with an empty iAAO layer above Cu electrode. In step one, the iAAO are back etched to form the CPW (S and G plane). Then in step two, shown in Fig 5.8b, the Cu NWs are grown in the iAAO in via region only. In last step, shown in Fig 5.8c, the top metal is deposited to make the connection between top and bottom lines and to form the vias.

A five-unit circuit fabricated with Process II method is shown in Fig 5.9, where the NWs are only grown in the via region. The iAAO, shown in non-via regions of the Via-AAO-CPW section is empty.

Circuits fabricated with Process I and Process II have similar via areas, but the number of NWs grown in S and G plane is lower in Process II.

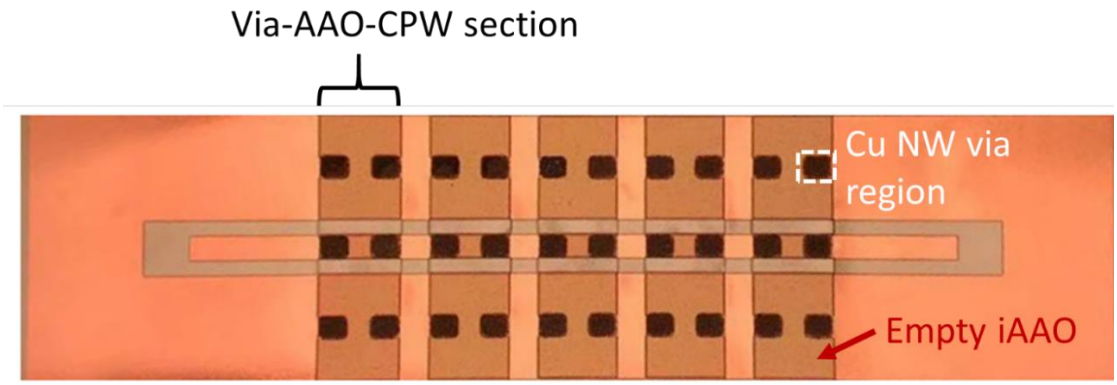

Fig 5.9. Fabricated five-unit CPW circuit with NW vias based on Process II.

5.3.2.3 Fabrication processes of conventional via

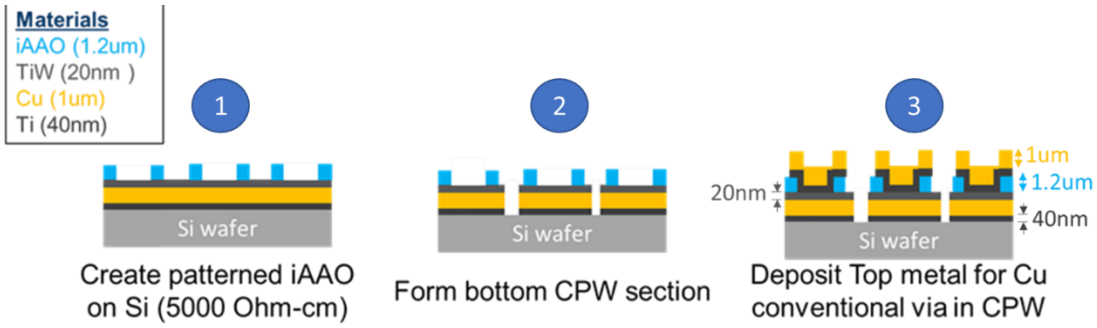

Fig 5.10. Fabrication process for conventional via.

Fig 5.10 shows the fabrication process of conventional vias. The conventional via is fabricated on Si wafer after empty iAAO is removed as described next.

In step one, shown in Fig 5.10a, the empty iAAO is removed in the CPW slot and via regions. Then, the Cu electrode layer is etched to form bottom CPW line (Fig 5.10b). Lastly, the top metal is deposited to form the conventional via (Fig 5.10c).

A fabricated five-unit circuit with conventional vias is shown in Fig 5.11, where iAAO is removed in the conventional via region.

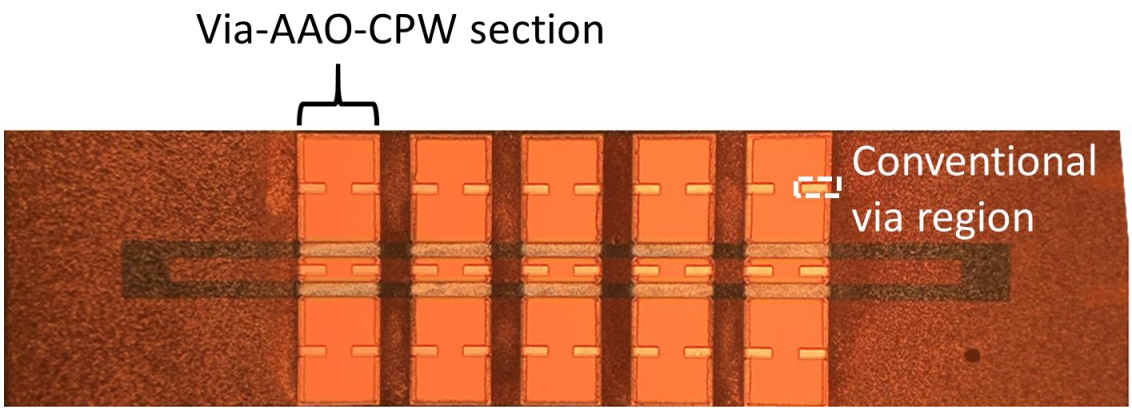

Fig 5.11. Fabricated five-unit CPW circuit with conventional vias.

5.3.3 Measurement of NW via and conventional via

To obtain an understanding of NW vias AC properties, NW via measurements are implemented in three different frequency bands. They are 0.04-40 GHz, 0.01-67 GHz, and 0.01-110 GHz. The measurement set-up and results for Process I and Process II NW vias will be shown in this section. Then their results will be compared to conventional vias to understand the advantages of NW vias.

5.3.3.1 Measurement system set up

(1) Measurement system set-up up to 40 GHz

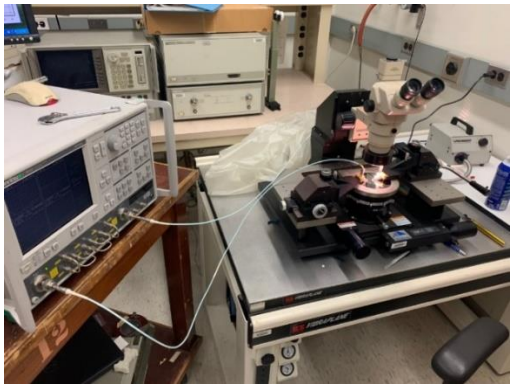

Fig 5.12. Measurement system for frequencies up to 40 GHz

The measurement system set-up for frequencies up to 40 GHz is shown in Fig 5.12. An Anritsu 37369D VNA operating from 0.04 GHz to 40 GHz is used and connected to a Cascade RF-1 probe station. A 500 μm thick high resistivity (>5000 Ω-cm) Si wafer is placed between the measurement sample and the metallic chuck for isolation. Line-reflect-reflect-match (LRRM) calibration is performed using Cascade ACP50 probes with pitch of 150 μm and an ISS 101-190 calibration chip to shift reference plane to the probe tip.

(2) Measurement system set-up up to 67 GHz

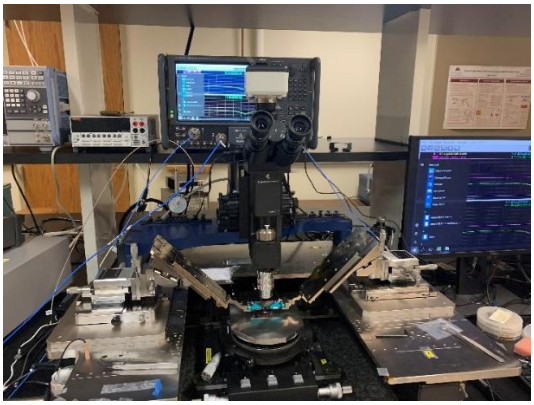

Fig 5.13. Measurement system for frequencies up to 67 GHz.

The measurement set-up for frequencies up to 67 GHz is shown in Fig 5.13. A Keysight PNA operating from 0.01 GHz to 67 GHz is connected to a Cascade probe station. LRRM calibration is performed with Cascade IXT67 probes (pitch of 150 μm) and an ISS 101-190 calibration chip to shift the reference plane to the probe tip.

(3) Measurement system set-up up to 110 GHz

The measurement set-up for frequencies up to 110 GHz is shown in Fig 5.14. A Keysight VNA 8361C operating from 0.01-110 GHz is connected to a Cascade probe i110 with pitch of 50 μm. LRRM calibration method is performed with ISS138-357 calibration substrate to shift reference plane to the probe tip.

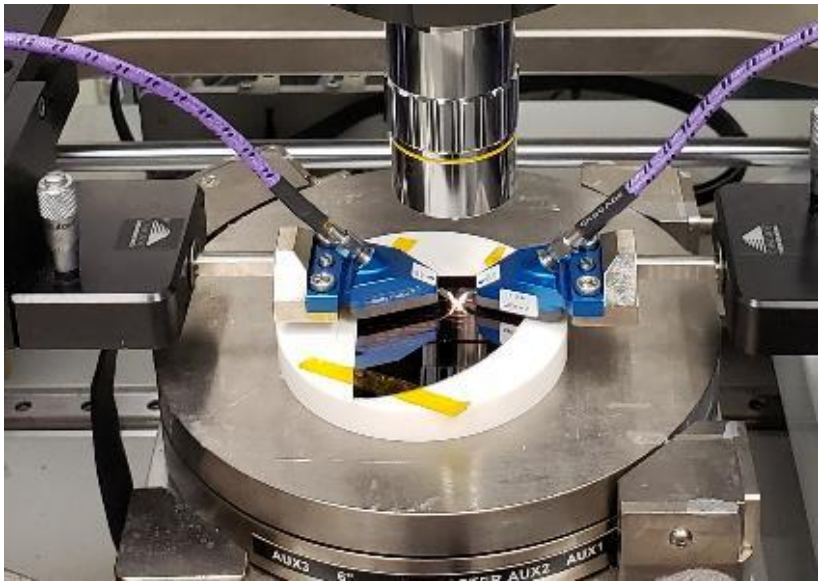

Fig 5.14. Measurement system set-up for frequencies up to 110 GHz.

5.3.3.2 Process I NW vias

A specific CPW design is created for each frequency band, where CPW-A and CPW-B with NW vias are characterized up to 40 GHz and 110 GHz, respectively. The NW vias in this section are developed using Process I method. CPW with NW vias and a reference CPW are measured, the modeled and experimental results of CPW with NWs are compared, NW via dimension study is implemented and NW via loss is extracted and shown.

5.3.3.2.1 40 GHz results of CPW-A with NW vias using Process I

(a) Measurement results and comparison [63]

Fig 5.15 shows measurement results of a one-unit CPW-A with Type 1 NW via and a 1224 μm reference CPW line. The trend of the data is similar across the band. Type 1 NW via transmission loss is lower than the reference CPW up to 25 GHz. Above 25 GHz,

Type 1 NW vias shows higher transmission loss. The results indicate that Cu NW-based vias provide similar if not better performance to a conventional planar CPW lines.

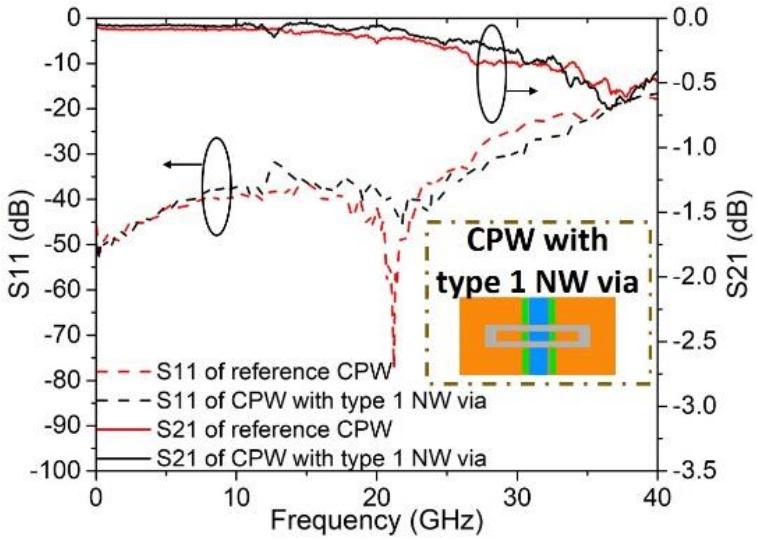

Fig. 5.15. Comparison of one-unit CPW-A with Type 1 vias based on Process I and 1224 µm reference line, where VL= 90 µm, VW = 80 µm and 390 µm on S and G, respectively.

Fig 5.16 compares the measurement and simulation of five-unit CPW-A with Type 2 NW vias. The via area dimensions of VL=30 µm and VW =70 µm are located at Δx =0 µm. In the simulation, the micron-sized Cu pillar model, discussed in Chapter 2, is used to approximate the 9% porosity of NW vias. The comparison of S21 data shows that measurement results follow a similar trend to the predicted response from the simulation. The measured S11 data is, however, worse than predicted which might be due to the fabrication defects, such as over etching of the CPW slot.

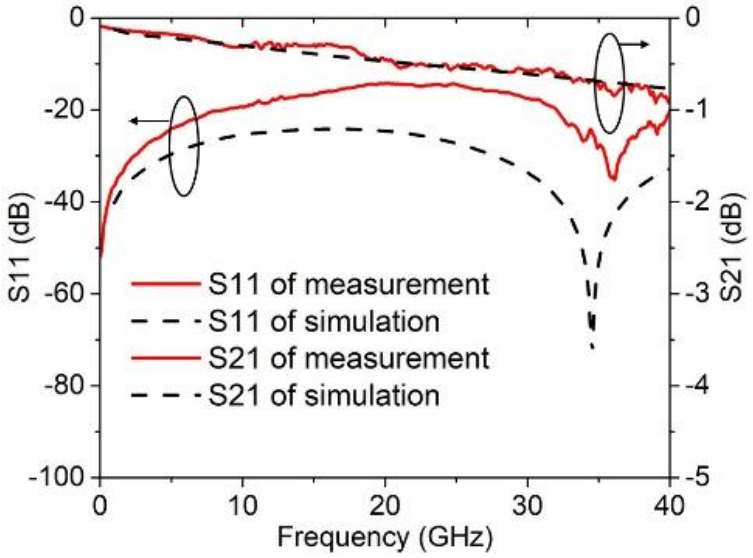

Fig 5.16. Comparison of HFSS simulation and measurement results of five-unit CPW-A with Type 2 NW vias based on Process I. VL=30 μm, VW =70 μm and Δx =0 μm.

Fig 5.17a shows the measurement results of a via width study for five-unit CPW-A with Type 1 and Type 2 NW vias. Three fabricated NW via structures are shown in Fig 5.17b. All have the same VL of 90 μm. Type 1 NW vias have VW of 80 μm and 390 μm on the S and G plane, respectively. Two Type 2 NW vias are used and have the same VW on the S and G plane. One has a VW of 70 μm and the other has a VW of 30 μm. When VL is fixed, an increase in VW produces reduced insertion loss and reduced reflection coefficient, and therefore better performance. CPW with Type 1 NW via shows the best performance due to its widest VW on both S and G plane, which provides more area for current to flow through. Therefore, the wider VW is preferred for via dimension design.

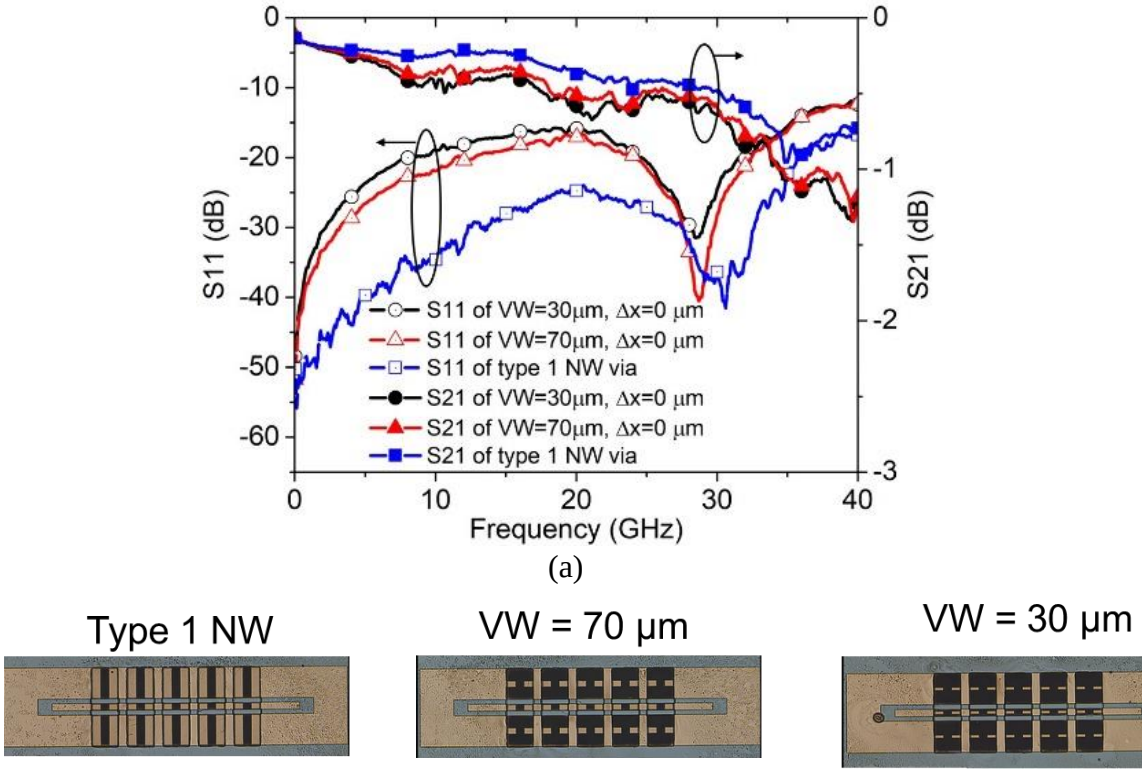

Fig 5.17. Via width comparison of five-unit CPW-A with NW vias based on Process I. For all three circuits, VL =90 μm, VW ranges from 30 μm to 390 μm. (a) Measurement results; (b) Fabricated structures.

Fig 5.18 shows the measurement results of a via length study for five-unit CPW-A with Type 2 NW vias. VW is fixed at 30 μm. The circuits with longer VL of 150 μm show higher insertion loss compared to the shorter VL of 90 μm. This is because the longer VL introduces a longer signal path which results in higher insertion loss. Therefore, shorter VL is preferred for via dimension design.

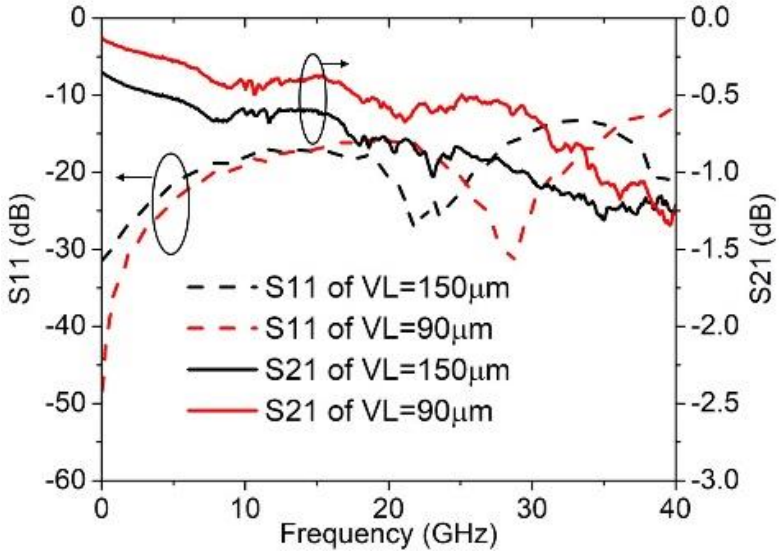

Fig 5.18. Via length comparison of five-unit CPW-A with Type 2 vias based on Process I in measurement results. For both circuits, VW =30 μm, Δx =0 μm, VLs are 90 μm and 150 μm.

Fig 5.19a shows the measurement results of a via position study for five-unit CPW-A with Type 2 NW vias. Δx is used to describe the via offset relative to the midpoint in the ground plane width. Both circuits have the same via dimensions, VW =70 μm, VL=90 μm. The circuits with via position at Δx = 0 μm and Δx = 130 μm are shown in Fig 5.19b. From the measurement results, higher Δx shows lower insertion loss. Therefore, putting the via position on G closer to S provides better via performance.

So far, all the via dimension and position study results aligns well with the simulation trend shown in chapter 5.2.1.2. For low loss via design, wider VW, shorter VL and larger Δx is preferred.

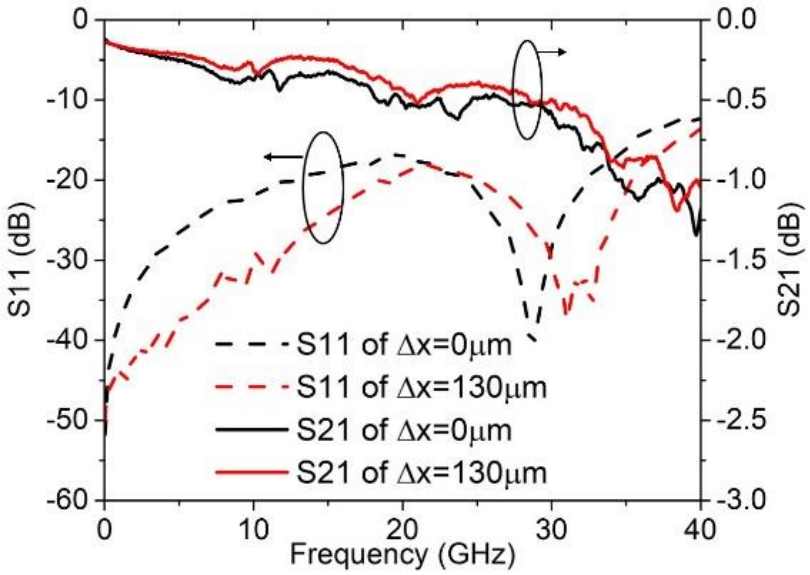

(a)

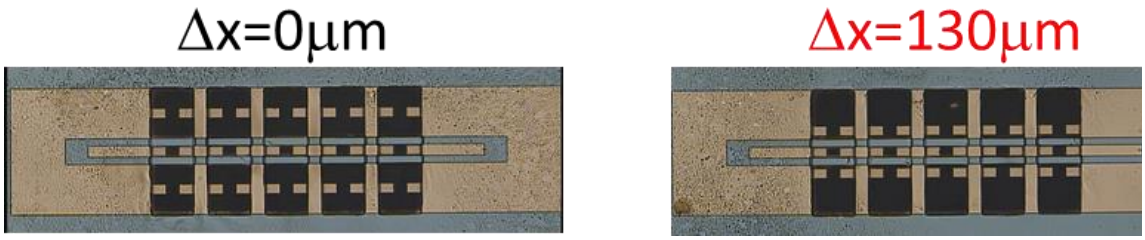

(b)

Fig 5.19. Δx comparison of five-unit CPW-A with Type 2 vias based on Process I in measurement results. For both circuits, VW =70 μm, VL=90 μm. Δx is 0 μm and 130 μm. (a) Measurement results; (b) Fabricated structures.

(b) Sing G-S-G via loss extraction

To compare the NW via in this work and other advanced via technologies, the via loss of single G-S-G via is needed. To achieve that, extracting the loss of Via-AAO-CPW section is required first. The data of five-unit CPW-A with Type 1 NW via, plotted in Fig 5.17a will be used to determine the loss for specific via type.

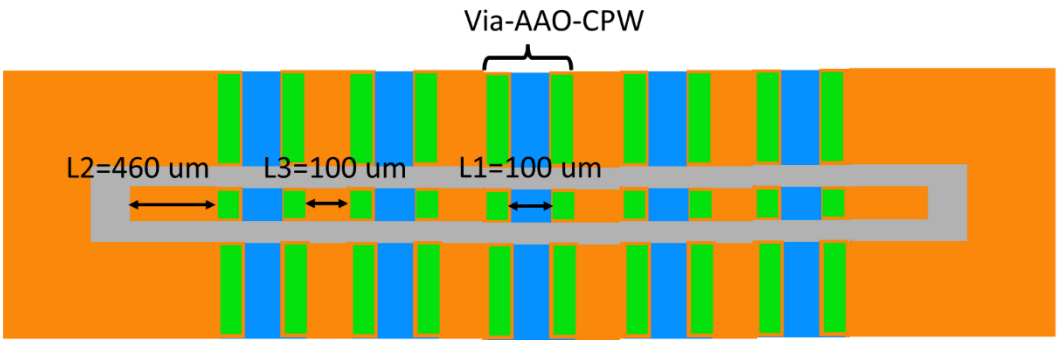

Fig 5.20. Top view of five-unit CPW with Type 1 NW vias.

Fig 5.20 shows a five-unit CPW with vias includes two feed line (L2), four CPW sections (L3) and five Via-AAO-CPW sections. To find the loss of one Via-AAO-CPW section, the influences from different CPW line segments (L2 and L3) must be removed. To do that, a de-embed method based on transmission matrix ([T]), is used. The [T] matrix is obtained from the conversion of [S] matrix using equation 5.5, equation 5.6, equation 5.7 and equation 5.8 [51].

$$T_{11} = \frac{-(S_{11}*S_{22}-S_{12}*S_{21})}{S_{21}} \quad (5.5)$$

$$T_{12} = \frac{S_{11}}{S_{21}} \quad (5.6)$$

$$T_{21} = \frac{-S_{22}}{S_{21}} \quad (5.7)$$

$$T_{22} = \frac{1}{S_{21}} \quad (5.8)$$

Then, five-unit CPW with NW vias can be expressed with the multiplication of [T] matrix from each section using equation 5.9, where $T_{\text{five-unit, CPW with NW via}}$ is [T] matrix of five-unit CPW with NW via, T_{L2} is [T] matrix of L2 section, $T_{\text{via-AAO-CPW}}$ is [T] matrix of Via-AAO-CPW section and T_{L3} is [T] matrix of L3 section.

$$T_{\text{five-unit, CPW with NW via}} = T_{L2} * (T_{\text{via-AAO-CPW}} * T_{L3})^4 * T_{\text{via-AAO-CPW}} * T_{L2} \quad (5.9)$$

Next, T_{L2} and T_{L3} are calculated using measurement results of two standard CPW lines, C1 and C2: 1) C1 is comprised of two L2 sections and one L3 section with the total line length of 1020 µm; 2) C2 is comprised of the two L2 sections and two L3 section with the total length of 1120 µm. The [T] matrix of C1 (T_{C1}) and C2 (T_{C2}) can be expressed using equation 5.10 and 5.11.

$$T_{C1}=T_{L2}*T_{L3}*T_{L2} \quad (5.10)$$

$$T_{C2}= T_{L2}*T_{L3}*T_{L3}*T_{L2} \quad (5.11)$$

Then, T_{L2} and T_{L3} are acquired using equation 5.12 and equation 5.13.

$$T_{L2}=(T^{-1}_{C1}*T_{C2}*T^{-1}_{C1})^{1/2} \quad (5.12)$$

$$T_{L3}= T^{-1}_{L2}*T_{C1}* T^{-1}_{L2} \quad (5.13)$$

Based on T_{L2} and T_{L3} and $T_{\text{five-unit, CPW with NW via}}$, [T] matrix of Via-AAO-CPW, $T_{\text{via-AAO-CPW}}$, is obtained in equation 5.14.

$$T_{\text{via-AAO-CPW}} = (T^{-1}_{L2} * T_{\text{five-unit, CPW with NW via}} * T^{-1}_{L2} * T_{L3})^{1/5} * T^{-1}_{L3} \quad (5.14)$$

By converting $T_{\text{via-AAO-CPW}}$ back to the [S] matrix, the insertion loss of a Via-AAO-CPW section is acquired and has the value of 0.043 at 20 GHz, 0.07 at 30 GHz and 0.095 at 40 GHz (in dB).

Next, to find the loss of a single G-S-G via, the loss of CPW below AAO section (L1) needs to be removed from the Via-AAO-CPW section data. The simulation results of CPW below AAO is used to approximate the loss, which is calculated using S parameters based on equation 5.15 [51]. The loss value is 0.024 at 20 GHz, 0.0379 at 30 GHz and 0.04 at 40 GHz (in dB).

$$Loss = -10 * \log_{10}\left(\frac{|S_{21}|*|S_{12}|}{1-|S_{11}|*|S_{22}|}\right) \qquad (5.15)$$

Therefore, the loss of each Type 1 NW G-S-G via loss is 0.0095 at 20 GHz, 0.016 at 30 GHz and 0.0275 at 40 GHz (in dB).

Table 5.2 shows the comparison of the Type 1 via design to other via technologies. Compared to the via from the other work, the vias in this work has much thinner thickness and the lowest single G-S-G via loss with the value of approximately 0.0275 at 40 GHz.

TABLE 5.2
COMPARISON OF VIA TECHNOLOGIES FOR MILLIMETER-WAVE FREQUENCY RANGE

Ref.	Substrate Type	Loss of one G-S-G via (dB)	Insertion loss of test line with two G-S-G vias at 40 GHz (dB)	Via size	Via Thickness (μm)	Line Length (mm)
[21]	Si: 5000 Ω·cm resistivity	0.53 at 75 GHz	0.93	Via diameter =42 μm	252	3.15
[22]	Si: High resistivity	0.03 at 40 GHz	~ 0.3	Via diameter =200 μm	100	2.7
[23]	AAO	0.035 at 40 GHz	~ 0.21	20×30 μm^2	50	0.200
This work	Si: 5000 Ω·cm resistivity (CPW) & AAO (via)	~ 0.0275 at 40 GHz	0.095 (Via-AAO-CPW section)	S: VL x VW = 90 μm×80 μm G: VL x VW = 90μm×390 μm	1.2	0.300

The total loss of a test line with two G-S-G vias is compared in the fourth column of the Table 5.2. In [23], a 0.2 mm long signal line with two 50 μm thick vias is presented and have total signal path length of 0.3mm, which is very similar to that in this work. Yet, the total loss for this work, 0.095 dB at 40 GHz, is 45 % of that in [23]. This comparison shows promise for the proposed via technology in this work.

5.3.3.2.2 110 GHz results of CPW-B with NW via using Process I

The CPW-B with NW vias are fabricated and measured up to 110 GHz Process I. The measurement system set-up was shown in Fig 5.14. Fig 5.21 shows the five-unit CPW-B with Type 1 and Type 2 NW vias that is measured in this section.

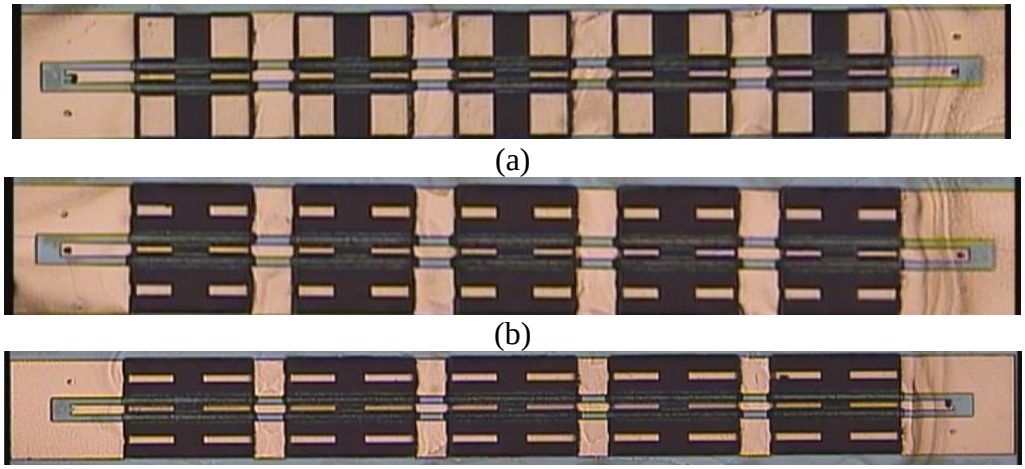

Fig 5.21. Fabricated five-unit CPW-B with NW vias based on Process I. (a) Type 1 via with VL= 90 µm and VW = 30 µm and 130 µm on S and G, respectively; (b) Type 2 via with VL= 90 µm, VW = 20 µm and Δx = 0 µm; (c) Type 2 via with VL= 150 µm, VW = 20 µm and Δx = 0 µm.

Fig 5.22 shows measurement results of a five-unit CPW-B with Type 1 NW via and a 2320 µm reference CPW line. The trend of the data is similar across the band. Type 1 NW via transmission loss is higher than that of the reference CPW up to 75 GHz. Above 75 GHz, Type 1 NW vias shows lower transmission loss. These results indicate that in CPW-B Cu NW-based vias provides better performance to a conventional planar CPW lines above 75 GHz.

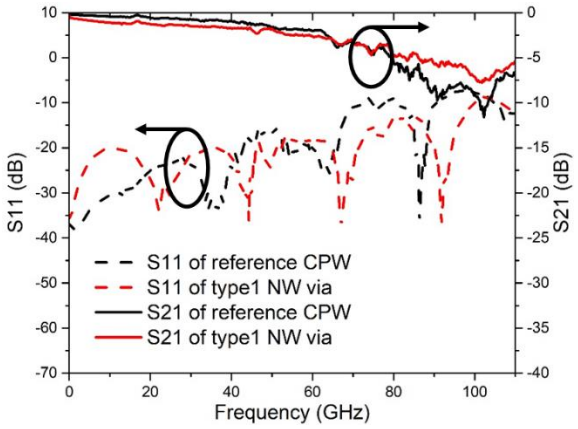

Fig 5.22. Comparison of five-unit CPW-B with Type 1 NW via based on Process I and its 2320 µm reference CPW line. For Type1 NW vias, VL=90 µm, and S and G has VW = 30 µm and 130 µm, respectively.

Fig. 5.23 shows the comparison of CPW-B circuit with Type 1 and Type 2 NW vias. Both designs have VL fixed at 90 µm. Type 1 NW via has VW of 30 µm and 130 µm on S and G plane, respectively. Type 2 via has VW of 20 µm. CPW with Type 1 NW via shows lower insertion loss and lower reflection coefficient compared to that of Type 2 NW via. This is because Type 1 via possesses wider VW for both S and G plane which provide larger cross section for current to go through. This conclusion aligns with the via width study for CPW-A, discussed in chapter 5.2.3.2.1. The results confirm that for via design in both 40 GHz and 110 GHz frequency bands, wider via width is preferred for lower loss.

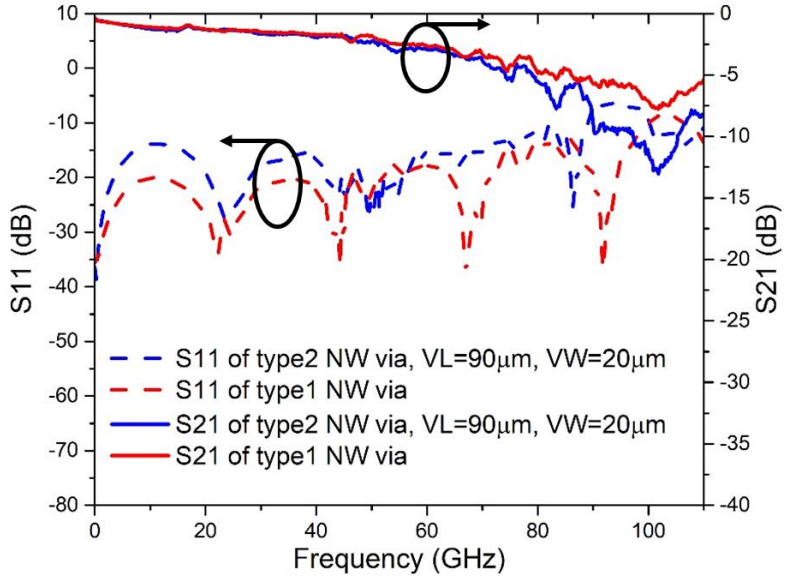

Fig 5.23. Comparison of five-unit CPW-B with Type 1 and Type 2 NW vias based on Process I. For Type1 NW vias, VL=90 µm, and S and G has VW = 30 µm and 130 µm, respectively. For Type 2 NW via, VL=90 µm, VW = 20 µm and Δx= 0 µm.

Fig 5.24 shows the NW VL study for CPW-B with Type 1 NW via. The VW is fixed at 20 µm. The VL of 90 µm and 150 µm are studied. Similar to the VL study for CPW-A, the conclusion of VL study based on CPW-B is that longer VL performs worse

due to the longer signal path and therefore higher introduced insertion loss. Therefore, for via design in both 40 GHz and 110 GHz frequency bands, shorter VL is preferred.

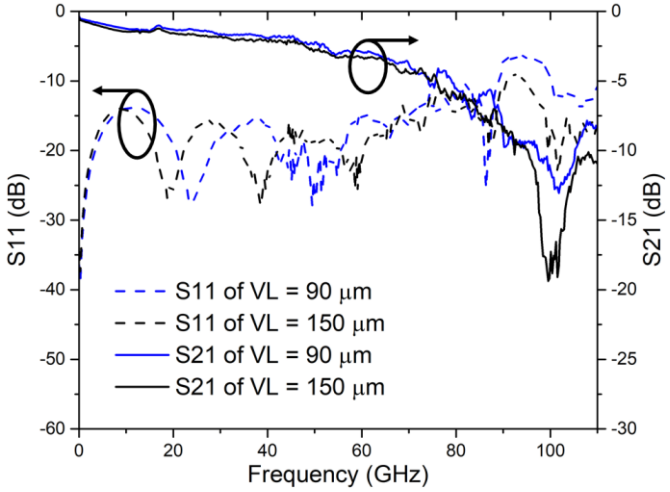

Fig 5.24. VL study of five-unit CPW-B with Type 2 NW via based on Process I. For both circuits, VW = 20 μm and Δx =0 μm.

In general, NW via based on Process I shows promising results compared to reference CPW. Via dimension and position effect study shows that wider VW, shorter VL and larger Δx provides better performance.

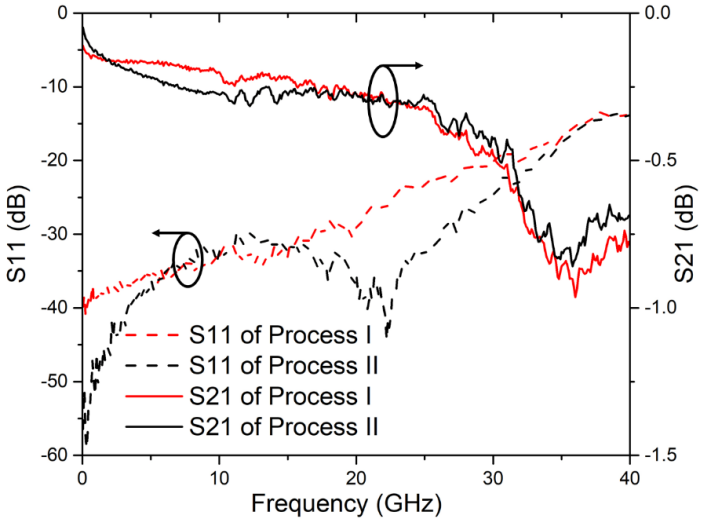

Fig 5.25. Comparison of NW via based on Process I and Process II using one-unit CPW-A, where VL=150 μm, VW = 30 μm and Δx =130 μm.

5.3.3.3 Comparison of Process I and Process II NW vias

In this section, NW via will be performed using Process II, where NWs are grown only in the via region, whereas Process I NW via has NWs grown in all AAO regions. Due to fabrication differences, compared to Process I, Process II NW vias have lower filling factor and extra Cu above the AAO substrate. A lower NW filling factor is expected to impact and degrade the RF performance, whereas extra Cu above the AAO provides extra current flow region and therefore improves the performance.

Therefore, the measurement of Process II NW via and its comparison with the Process I is needed.

Fig 5.25 shows the results of one-unit CPW-A with NW vias based on Process I and Process II. Measurements are performed and compared up to 40 GHz. For both S11 and S21 data, Process II and I show close performance despite of different number of NWs and extra Cu above iAAO.

5.3.3.4 Comparison of NW and conventional vias

The NW vias are compared to conventional vias to determine if the NW structure provides a benefit. If so, quantifying the benefit of NW via performance needs to be implemented.

Fig 5.26 shows the comparison of five-unit CPW-A with Type 2 NW based on Process I and conventional vias in the 67 GHz. The via dimensions are VW = 30 μm, VL = 90 μm, and located at $\Delta x = 0$ μm. When compared to the conventional vias, NW via based on Process I shows lower insertion loss but higher reflection coefficient. It is not clear which type of via performs better.

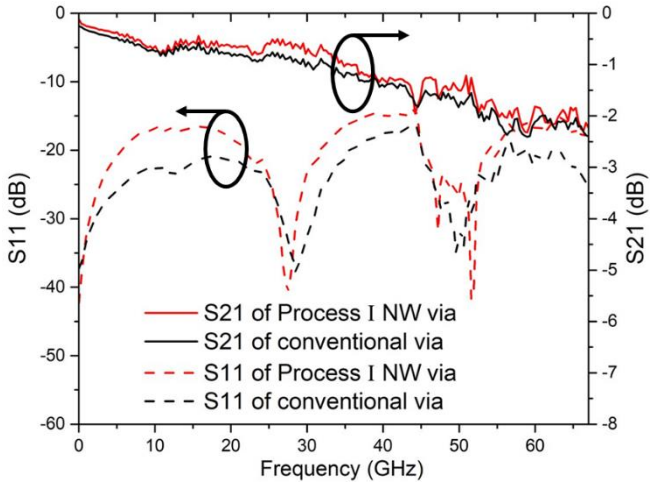

Fig 5.26. Comparison of Type 2 NW via based on Process I and conventional via. VW =30µm, VL=90µm and Δx = 0µm.

Fig 5.27 shows the comparison of five-unit CPW-A with Type 2 NW based on Process II and conventional vias in the 67 GHz. The via dimensions are VW = 70 µm, VL = 30 µm, and located at Δx = 130 µm. When compared to the conventional vias, NW via based on Process II shows lower insertion loss across the 67 GHz band and lower reflection coefficient up to 32.17 GHz.

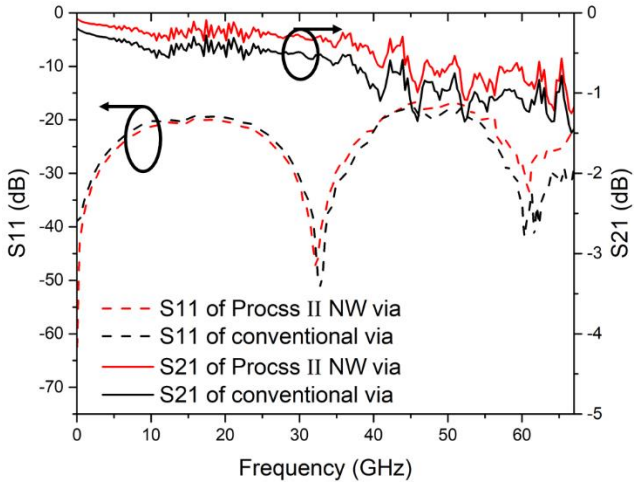

Fig 5.27. Comparison of Type 2 NW via based on Process II and conventional vias, where VW= 70µm, VL = 30 µm, Δx = 130µm.

So far, the comparison of NW and conventional vias is based on a full five-unit circuit and depends on two S parameters, S11 and S21. The fabrication variation of different CPW sections such as feedline (L2) and CPW line between Via-AAO-CPW sections (L3) introduces the error. Also, two S parameters can provide opposite conclusion for via performance. Therefore, it is difficult to determine which type of vias perform better. The total loss of Via-AAO-CPW section for each type of via needs to be extracted and used to do a further comparison.

To obtain the loss of Via-AAO-CPW section up to 67 GHz, a different de-embed method is required to be used for analyzing the NW and conventional vias. Previously in chapter 5.3.3.2.1, the loss of Via-AAO-CPW is determined by removing the loss of L2 and L3 sections in the five-unit circuit using the transmission matrix extraction method. However, above 40 GHz, for line lengths of 1020 μm and 1120 μm associated with L2 and L3, respectively, the contact repeatability introduces unwanted noise, and the signal variation produces unwanted resonances in the extraction matrix data. To overcome this problem, a new method is used that excludes consideration of L2 and L3 loss, explicitly.

The new method, described by equation 5.17, uses the calculated value for total loss of five-unit CPW with vias ($Loss_{five-unit\ circuit}$) obtained by equation 5.15 and the measurement of two new standard CPW lines with lengths of 1140 μm and 2880 μm. First, the loss per μm of a CPW line ($Loss_{1um}$) is determined using the two new lines in equation 5.16, where the loss of each line, described as $Loss_{1140um}$ and $Loss_{2880um}$, are also calculated using equation 5.15.

$$Loss_{1um} = (Loss_{2880um} - Loss_{1140um})/1740 \tag{5.16}$$

Next, the loss of Via-AAO-CPW section, defined as $Loss_{Via-AAO-CPW}$, is calculated using equation (5.17).

$$Loss_{Via-AAO-CPW} = \frac{Loss_{five-unit\ circuit} - Loss_{1140um} - Loss_{1um} * 180}{5} \quad (5.17)$$

Fig 5.28 shows the calculated loss comparison of Via-AAO-CPW for NW via based on Process I and conventional via. The NW via based on Process I shows lower loss and therefore better performance than conventional via up to 45 GHz. The loss difference of 0.035 dB at 30 GHz is observed. For data above 45 GHz, they have similar value.

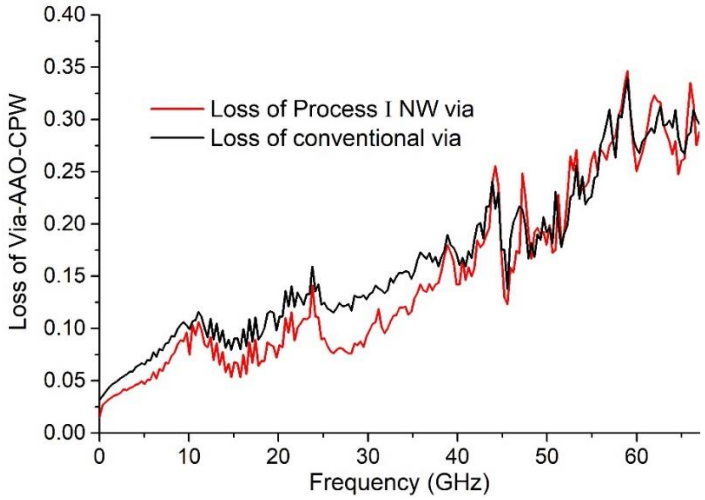

Fig 5.28. Comparison of Via-AAO-CPW loss of NW based on Process I via and conventional vias, where VW =30μm, VL=90μm and Δx = 0μm.

Fig 5.29 shows the Via-AAO-CPW loss comparison of NW via based on Process II and conventional via. Similarly, NW via based on Process II shows lower loss and therefore better performance compared to the conventional via up to 45 GHz. The loss difference of 0.023 dB at 30 GHz is observed. Above 45 GHz, the extracted loss is noise, and it is difficult to determine which type of via performs better.

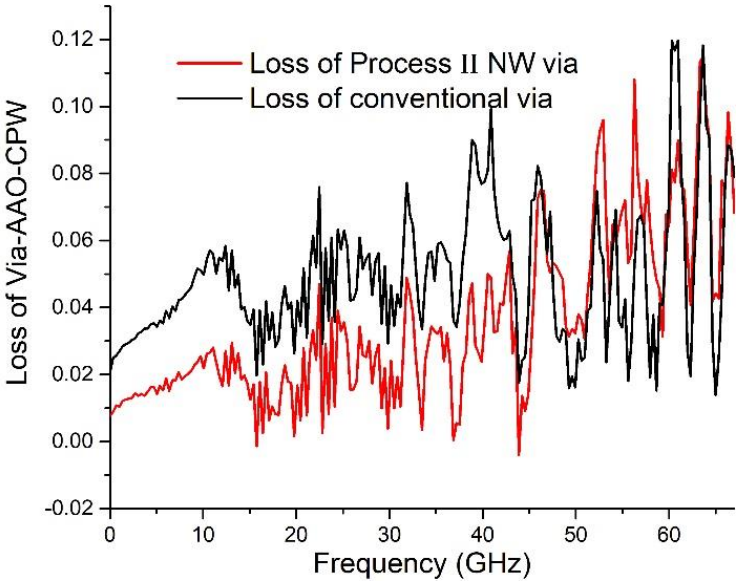

Fig 5.29. Comparison of Via-AAO-CPW loss of NW via based on Process II and conventional vias, where VW = 30μm, VL=70μm and Δx = 130μm.

In summary, NW vias, which allow signal transmission along with wire axis, provide benefit of low loss. The CPW with NW vias shows lower loss and better performance compared to the conventional vias up to 45 GHz.

5.4 Summary

In chapter 5, Cu NWs are studied as vertical vias for future communication application. Both DC and AC properties of NW vias are obtained. For DC resistance measurement, the resistivity of 4.82 μΩ-cm is obtained. For AC properties measurement, CPW with NW vias are designed and characterized.

Two processes, Process I and Process II are developed for NWs vias with 9 % porosity, 20 nm diameter and 1.2 μm thickness. The former one has NWs grown in the iAAO regions as a uniform layer, whereas the latter has NWs grown in the via region only. As a reference, a fabrication process of conventional via has been developed.

Based on Process I NW vias, different via dimensions and positions are designed, fabricated, and measured up to 40 GHz and 110 GHz. The results show that NW vias with wider VW, shorter VL and larger Δx have better performance. The loss of single G-S-G Type 1 NW via based on Process I is approximately 0.0275 dB at 40 GHz, which is promising compared to the other advanced via technologies.

The measurement comparison between NW vias based on Process I and II show similar results. NW vias based on Process I and Process II shows better performance than conventional via up to 45 GHz. Compared to the conventional via, a 0.035 dB and 0.023 dB lower loss at 30 GHz is observed for NW vias based on Process I and Process II, respectively. These results indicate the great potential of using Cu NWs as vertical interconnect.

In summary, the study in this chapter provides deep understanding for the NWs application in millimeter wave band communication technology. Cu NWs shows great potential to be vertical vias.

Chapter 6 Conclusion and future work

6.1 Conclusion

In this thesis, magnetic and Cu nanowires (NWs) are studied and characterized for two applications: biomedical labeling and communication.

A model has been developed to determine the FMR responses of single and array of magnetic nanowires (MNWs). The FMR frequencies can be predicted using Kittel equation. The susceptibility and linewidth of MNWs can be obtained by using micromagnetic software, like OOMMF and NMAG. As an example, the single and array of cobalt (Co) MNWs with 40 nm diameter and 800 nm length is simulated at 0.2 T DC field with the bulk mode FMR frequencies of 30 GHz and 21.4 GHz, respectively. The array shows lower FMR frequency due to the dipolar interaction effect between each NWs.

In experiments, MNWs are fabricated in 50 μm thick commercial anodized aluminum oxide (AAO) template. Two methods are developed for MNW characterization: DC field domain and frequency domain.

To characterize the MNWs in DC field domain, a VNA-FMR system is developed to acquire the FMR responses from S parameters. Magnitude method and phase analysis methods (PAM), which obtain the FMR frequencies using the magnitude and phase derivative of the S parameters, respectively, were proposed. Both methods determine the FMR frequencies accurately with good agreement between the experimental data and predicted data from the Kittel equation. For magnitude method, the factors that influence FMR responses has been studied, such as Cu back effect, position effect and volume effect. From these studies, the FMR signal strength can be enhanced by adding a Cu back layer,

putting the MNW sample on the slot of CPW, making the AC field direction perpendicular to the magnetization, and using a one-port test circuit instead of a two-port test circuit. The detection ability of the system used in this work was determined with the smallest detectable Co volume and magnetization of $2.2x10^{-4}$ mm^3 and 317 μemu, respectively. The PAM method is compared to the magnitude method and shows advantages in determining the FMR frequencies in DC field domain with overlapping linewidth and in providing information on moment direction. The position effect and volume effect were investigated for PAM method. It showed that the variation of sample size and position don't influence the FMR frequencies obtained from PAM method. Based on magnitude method and PAM method, a tri-labeling system has been proposed using Co, nickel (Ni) and iron (Fe) MNWs that shows the potential of MNW for biosensor application with multiple biomarkers.

In the previous study, MNWs are aligned in the same direction and spaced equally in a hexagonal orientation. However, these conditions cannot be satisfied, when MNWs are measured in a polycarbonate or in a biological sample. Both detection and identification can be achieved for MNWs in polycarbonate when equal spacing is invalid, whereas only detection can be achieved for MNWs in the biological sample when both alignment and equal spacing are invalid.

Next, MNWs are characterized in frequency domain as a magnetic substrate. The small volume of Co MNWs without Cu layer is characterized first using "four step methods". The FMR frequencies and permeability at 0.4 T can be obtained. But the responses from other fields are influenced by RF background noise and their permeability cannot be extracted. Therefore, large volume Co MNW sample is used, which provides FMR frequencies in the frequency bands that are away from board resonances. However,

the extracted permeability possess distortion from 25 GHz to 29.5 GHz influenced by the board resonances. To resolve this issue, a Cu back layer is added and provide successful permeability extraction on both large volume Co and Fe MNW samples.

To study the copper (Cu) NWs as vertical vias, a coplanar waveguide (CPW) line with NW via structure is designed and modeled. The 5.5 μm by 5.5 μm micron-sized Cu pillar with 17.5 μm interwire distance structure is used to replace the NW vias and to reduce the computation time. The simulation results of NW-based via indicate that this design can transmit signal along the NW wire axis successfully.

Then a CPW with NW via design is fabricated using Process I and Process II. They show similar performance across the frequency band of 0.01 - 67 GHz. Process I is studied primarily with measurements in three frequency bands: up to 40 GHz, up to 67 GHz and up to 110 GHz. The via dimension and position effect are studied. To design a low loss via, the wider via width, shorter via length and location closer to the CPW slot is preferred. The loss of single G-S-G NW via is extracted with the value of ~0.0278 dB at 40 GHz. Compared to other advanced via technologies, the via proposed in this work is promising. To determine the benefit of NW via, it is compared to the conventional via and show lower loss up to 45 GHz. Compared to the conventional via, a 0.035 dB and 0.023 dB lower loss at 30 GHz is observed for NW vias based on Process I and Process II, respectively.

6.2 Future work

To use MNWs as bio-labels, the detection and identification are required. However, the identification is lacking with current approach. The next step is to study a biological sample with MNWs in a liquid environment. Fe MNWs are preferred due to their high

saturation magnetization, which will provide strong FMR signal. In liquid environment, an external DC field could be used to align the NWs inside the cells to provide aligned orientation. In this way, the identification of MNWs inside cells is expected to be achieved even if no template is used.

For non-reciprocal device design, the next step will be to fabricate several Fe or Co MNW samples and characterize their performance at zero DC fields to obtain the FMR frequencies, permeability, and linewidth. The smallest linewidth is preferred. Then, based on the FMR frequency, the operation frequency band can be determined. By importing the extracted permeability into HFSS, the circuit with MNW substrate can be modeled and optimized to design a prototype for measurement.

For Cu NW used as vertical vias in integrated circuits (IC), the next step for this work is to further investigate the RF performance for NW vias with different wire diameter and porosity. The higher porosity and diameter are expected to provide higher signal transmission and better RF performance due to higher current flow area. But when the diameter is close to the skin depth at specific frequency, such as 330nm at 40GHz, the performance is expected to degrade. Therefore, a proper NW dimensions need to be investigated for specific frequency bands. Moreover, the NW vias will be studied for use in different integrated components or designs, such as transition from microstrip to CPW, inductors or capacitors.

BIBLIOGRAPHY

[1] Vigneshvar, S, Senthilkumaran, B. Current, “technological trends in biosensors, nanoparticle devices and biolabels: Hi-tech network sensing applications,” *Med Devices Sens.* 2018

[2] Fang, S.; Wang, C.; Xiang, J.; Cheng, L.; Song, X.; Xu, L.; Peng, R.; Liu, Z., “Aptamer-Conjugated Upconversion Nanoprobes Assisted by Magnetic Separation for Effective Isolation and Sensitive Detection of Circulating Tumor Cells”. *Nano Res.* 2014, 7, 1327−1336.

[3] Shi, D.; Sadat, M. E.; Dunn, A. W.; Mast, D. B., “Photo Fluorescent and Magnetic Properties of Iron Oxide Nanoparticles for Biomedical Applications.,” *Nanoscale*, 2015, 7, 8209−8232.

[4] S. Kumar and A. Kalkal, “Electrochemical detection: Cyclic voltammetry/differential pulse voltammetry/impedance spectroscopy” in *Nanotechnology in Cancer Management*, ed. K. R. Khondakar and A. K. Kaushik, Elsevier, 2021, pp. 43–71

[5] S. Kumar, Ashish, S. Kumar, S. Augustine, S. Yadav, B. K. Yadav, R. P. Chauhan, A. K. Dewan and B. D. Malhotra, “Effect of Brownian motion on reduced agglomeration of nanostructured metal oxide towards development of efficient cancer biosensor”, *Biosens. Bioelectron.*, 2018, 102, 247–255

[6] Dobson, J. (2006), “Magnetic nanoparticles for drug delivery,” *Drug Dev. Res.*, 67: 55-60.

[7] J. Alonso, H. Khurshid, V. Sankar, Z. Nemati, M. H. Phan, E. Garayo, J. A. García, and H. Srikanth, “FeCo nanowires with enhanced heating powers and controllable dimensions for magnetic hyperthermia,” *Journal of Applied Physics*, vol. 117, no. 17, Jul. 2015.

[8] D. Shore, S. L. Pailloux, J. Zhang, T. Gage, D. J. Flannigan, M. Garwood, V. C. Pierre, and B. J. H. Stadler, “Electrodeposited Fe and Fe–Au nanowires as MRI contrast agents,” *Chemical Communications*, vol. 52, no. 85, pp. 12634–12637, 2016.

[9] W. Zhou, J. Um, Y. Zhang, A. P. Nelson, Z. Nemati, J. Modiano B. Stadler and R. Franklin., "Development of a Biolabeling System Using Ferromagnetic Nanowires," in *IEEE Journal of Electromagnetics, RF and Microwaves in Medicine and Biology*, vol. 3, no. 2, pp. 134-142, June 2019.

[10] P. Biehl, M. V. D. Lühe, S. Dutz, and F. Schacher, “Synthesis, Characterization, and Applications of Magnetic Nanoparticles Featuring Polyzwitterionic Coatings,” *Polymers*, vol. 10, no. 1, p. 91, 2018.

[11] M. Faraji, Y. Yamini, and M. Rezaee, “Magnetic nanoparticles: Synthesis, stabilization, functionalization, characterization, and applications,” *Journal of the Iranian Chemical Society*, vol. 7, no. 1, pp. 1–37, 2010.

[12] A. Sharma, G. M. Orlowski, Y. Zhu, D. Shore, S. Y. Kim, M. D. Divito, A. Hubel, and B. J. H. Stadler, “Inducing cells to disperse nickel nanowires via integrin-mediated responses,” *Nanotechnology*, vol. 26, no. 13, p. 135102, Dec. 2015.

[13] Sharma, Anirudh, Yuechen Zhu, ShengShee Thor, Fang Zhou, Bethanie Stadler, and Allison Hubel. "Magnetic barcode nanowires for osteosarcoma cell control, detection and separation." *IEEE transactions on magnetics* (2012): 453-456.

[14] Yuanyuan Zhang, Xixi Feng, Kaiqiang Zhu, Xi Yang and Houmin Li, "An X-band tunable circulator based on Yttrium iron garnet thin film," *2016 IEEE International Conference on Microwave and Millimeter Wave Technology (ICMMT)*, 2016, pp. 425-427

[15] J. D. Adam, H. Buhay, M. R. Daniel, M. C. Driver, G. W. Eldridge, M. H. Hanes, and R. L. Messham, "Monolithic integration of an X band circulator with GaAs MMICs," in *IEEE MTT-S Int. Microw. Symp.Dig.*, Orlando, FL, USA, May 1995, pp. 97–98.

[16] F. K. H. Gellersen and A. F. Jacob, "A sol-gel approach for self-biased barium hexaferrite thin-film circulators," *2016 46th European Microwave Conference (EuMC)*, 2016, pp. 361-364

[17] S. Bierlich, T. Reimann, F. Gellersen, A. F. Jacob, J. Töpfer," Sintering, microwave properties, and circulator applications of textured Sc-substituted M-type ferrite thick films," *Journal of the European Ceramic Society*, 2019.

[18] M. Darques, J. De La T. Medina, L. Piraux, L. Cagnon and I. Huynen, "Microwave circulator based on ferromagnetic nanowires in alumina template", *Nanotechnology* 21 (2010) 145208

[19] J. De La T. Medina, J. Spiegel, M. Darques, L. Piraux and I. Huynen, "Differential phase shift in nonreciprocal microstrip lines on magnetic nanowired substrates", *Appl. Phys. Lett.* 96 (2010) 072508.

[20] Y. Cui *et al.*, "Monolithic Integration of Self-Biased C-Band Circulator on SiC Substrate for GaN MMIC Applications," in *IEEE Electron Device Letters*, vol. 40, no. 8, pp. 1249-1252, Aug. 2019

[21] S. J. Bleiker, A. C. Fischer, U. Shah, N. Somjit, T. Haraldsson, N. Roxhed, J. Oberhammer, G. Stemme, and F. Niklaus, "High Aspect-ratio through silicon vias for high-

frequency application fabricated by magnetic assembly of gold-coated nickel wires," *IEEE Trans. Compon., Packag. Manuf. Technol.*, vol. 5, no. 1, pp. 21-27, January 2015.

[22] A. Margomenos and L. P. B. Katehi, "Fabrication and accelerated hermeticity testing of an on-wafer package for RF MEMS*," IEEE Trans. Microw. Theory Tech.*, vol. 52, no. 6, pp. 1626–1636, 2004.

[23] J. M. Pinheiro, M. V. Pelegrini, L. Amorese, P. Ferrari, G. P. Rehder, and A. L. C. Serrano, "Nanowire-based through substrate via for millimeter-wave frequencies," in *IEEE MTT-S Int. Microw. Symp. Dig.*, San Francisco, CA, USA, May 2016, pp. 1–4.

[24] J. M. Pinheiro et al., "110-GHz Through-Substrate-Via Transition Based on Copper Nanowires in Alumina Membrane," in *IEEE Transactions on Microwave Theory and Techniques*, vol. 66, no. 2, pp. 784-790, Feb. 2018

[25] M. Bertrand *et al*., "Integrated Waveguides in Nanoporous Alumina Membrane for Millimeter-Wave Interposer," in *IEEE Microwave and Wireless Components Letters*, vol. 29, no. 2, pp. 83-85, Feb. 2019.

[26] A. L. C. Serrano *et al*., "3D inductors with nanowire through substrate vias," *2017 IEEE MTT-S International Microwave Symposium (IMS)*, 2017, pp. 1641-1644, doi: 10.1109/MWSYM.2017.8058952.

[27] Donahue M J and Porter D G 2002 OOMMF User's Guide, Version 1.2a3 (http://math.nist.gov/oommf)

[28] Available online: https://nmag-project.github.io/

[29] C. Wen-Bing, H. Man-Gui, Z. Hao, O. Yu, D. Long-Jiang, "Micromagnetic simulation on the dynamic susceptibility spectra of cobalt nanowires arrays: the effect of magnetostatic interaction" *Chin. Phys. B*, 19 (8) (2010), p. 087502.

[30] C. Kittel, “On the theory of ferromagnetic resonance absorption,” *in Phys. Rev.*, vol. 73, pp. 155-161, 1948.

[31] M. Darques, J. Spiegel, J. De la Torre Medina, I. Huynen, L. Piraux, “Ferromagnetic nanowire-loaded membranes for microwave electronics”, *Journal of Magnetism and Magnetic Materials*, Vol.321, 2009.

[32] ANSYS High Frequency Structure Simulator (HFSS), Version 15, Pittsburgh, PA, 2013.

[33] A. Sklyuyev, M. Ciureanu, C. Akyel, P. Ciureanu, D. Menard and A. Yelon, "Measurement of Complex Permeability of Ferromagnetic Nanowires using Cavity Perturbation Techniques," *2006 Canadian Conference on Electrical and Computer Engineering*, Ottawa, Ont., 2006, pp. 1486-1489

[34] A. Encinas-Oropesa, M. Demand, L. Piraux, I. Huynen, and U. Ebels, “Dipolar interactions in arrays of nickel nanowires studied by ferromagnetic resonance,” *Physical Review Letters*, Vol. 63, no. 10, 2001.

[35] M. Sharma, S. Pathak and M. Sharma, “FMR Measurements of Magnetic Nanostructures”, *Ferromagnetic Resonance*, 2013.

[36] E. Montoya, T. McKinnon, A. Zamani, E. Girt, B. Heinrich, “Broadband ferromagnetic resonance system and methods for ultrathin magnetic films”, *Journal of Magnetism and Magnetic Materials*, 2013.

[37] A. B. Kos, T. J. Silva, and P. Kabos, “Pulsed inductive microwave magnetometer”, *Review of Scientific Instruments*, 73, 3563, 2002.

[38] S.S Kalarickal, P. Krivosik, M. Wu, C.E. Patton, M.L. Schneider, P. Kabos, T.J. Silva, J.P. Nibarger, “Ferromagnetic resonance linewidth in metallic thin films: Comparison of measurement methods”, *Journal of Applied Physics*, 2006

[39] Y. Zhang, J. Um, W. Zhou, B. Stadler and R. Franklin, "Magnetic Nanowires for RF applications: Ferromagnetic Resonance and Permeability Characterization," *2019 IEEE MTT-S International Microwave Symposium (IMS)*, 2019, pp. 1100-1103

[40] [Online]. Available: https://www.rogerscorp.com/

[41] [Online]. Available: https://www.belfuse.com/cinch

[42] Y. Zhang, J. Um, B. Stadler and R. Franklin, "Signal Enhancement for Ferromagnetic Resonance Measurement of Magnetic Nanowire array," *2019 IEEE International Symposium on Antennas and Propagation and USNC-URSI Radio Science Meeting*, 2019, pp. 1305-1306.

[43] Y. Zhang, J. Um, B. Stadler and R. Franklin, "A Ferromagnetic Resonance Measurement System for Small Volume Magnetic Nanowires," 2019 *IEEE International Symposium on Antennas and Propagation and USNC-URSI Radio Science Meeting*, 2019, pp. 1307-1308.

[44] Y. Zhang, B. Garcia, J. Um, B. Stadler and R. Franklin, "A Phase Analysis Method for Ferromagnetic Resonance Characterization of Magnetic Nanowires," *2020 IEEE/MTT-S International Microwave Symposium (IMS)*, 2020, pp. 968-971.

[45] G. Hamoir, J. De La Torre Medina, L. Piraux and I. Huynen, “Self-Biased Nonreciprocal Microstrip Phase Shifter on Magnetic Nanowired Substrate Suitable for Gyrator Applications,” in *IEEE Transactions on Microwave Theory and Techniques*, vol. 60, no. 7, pp. 2152-2157, July 2012.

[46] G. Hamoir, L. Piraux and I. Huynen, “Control of Microwave Circulation Using Unbiased Ferromagnetic Nanowires Arrays,” in *IEEE Transactions on Magnetics*, vol. 49, no. 7, pp. 4261-4264, July 2013.

[47] B. K. Kuanr, V. Veerakumar, R. Marson, S. R. Mishra, R. E. Camley, Z. Celinski, “Nonreciprocal microwave devices based on magnetic nanowires,” *Applied Physics Letters*, vol 94, 2009.

[48] W. Zhou, J. Um, B. Stadler and R. Franklin, “Design of self-biased coplanar circulator with ferromagnetic nanowires,” *IEEE Radio and Wireless Symp. (RWS)*, pp. 240-242, 2018.

[49] M. Sharma and B. Kuanr, “Microwave devices based on template-assisted NiFe nanowires: fabrication and characterization,” *Journal of Physics D: Applied Physics*, vol 53, p. 065001, 2019.

[50] L. P. Carignan, C. Caloz and D. Menard “Dual-band integrated self-biased edge-mode isolator based on the double ferromagnetic resonance of a bistable nanowire substrate,” *IEEE MTT-S International Microwave Symposium, Anaheim*, CA, pp. 1336-1339, 2010.

[51] Pozar, *D. M. Microwave Engineering*, New York City, NY: John Wiley and Sons, Inc., 1998.

[52] V. Bekker, K. Seemann, H. Leiste, “A new strip line broad-band measurement evaluation for determining the complex permeability of thin ferromagnetic films”, *Journal of Magnetism and Magnetic Materials*, Vol. 270, 2004.

[53] Y. Liu, L. Chen, C. Y. Tan, H. J. Liu and C. K. Ong, “Broadband Complex Permeability Characterization of Magnetic Thin Films using Shorted Microstrip Transmission-Line Perturbation”, *Review of Scientific Instruments*, Vol. 76,2005.

[54] J. Wei, H. Feng, Z. Zhu, Q. Liu and J. Wang, “A short-circuited coplanar waveguide to measure the permeability of magnetic thin films: Comparison with short-circuited microstrip line”, *Review of Scientific Instruments,* Vol. 86, 2015.

[55] Y. Zhang, J. Um, B. Stadler and R. Franklin, "Permeability and Ferromagnetic Resonance Study for Magnetic Nanowires Substrate with Copper Layer," *in IEEE Microwave and Wireless Components Letters,* vol. 30, no. 11, pp. 1065-1068, Nov. 2020.

[56] R. Weerasekera, D. Pamunuwa, L.-R. Zheng, and H. Tenhunen, “Two-dimensional and three-dimensional integration of heterogeneous electronic systems under cost, performance, and technological constraints,” *IEEE Trans. Comput. -Aided Design Integr. Circuits Syst.*, vol. 28, no. 8, pp. 1237–1250, Aug. 2009.

[57] V. Sukumaran, G. Kumar, K. Ramachandran, Y. Suzuki, K. Demir, Y. Sato, T. Seki, V. Sundaram, and R. R. Tummala, “Design, fabrication, and characterization of ultrathin 3-D glass interposers with through-package-vias at same pitch as TSVs in silicon,” *IEEE Trans. Compon., Packag. Manuf. Technol.*, vol. 4, no. 5, pp. 786-795, May 2014.

[58] J. H. Lau, “Overview and outlook of through-silicon via (TSV) and 3D integrations,” *Microelectron. Int.* 28, 8–22 (2011).

[59] X. Gagnard, T. Mourier, “Through silicon via: From the CMOS imager sensor wafer level package to the 3D integration,” *Microelectronic Engineering,* Volume 87, Issue 3, pp. 470-47 (2010).

[60] W. Xu, L, Wang, Z. Guo, X. Chen, J. Liu, X. Huang, “Copper Nanowires as Nanoscale Interconnects: Their Stability, Electrical Transport, and Mechanical Properties” *ACS Nano,* 2015, 9, 1, 241–250

[61] Maqableh et al., “Low-Resistivity 10 nm Diameter Magnetic Sensors”, *Nano Letters*, 2012.

[62] J. Um et al., “Fabrication of Long-Range Ordered Aluminum Oxide and Fe/Au Multilayered Nanowires for 3-D Magnetic Memory,” *in IEEE Transactions on Magnetics*, vol. 56, no. 2, pp. 1-6, Feb. 2020.

[63] Y. Zhang, J. Um, B. Stadler, R. Henderson and R. Franklin, "Study of Nanowire-Based Integrated via Technology for CMOS Application in Millimeter-Wave Frequencies," in *IEEE Microwave and Wireless Components Letters*, vol. 31, no. 6, pp. 693-696, June 2021.

Appendix A Ferromagnetic resonance simulation procedure using OOMMF and NMAG

The simulation procedure is modified from [29]. The procedure steps are:

1. Set initial magnetization direction in the x direction, shown in Fig 2.4.

2. Add external DC magnetic field along with wire axis, z direction.

3. Start the simulation and reach the steady state of material, shown in Fig 2.5.

4. Add a pulse field as AC field in the y direction.

5. Calculate FMR response from $\chi = \frac{M(\omega)}{H(\omega)} = \chi'(\omega) - j\chi''(\omega)$, where $M(\omega)$ and $H(\omega)$ are magnetization and AC magnetic field in frequency domain. $\chi'(\omega)$ and $\chi''(\omega)$ are real and imaginary part of susceptibility in frequency domain. By plotting $\chi'(\omega)$ and $\chi''(\omega)$ with respect to the frequency in x or y direction, the FMR frequencies can be obtained from peak or dip of χ''.